Basic Characteristics of Rankine Cycle with Functional Elements, using Supercritical Carbon Dioxide

(超臨界二酸化炭素を用いたランキンサイクルと機能構成要素の基礎特性に関する研究)

September 2018

Chayadit Pumaneratkul

Index

Chapter 1

Introduction of carbon dioxide power cycle technology

Since the industrial revolution, the world's environment in recent years has been marked as a significant turning point. No one would have been concerned in the past that the fossil fuel-powered generation facilities, in such as the combustion process of coal, oil or gas will be caused of the greenhouse gases (GHGs) emission produced, which is the primary root of global warming and climate change crisis [1]. Furthermore, other significant cause can be considered from the fossil fuel consumption for driving inefficient vehicle usage in household and businesses operate. Particularly in consideration of energy and environment issues, there are many attempts in science and engineering with interdisciplinary efforts to research and develop for replacing the conventional fossil energy resources to green energy resources [2~3].

Since the 1950s, the working fluid Chlorofluorocarbons (CFCs) and Hydrochlorofluorocarbons (HCFCs) have been used for refrigeration in the industrial, in which people have much concern about depletion of the ozone layer. In 1987, the agreement to protect the world's ozone layer called the Montréal Protocol on Substances that Deplete the Ozone Layer has been signed, and in the agreement first 47 countries agreed on the protocol. The primary purpose of protocol deals with by phasing out the refrigerant and production that reason of ozone depletion. After the phasing-out of CFCs, the ozone hole in Antarctica area is found recovery slowly [4]. Furthermore, the international agreement of industrial countries to phase down the use of HCFCs under Montréal Protocol started in 2013 by targeting to final phase-out of HCFCs by 2030 and 2040 in developed and developing countries, respectively [5]. The timeline of the Montréal Protocol has drawn in Figure 1.1 [6~7]. 1997 Kyoto Protocol, the world's first global warming and climate change treaty, is a binding agreement to reduce GHGs emission level with 192 parties' agreement. In 2012, the second commitment period (2013 – 2020) had severe been purposed to reduce 20 % of 1990 GHGs emission level by the year 2020. In order to prevent global warming and greenhouse effect, Hydrofluorocarbon (HFCs) had been recommended to replace with CFCs and HCFCs, and widely used in various industries for many years [8]. HFCs are commonly used in air conditions and refrigerants system, which does not affect to Ozone Layer Depletion. The Ozone Layer Depletion (ODP) is the potential of the refrigerant to destroy the ozone layer by using CFC-11 as a datum reference, where CFC-11 has an ODP of 1.0. However, HFCs have a very high impact on Global Warming Potential (GWP), where GWP means the ratio of how much effect of the refrigerant that will cause the global warming by comparison with the similar mass of carbon dioxide (CO_2). Furthermore, 2 to 4 % increase of HFCs is forecasted in the overall climate forcing impact by 2050 [9].

In 2015, the 21st session of the Conference of the Parties (COP) to the United Nation Framework Convention on Climate Change (UNFCCC), so-called "Paris Agreement", as well suggested procedures to reduce the carbon emission at the earliest and aim to respond to the global climate change threat by handling the global average temperature rising in this century to well below 2 °C above the pre-industrial level, and to intend to limit of temperature rising further below to 1.5 °C [10]. To achieve the goal of Paris Agreement, the natural working fluid such as ammonia (NH_3) and carbon dioxide (R-744 or CO_2) have recommended to utilize and use as a refrigerant in industrial instead of HFCs. Especially, CO_2 is also listed in the required corporate control in the Kyoto Protocol. Furthermore, from "Act on Rational Use and Proper Management of Fluorocarbons" 2015, Ministry of the Environment, Government of Japan, states that CO_2 is one of the recommended alternative refrigerants to use for combat world's emission crisis [11].

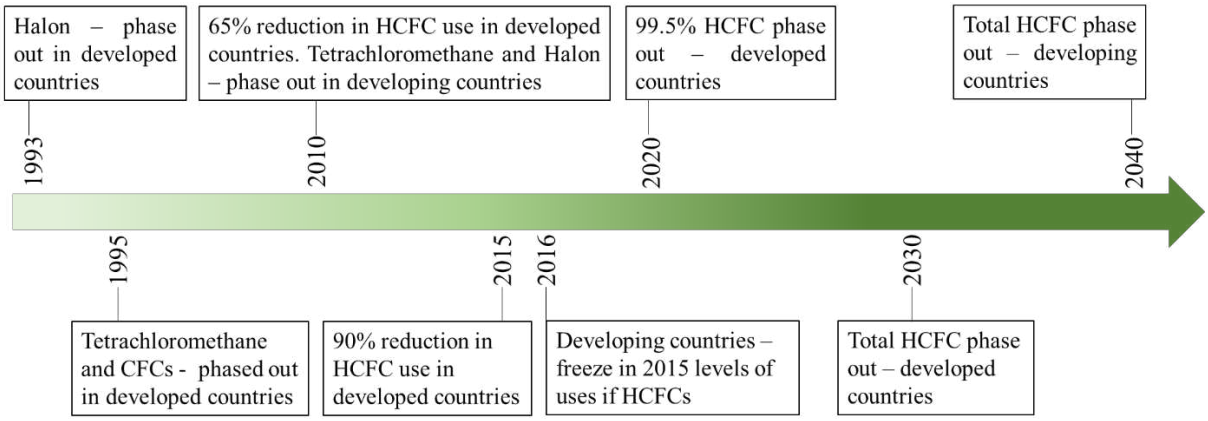

Figure 1.1. Timeline of Montréal Protocol [8~9].

In the viewpoint of preventing global warming and greenhouse effect, the interest to use CO_2 as a natural working fluid has been given much attention for decades by taking an account of the reasons that CO_2 itself is environmentally friendly when compared with other working fluid, where ODP and GWP of CO_2 are defined by 0 and 1, respectively. The characteristics and properties of various working fluid are listed in Table 1.1. CO_2 is also classified as non-flammable, non-toxic, chemically inactive, and inexpensive as well. Also, vapor pressure and volumetric refrigeration capacity of CO_2, which are 22,545 kJ/m^3 at 0 °C, is much higher when compared with other common working fluids available in the market. It means that by using CO_2 in the thermodynamic cycle, the system performance and energy transport with the working fluid would be much effective.

Table 1.1. Characteristic of some representative working fluids [12]

Properties	**R-12**	**R-22**	**R-134a**	**R-407C**	**R-410A**	**R-717**	**R-209**	**R-744**
ODP/GWP	1/8500	0.05/1700	0/1300	0/1600	0/1900	0/0	0/6	0/1
Flammability/toxicity	N/N	N/N	N/N	N/N	N/N	Y/Y	Y/N	N/N
Molecular mass (kg/kmol)	120.9	86.5	102	86.2	72.6	17	44.1	44
Critical pressure (MPa)	4.11	4.97	4.07	4.64	4.79	11.42	4.25	7.38
Critical temperature (°C)	11.2	96	101.1	86.1	70.2	133	96.7	31.1
Reduced pressure[a]	0.07	0.1	0.07	0.11	0.16	0.04	0.11	0.47
Reduced temperature[b]	0.71	0.74	0.73	0.76	0.79	0.67	0.74	0.9
Refrigerant capacity[c] (kJ/m^3)	2734	4356	2868	4029	6763	4382	3907	22,454

R-12: dichlorodifluoromethane; R-22: chlorodifluoromethane; R-134a: tetrafluoroethane; R-407C: ternary mixture of difluoromethane/pentafluoroethane/tetrafluoroethane (23/25/52, %); R-410A: binary mixture of difluoromethane/pentafluoroethane (50/50, %); R-717: ammonia; R-290: propane; R-744: carbon dioxide.

[a] Ratio of saturation pressure at 0 °C to critical pressure.

[b] Ratio of 273.15 K (0 °C) to critical temperature in Kelvin.

[c] Volumetric refrigeration capacity at 0 °C.

The utilization of CO_2 in green technology purposed applications have been researched and developed from various research groups and applied to various field such as chemical engineering, industrial engineering, mechanical engineering, environmental engineering, electrical engineering, nuclear engineering and so forth. The recently available representative specific studies are shown;

- CO_2 capture technologies [13~15]
- CO_2 heat pump cycle [16~17]
- CO_2 air-conditioning system [18]
- CO_2 ECU (environment control unit) [19]

- CO_2 plume geothermal system [20~21]
- CO_2 nuclear reactor [22]
- CO_2 power generation cycle [23~24]

Some of the CO_2 applications dominate in the supercritical phase. Because of the thermophysical properties indicate that CO_2 is easily changed its phase to supercritical phase in moderate operation condition due to its low critical point, in which the critical pressure and critical temperature of CO_2 are 7.38 MPa and 31.1 °C, respectively. Thus, CO_2 can become the supercritical state easily, when compared with other working fluid (shown in Table 1.1), even when it is operated at a comparatively low temperature range. From the reasons mentioned, many attempts have been made so far to replace the high global warming working fluids with natural working fluid CO_2 in power cycle, in which CO_2 could yield high efficiency system performance with a relatively low operation range of temperature around 30 °C.

Using CO_2 as working fluid in the thermo-fluid cycle can be considered to achieve the targeted level of the global warming treaty and the world's sustainable development. The gases emitted from industrial plants or transportation system can capture and recycle by separating CO_2 gas with chemical absorption or membrane technology [25]. After captured of CO_2, it can be purified and store in a gas cylinder in convenience. In principle, CO_2 is easy to supply for consumer and utilize as a working fluid in the thermos-fluid cycle for electric energy and/or thermal (heat) energy generation in an industrial plant or household usage.

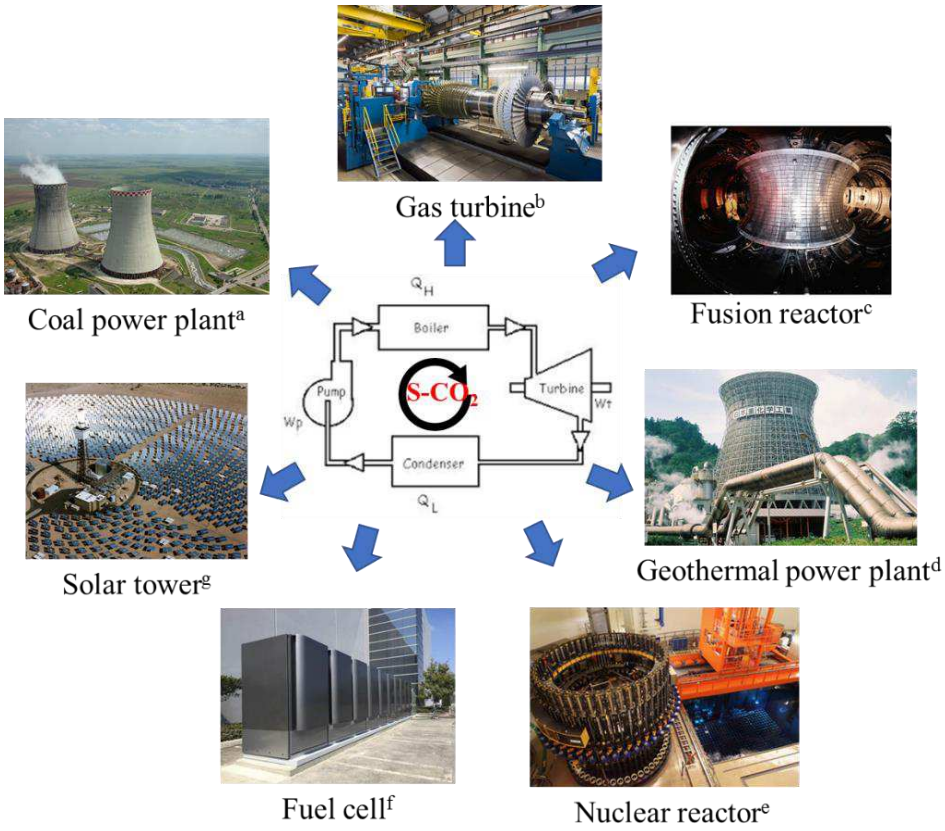

Figure 1.2. The potential applications of supercritical CO_2 power cycle[1].

[1]Pictures are taken from the following website only to symbolize potential applications of the supercritical CO_2 cycle, a: rtem via shutterstock.com, b: siemens.com, c: inverse.com, d: aiche.org, e: pinsdaddy.com, f: pinsdaddy.com, g: funnyjunk.com.

In the term of protecting the world environment and sustainable development, the application of renewable energy to electric power generation and thermal energy applied is essential. In order to achieve the higher efficiency by using CO_2 as a working fluid, achieving the CO_2 supercritical state is essential to enhance the operation in power cycle. Due to the lower temperature of attaining supercritical state, the supercritical CO_2 power cycle system can be considered to apply to various heat sources such as geothermal or solar thermal energy, and also nuclear reactor. Supercritical CO_2 also can be utilized as well in the high-temperature fossil fuel power generation cycle. The potential applications of supercritical CO_2 power cycle are based upon the Rankine cycle shown in Figure 1.2.

The first study on supercritical CO_2 cycle system was appeared in 1968 by Angelio [26]. Although the research focused on the CO_2 condensation cycle, however, the supercritical CO_2 thermodynamic power cycle in the high temperature range (650 °C to 800 °C) was also suggested with promising high efficiency in the study. Supercritical CO_2 thermodynamic power cycle has been developed so far in the wide range of application, and some of which are, such as

- Brayton cycle [27]
- Pre-compression cycle [28]
- Recompression cycle [29]
- Partial cooling cycle [30]

On the other hand, the study on the low temperature range of supercritical CO_2 power cycle is also capable of using a natural renewable heat source such as solar energy or geothermal energy [31~32].

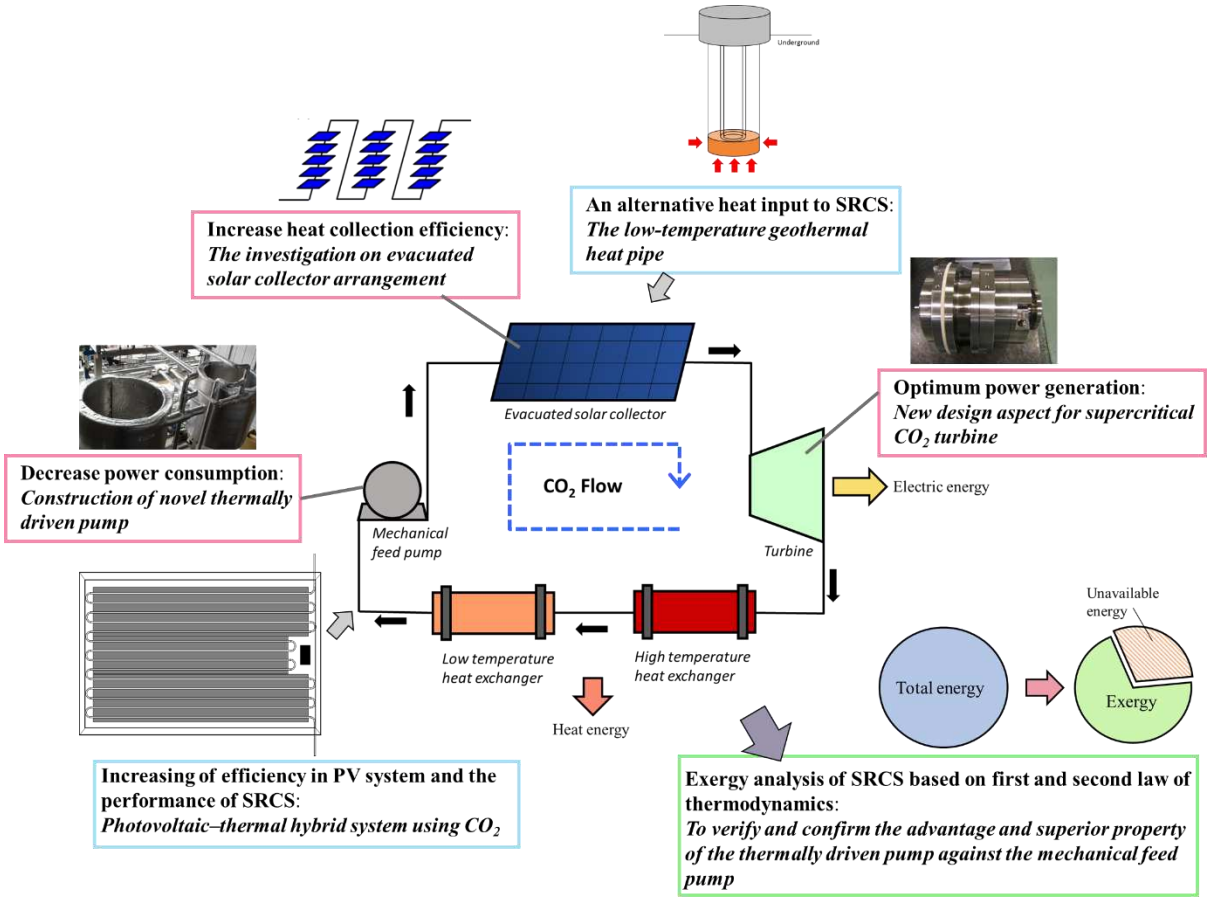

Figure 1.3. Development structure of SRCS.

The new combined power/heat thermal-fluid cycle with operating temperature range around 30 °C to 200 °C using CO_2 as a working fluid and utilize solar energy as the energy source, so-called supercritical CO_2 solar Rankine cycle system (SRCS), has been originally designed and developed by the research group since 2004 in Kyoto, Japan [33]. By the unique properties of CO_2, it is resulted to avoid the limitation appeared in an ordinary Rankine cycle, such as using water as a working fluid [34], SRCS gives the high performance and effectiveness. In this thesis, the current development on SRCS will be discussed along with the theory behind, which are mainly developed on the turbine and thermally driven pump.

This work presented in this thesis contributes on the research based on CO_2 working fluid in SRCS, it can be observed that the specific optimum designed on supercritical CO_2 machinery has not extensive developed yet, many opportunities for enhancement. The development structure on the SRCS in this thesis is drawn in Figure 1.3. Three key elements in the SRCS; Evacuated solar collector, supercritical CO_2 turbine and thermally driven pump are evaluated and developed to enhance the performance of SRCS. The optimum power generation is investigated with decreasing power consumption of the system. To further analyze on the system, the exergy analysis based on first and second laws of thermodynamics on the SRCS with mechanical feed pump and thermally driven pump are compared and employed to verify the losses of quality and work potential of the system. It can be seen from the exergy analysis that the weakness appears in a current system designed. By focusing on the progression of evacuated solar collector and thermally driven pump, exergy destruction is found smaller. The additional system to improve system efficiency of SRCS and improve on the exergy destruction in evacuated solar collector part, the so-called photovoltaic-thermal hybrid system is discussed in detail. For further development of SRCS, some low-temperature geothermal heat source as heat input is applied to generate electric and thermal energy to propose and analyze the system performance and characteristics. The proposed study is to sustainably develop and extend the uses of CO_2 in energy conversion cycle as a pathway on a low-carbon and green energy future.

The present thesis consists of the following chapters:

Chapter 1, the present chapter, describes the research motivation and background. This chapter also states the contents of the thesis briefly.

Chapter 2 describes the properties of CO_2 in the supercritical state by explaining the maximum of specific heat on the pseudocritical region. The fundamental principle of the Rankine cycle and supercritical Rankine cycle are also discussed here.

Chapter 3 mentions the components and formula on the SRCS. The analysis and investigation on the evacuated solar collector arrangement, a new development of supercritical CO_2 turbine and thermally driven pump component are given here, by both experimental and analytical approach on flow characteristic. The development in components shows an increase in the performance of the system.

Chapter 4 mentions the theory of the exergy balance in the SRCS together with a comparison of the exergetic efficiency of the system, with explaining conventional mechanical feed pump and newly development thermally driven pump. The optimum development on the system is also suggested here.

Chapter 5 mentions the additional system of SRCS, photovoltaic-thermal hybrid system to enhance the efficiency of electric and thermal energy generation. Also, the numerical simulation on the thermal characteristic of the hybrid system compared with ordinary PV system is shown at the same time.

Chapter 6 presents a new application of SRCS to use low temperature geothermal energy as heat input by using a heat pipe device. The system simulation on performance and experimental results of the system model are discussed.

Chapter 7 gives the general conclusion from Chapter 2 to Chapter 6. The development and achievement in SRCS are concluded here. The aspect of energy security and environment profits of Japan is also mentioned. Further study for the fundamental and the system is finally suggested.

References

[1] Hu, Y., Naito, S., Kobayashi, N. and Hasatani, M., 2000. CO_2, NO_x and SO_2 emissions from the combustion of coal with high oxygen concentration gases. *Fuel*, *79*(15), pp.1925-1932.

[2] Panwar, N.L., Kaushik, S.C. and Kothari, S., 2011. Role of renewable energy sources in environmental protection: a review. *Renewable and Sustainable Energy Reviews*, *15*(3), pp.1513-1524.

[3] Lund, H., 2007. Renewable energy strategies for sustainable development. *Energy*, *32*(6), pp.912-919.

[4] Perlwitz, J., Pawson, S., Fogt, R.L., Nielsen, J.E. and Neff, W.D., 2008. Impact of stratospheric ozone hole recovery on Antarctic climate. *Geophysical Research Letters*, *35*(8), p. L08714.

[5] Norman, C., DeCanio, S. and Fan, L., 2008. The Montreal Protocol at 20: Ongoing opportunities for integration with climate protection. *Global Environmental Change*, *18*(2), pp.330-340.

[6] Fahey, D.W., 2013. The Montreal Protocol Protection of Ozone and Climate. *Theoretical Inquiries in Law*, *14*(1), pp.21-42.

[7] Brack, D., 2017. *International trade and the Montreal Protocol*. Routledge.

[8] Lorentzen, G., 1995. The use of natural refrigerants: a complete solution to the CFC/HCFC predicament. *International journal of refrigeration*, *18*(3), pp.190-197.

[9] Velders, G.J., Fahey, D.W., Daniel, J.S., McFarland, M. and Andersen, S.O., 2009. The large contribution of projected HFC emissions to future climate forcing. *Proceedings of the National Academy of Sciences*, *106*(27), pp.10949-10954.

[10] Rogelj, J., Den Elzen, M., Höhne, N., Fransen, T., Fekete, H., Winkler, H., Schaeffer, R., Sha, F., Riahi, K. and Meinshausen, M., 2016. Paris Agreement climate proposals need a boost to keep warming well below 2 C. *Nature*, *534*(7609), p.631.

[11] Ministry of the Environment Japan, 2015. Law on regulation of management and rational use of fluorocarbons, http://www.env.go.jp/earth/ozone/cfc/law/kaisei_h27/index.html. (Accessed February 2018).

[12] Ke, J., Han, B., George, M.W., Yan, H. and Poliakoff, M., 2001. How does the critical point change during a chemical reaction in supercritical fluids? A study of the hydroformylation of propene in supercritical CO_2. *Journal of the American Chemical Society*, *123*(16), pp.3661-3670.

[13] Bates, E.D., Mayton, R.D., Ntai, I. and Davis, J.H., 2002. CO_2 capture by a task-specific ionic liquid. *Journal of the American Chemical Society*, *124*(6), pp.926-927.

[14] Wang, Q., Luo, J., Zhong, Z. and Borgna, A., 2011. CO_2 capture by solid adsorbents and their applications: current status and new trends. *Energy & Environmental Science*, *4*(1), pp.42-55.

[15] Zhao, L., Zhao, R., Deng, S., Tan, Y. and Liu, Y., 2014. Integrating solar Organic Rankine Cycle into a coal-fired power plant with amine-based chemical absorption for CO_2 capture. *International Journal of Greenhouse Gas Control*, *31*, pp.77-86.

[16] Nekså, P., Rekstad, H., Zakeri, G.R. and Schiefloe, P.A., 1998. CO_2-heat pump water heater: characteristics, system design and experimental results. *International Journal of Refrigeration*, *21*(3), pp.172-179.

[17] Yamaguchi, H., Zhang, X.R. and Fujima, K., 2008. Basic study on new cryogenic refrigeration using CO_2 solid–gas two phase flow. *International Journal of Refrigeration*, *31*(3), pp.404-410.

[18] Lorentzen, G. and Pettersen, J., 1993. A new, efficient and environmentally benign system for car air-conditioning. *International Journal of Refrigeration*, *16*(1), pp.4-12.

[19] Li, D. and Groll, E.A., 2004. Theoretical performance evaluation of a carbon dioxide based environmental control unit (ECU) with microchannel heat exchangers. In *Proc. of the 6th IIR–Gustav Lorentzen Conf. on Natural Working Fluids*.

[20] Wang, J., Wang, J., Dai, Y. and Zhao, P., 2014. Thermodynamic analysis and optimization of a transcritical CO_2 geothermal power generation system based on the cold energy utilization of LNG. *Applied Thermal Engineering*, *70*(1), pp.531-540.
[21] Pruess, K., 2008. On production behavior of enhanced geothermal systems with CO_2 as working fluid. *Energy Conversion and Management*, *49*(6), pp.1446-1454.
[22] Handwerk, C.S., Driscoll, M.J. and Hejzlar, P., 2008. Optimized core design of a supercritical carbon dioxide-cooled fast reactor. *Nuclear Technology*, *164*(3), pp.320-336.
[23] Ahn, Y., Bae, S.J., Kim, M., Cho, S.K., Baik, S., Lee, J.I. and Cha, J.E., 2015. Review of supercritical CO_2 power cycle technology and current status of research and development. *Nuclear Engineering and Technology*, *47*(6), pp.647-661.
[24] Persichilli, M., Kacludis, A., Zdankiewicz, E. and Held, T., 2012. Supercritical CO_2 power cycle developments and commercialization: why sCO_2 can displace steam ste. *Power-Gen India & Central Asia*.
[25] Bredesen, R., Kumakiri, I. and Peters, T., 2009. CO_2 capture with membrane systems. *Membrane Operations: Innovative Separations and Transformations*, pp.195-220.
[26] Angelino, G., 1968. Carbon dioxide condensation cycles for power production. *Journal of Engineering for Power*, *90*(3), pp.287-295.
[27] Wright, S.A., Radel, R.F., Vernon, M.E., Rochau, G.E. and Pickard, P.S., 2010. Operation and analysis of a supercritical CO_2 Brayton cycle. *Sandia Report, No. SAND2010-0171*.
[28] Dostal, V., 2004. A supercritical carbon dioxide cycle for next generation nuclear reactors, *Doctoral dissertation of Department of Nuclear Engineering, Massachusetts Institute of Technology*, Massachusetts, USA.
[29] Sarkar, J., 2009. Second law analysis of supercritical CO_2 recompression Brayton cycle. *Energy*, *34*(9), pp.1172-1178.
[30] Neises, T. and Turchi, C., 2014. A comparison of supercritical carbon dioxide power cycle configurations with an emphasis on CSP applications. *Energy Procedia*, *49*, pp.1187-1196.
[31] Yamaguchi, H. and Zhang, X.R., 2017. Development of Supercritical CO_2 Solar Rankine Cycle System. In *Energy Solutions to Combat Global Warming* (pp. 3-27). Springer, Cham.
[32] Pumaneratkul, C., Yamasaki, H., Yamaguchi, H., Kitamura, S. and Sako, Y., 2017. Supercritical CO_2 Rankine Cycle System with Low-Temperature Geothermal Heat Pipe. *Energy Procedia*, *105*, pp.1029-1036.
[33] Zhang, X.R., Yamaguchi, H., Fujima, K., Enomoto, M. and Sawada, N., 2005. A feasibility study of CO_2-based Rankine cycle powered by solar energy. *JSME International Journal Series B Fluids and Thermal Engineering*, *48*(3), pp.540-547.
[34] Bao, J. and Zhao, L., 2013. A review of working fluid and expander selections for organic Rankine cycle. *Renewable and Sustainable Energy Reviews*, *24*, pp.325-342.

Chapter 2

The significance of supercritical CO_2 as a working fluid in Rankine cycle energy conversion system

The thermo-physical details of CO_2 and its supercritical state will be provided and discussed in view of the properties of thermal energy transfer. Moreover, the fundamental principle of the energy conversion cycle is described in this chapter.

A thermodynamic cycle is composited with various thermodynamic processes to transfer heat and work of the cycle. Eventually, the different properties of working fluid in the cycle such as pressure, temperature and other state variables are returned in the system to the initial state [1]. The concept of a thermodynamic cycle has been accorded to the law of thermodynamics, which made use of the power cycle for converting heat to useful work as an ideal reference cycle of heat engine [2]. The thermal efficiency of a thermodynamic cycle, η_{th}, in term of specific quantities can be specified as

$$\eta_{th} = \frac{W_{net}}{Q_H} \tag{2.1}$$

where W_{net} and Q_H are net power output from cycle per unit mass and energy input to cycle per unit mass, respectively.

The thermodynamic cycle can be classified into two primary classes, which are power cycle and heat pump cycle. Typically, the power cycle is used to convert heat energy input into mechanical work output, while the heat pump cycle uses mechanical work input to transfer low-temperature heat energy to high-temperature heat energy. The thermodynamic power cycles are widely used as a primary operation in a heat engine, which propels the world nowadays, mostly in electric power generation and in a motor vehicle [3~4].

In this chapter, the power cycles are discussed in general. Some of primary representative thermodynamic cycles (namely Carnot cycle, Brayton (Joule) cycle and Rankine cycle) are presented in order to differentiate and to give an advantage for supercritical Rankine cycle. Moreover, the detail on CO_2 in the supercritical region is later given.

2.1 Power cycle system

2.1.1 Carnot cycle

Carnot cycle has ultimate efficiency possible to an engine, in which heat is taken in at a constant upper pressure (P_h) and temperature (T_h) and rejected at a constant lower pressure (P_l) and temperature (T_l) [5]. The *T-s* and *P-h* diagram of Carnot cycle with four representative cycle points of ①, ②, ③ and ④, is shown in Figure 2.1 (a) and (b), respectively.

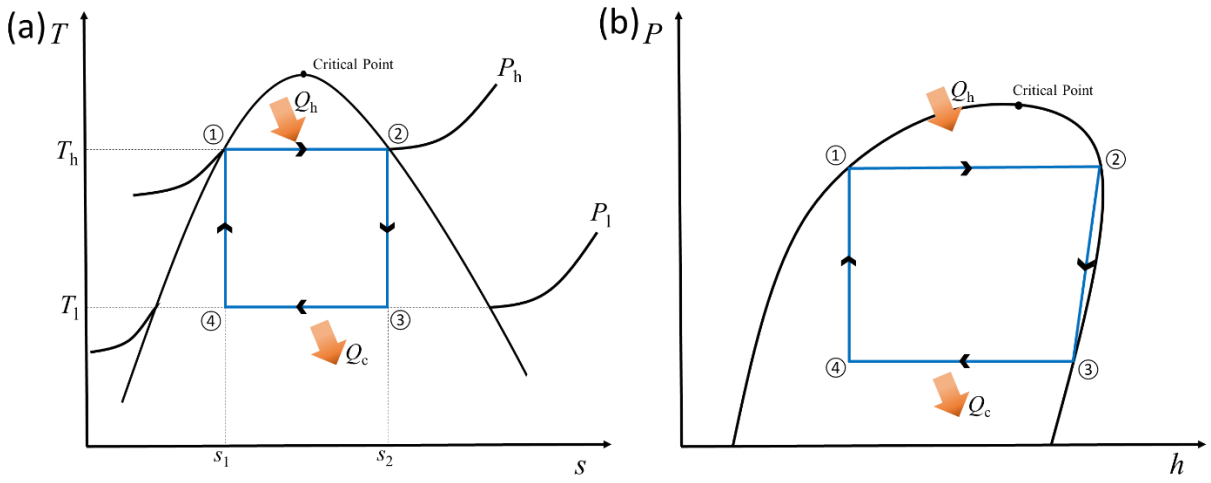

Figure 2.1. (a) *T-s* diagram and (b) *P-h* diagram of Carnot cycle.

i. Isothermal expansion process of the working fluid at a constant upper temperature (T_h) accompanied by heat absorption from the heat source (Q_h), (① → ②).
ii. Isentropic expansion process of the working fluid with a temperature drop from upper temperature to lower temperature (T_h to T_l), (② → ③).
iii. Isothermal compression process at a constant lower temperature (T_l) of working fluid with heat rejection (Q_c), (③ → ④).
iv. Isentropic compression with a temperature rise of working fluid from a lower temperature to upper temperature (T_l to T_h), and returning to the initial condition, (④ → ①).

From the *T-s* diagram, heat absorption during isothermal expansion process (① → ②) can be expressed as $T_h(s_2 - s_1)$ while the heat rejection in isothermal compression process (④ → ①) is $T_l(s_2 - s_1)$.

The work done of the Carnot cycle is from:

$$\begin{aligned}\text{Work done} &= \text{Heat absorption} - \text{Heat rejection}\\ &= Q_h - Q_c\\ &= (h_2 - h_1) - (h_3 - h_4)\\ &= T_h(s_1 - s_2) - T_l(s_1 - s_2)\\ &= (s_1 - s_2)(T_h - T_l)\end{aligned}$$

Carnot cycle will have the efficiency:

$$\eta_{\text{Carnot}} = \frac{\text{Work done}}{\text{Heat absorption}} = \frac{(s_1 - s_2)(T_h - T_l)}{T_h(s_1 - s_2)} = \frac{T_h - T_l}{T_h}$$

or

$$\eta_{\text{Carnot}} = 1 - \frac{T_l}{T_h} \qquad (2.2)$$

From the equation (2.2), it can be seen that the efficiency of the Carnot cycle increases as T_h is increased with T_l is decreased. In other words, heat would be absorbed in as the highest temperature as possible and rejected at as the lowest temperature as possible.

It can be said that the Carnot cycle has the highest possible efficiency, which represents to perfection cycle compared with others. Further, the thermal efficiency of the Carnot cycle mainly depends on the upper and lower temperatures in the cycle, in which heat transfer takes place. The efficiency also depends on the working fluid in the cycle, including the perfect (ideal) fluid.

2.1.2 Brayton cycle

Brayton cycle, is also sometimes known as the Joule cycle, can be considered as an ideal cycle for the gas turbine cycle, in which the working fluid undergoes in a closed loop. The cycle's combustion and exhaust processes are modeled by constant pressure heat absorption and rejection, respectively [6]. The Brayton cycle is an opened cycle (or closed cycle), which uses a single phase gaseous working fluid.

Similar to the Carnot cycle, Brayton cycle also consists of four processes, which they can sort as two isentropic processes and two isobaric processes as shown in Figure 2.2 (a) and (b) for *T-s* and *P-h* diagram, respectively.

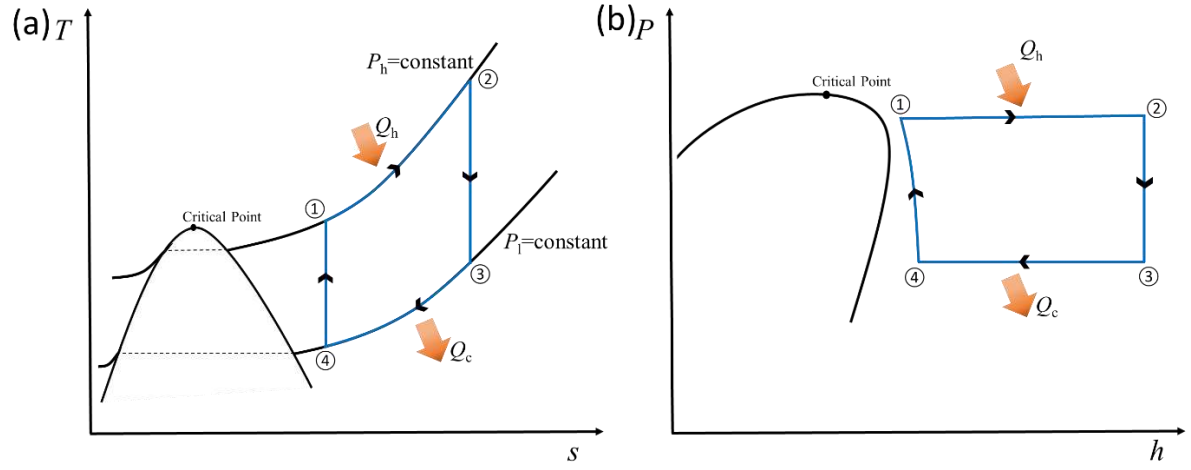

Figure 2.2. (a) *T-s* diagram and (b) *P-h* diagram of the Brayton cycle.

i. The isobaric process of the working fluid at a constant upper pressure (P_h) accompanied by heat absorption from the heat source (Q_h), (① → ②).
ii. Isentropic expansion process of the working fluid with the pressure drop (P_h to P_l) and work output from the cycle, (② → ③).
iii. The isobaric process of the working fluid at a constant lower pressure (P_l) with heat rejection (Q_c) to the surroundings, and returning to the initial state, (③ → ④).
iv. Isentropic compression process with a temperature rise of the working fluid compressed to higher pressure state (P_l to P_h), (④ → ①).

In the ideal Brayton cycle, heat is absorbed into the cycle at a constant pressure process:

$$Q_h = h_2 - h_1 = c_p(T_2 - T_1)$$

moreover, heat is rejected at a constant pressure process:

$$Q_l = h_3 - h_4 = c_p(T_3 - T_4)$$

The efficiency of such a simple Brayton cycle, for an ideal gas, can be expressed in term of the temperatures as:

$$\eta_{\text{Brayton}} = \frac{\text{Net work}}{\text{Heat absorbtion}} = \frac{c_p\left[(T_2 - T_3) - (T_1 - T_4)\right]}{c_p\left(T_2 - T_1\right)} = 1 - \frac{(T_3 - T_4)}{(T_2 - T_1)}$$

alternatively, regarding the compressor pressure ratio ($PR = P_h/P_l$), in which the efficiency becomes:

$$\eta_{\text{Brayton}} = 1 - \frac{1}{PR^{\frac{k-1}{k}}} \tag{2.3}$$

where k is the specific heat ratio.

In general, increasing the pressure ratio PR is the appropriate way to increase the Brayton cycle efficiency in light of the fact that the cycle approaches the Carnot cycle. Regarding Carnot's principle, higher efficiencies can be achieved by increasing the temperature of the gas [7].

The initially Brayton cycle was considered as a closed loop like external combustion hot air engine. However, it was found that the cycle gains higher efficiency and more reliable when converted into an open loop internal combustion engine and be a model of gas turbine later chapter in this thesis.

2.1.3 Rankine cycle

Rankine cycle is one of the closed-loop power generation cycles, which is synonymous with the stream cycle and can be considered as the oldest human-made functional heat cycle [8]. Furthermore, the Rankine cycle is usually used in a thermal power plant [9]. The ideal Rankine cycle is a practical model of energy conversion from heat to mechanical work, a basic diagram of the simple cycle is illustrated in Figure 2.3. The simple Rankine cycle consists of four main elements and procedures (Figure 2.3), the procedures are listed below;

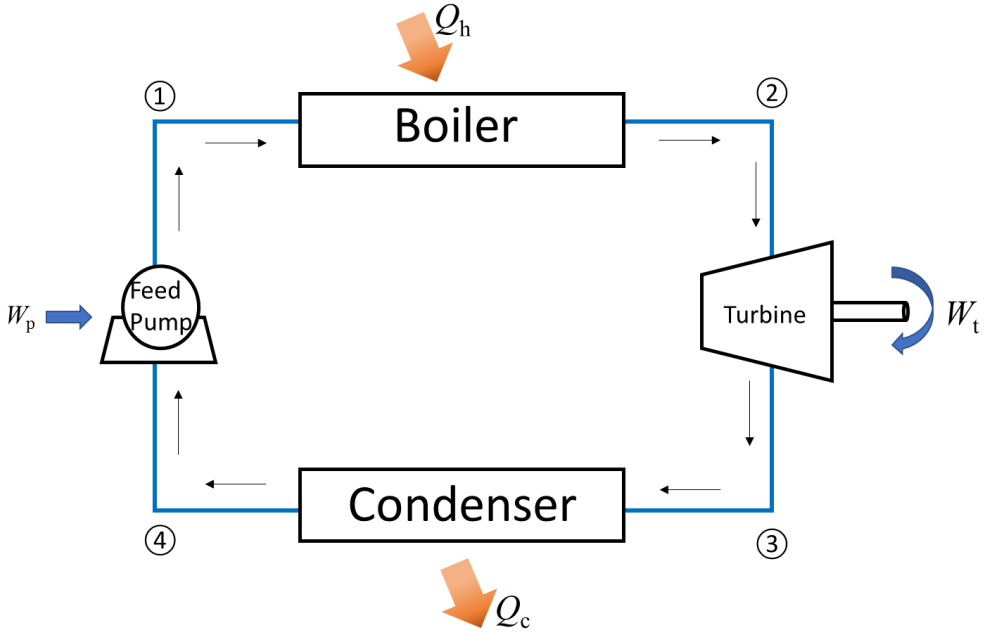

Figure 2.3. Simple Rankine cycle.

i. ① → ②; Boiler, heat absorption (Q_h).
ii. ② → ③; Turbine, work output (W_t).
iii. ③ → ④; Condenser, heat rejection (Q_c).
iv. ④ → ①; Feed pump, work input (W_p).

Commonly, the conventional Rankine cycle is modified to the superheat of entering turbine state, which is indicated at point ② in the *T-s* diagram shown in Figure 2.4 (a) while the *P-h* diagram of the Rankine cycle shown in Figure 2.4 (b).

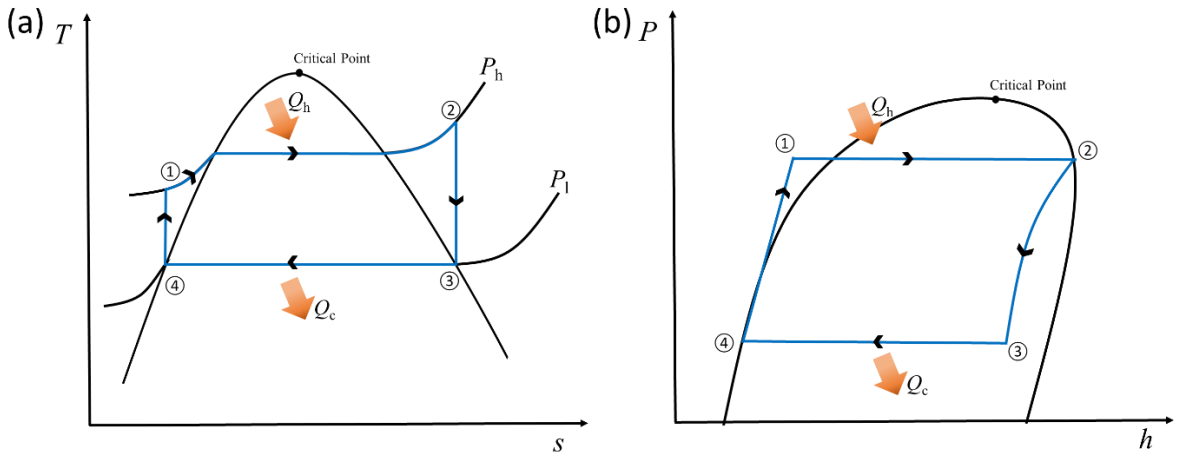

Figure 2.4. (a) *T-s* diagram and (b) *P-h* diagram of Rankine cycle.

i. Heating of working fluid at constant pressure by heat absorption (Q_h), (① → ②).
ii. Adiabatic expansion process of working fluid to a low-pressure state (P_l), (② → ③).
iii. The constant pressure of working fluid with heat rejection (Q_c) to convert condensate in the working fluid, and returning to the initial condition, (③ → ④).
iv. Isentropic compression process of working fluid at low-pressure state turned to be a high-pressure state (P_h). (Reversible adiabatic), (④ → ①).

The efficiency of the Rankine cycle ($\eta_{Rankine}$) can be represented by a ration of total work capacity divided by the total heat into the system:

$$\eta_{Rankine} = \frac{W_t - W_p}{Q_h} \tag{2.4}$$

The Rankine cycle gains higher thermal efficiency, in which the cycle provides two phase changes in the cycle process [10]. In the practical process of Rankine cycle, however, external power input W_p in iv; ④ - ① process is required to achieve the closed thermodynamic cycle as formulated in equation (2.4).

In term of entropy (h), the efficiency for the Rankine cycle can be refined from equation (2.4) by the following equation:

$$\eta_{Rankine} = \frac{(h_2 - h_3) - (h_1 - h_4)}{h_2 - h_1} = 1 - \frac{h_3 - h_4}{h_2 - h_1} \tag{2.5}$$

Typical efficiency for the steam Rankine cycle with superheated ranges from around 20% - 35% [11].

This cycle is considered to the subcritical cycle due to the fact that the processes of heat absorption and rejection to/from the cycle lie at the pressures below the critical pressure, which causes that at the same time it lies at constant temperatures in part [12]. In the case of supercritical Rankine cycle, the heat extraction process takes place at a pressure below the critical pressure, whereas the heat input process takes place at a pressure higher than the critical pressure, which it is explained in next section.

2.1.4 Supercritical Rankine cycle

In the selection of appropriate practical working substance, the working fluid, which has relatively low critical temperature and pressure, is to be used in the Rankine cycle when operating in the supercritical region [13]. The working fluid is compressed to achieve its supercritical state over critical point to obtain higher efficiency (with higher heat transfer mode in the heating process ① - ②) in supercritical Rankine cycle as shown in Figure 2.3.

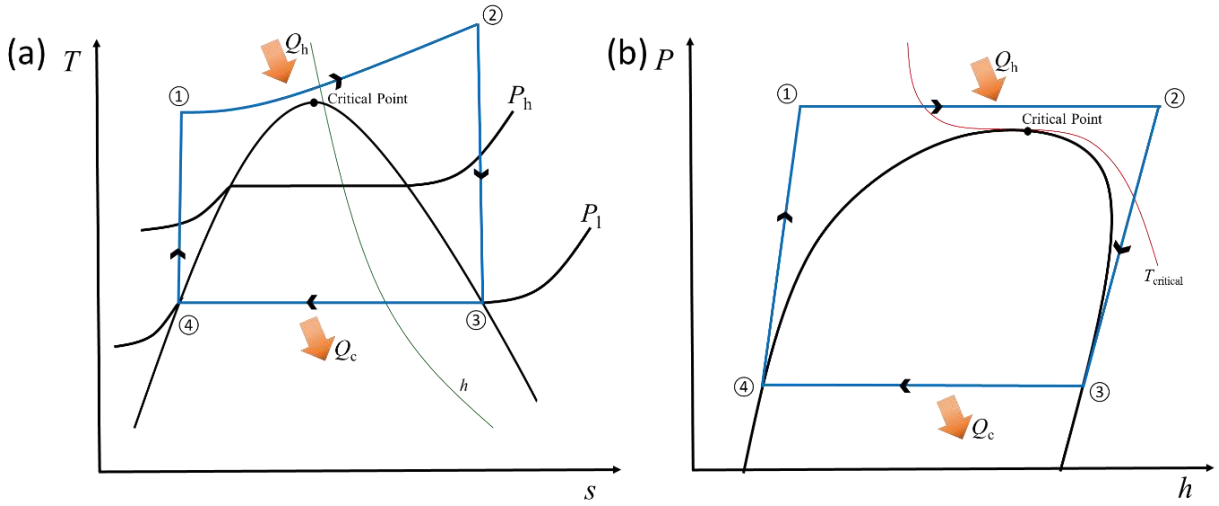

Figure 2.5. (a) *T-s* diagram and (b) *P-h* diagram of supercritical Rankine cycle.

The diagrams of supercritical Rankine cycle of *T-s* and *P-h* diagram are drawn in Figure 2.5 (a) and (b) respectively. Different from the ideal Rankine cycle as shown in Figure 2.4, working fluid is heated and compressed to high pressure and temperature to reach the supercritical state, where a high-mode phase change occurs in the process of heating ① - ②. Then, supercritical working fluid at ② passes through the turbine in adiabatic expansion process (② - ③) for power generation (W_t). As shown in Figure 2.5 (a) and (b), the supercritical Rankine cycle is the trans-critical cycle, where the critical point is included inside of the closed loop (cycle).

In consideration of realizing the supercritical Rankine cycle, which should be the most effective with efficient power generation cycle as described above, CO_2 would be the choice for the purpose in the present study, owing to the low temperature critical point of CO_2 for low temperature heat source of Rankine cycle.

2.2 Gas behavior

Thus far, in an ordinary power cycle, the ideal gas is usually agreed to explain the change of thermodynamic state in a power cycle. However, at the state of high temperature and high pressure such as the supercritical state, the behavior of real gas deviates significantly from the ideal gas [13].

For one mole of real gas;

$$\frac{PV}{RT} \to 1_{\mathrm{limit}P \to 0} \tag{2.6}$$

where P is pressure, V is volume, R is gas constant and T is temperature.

It can be seen that when the pressure of the gas is approached to zero, the behavior of real gas will be similar to the ideal gas, with which the ideal gas law can be defined as

$$PV = RT \tag{2.7}$$

In an extension of equation (2.7), the deviation of real gas from the ideal gas can be considered by the compressibility factor (Z) by comparing the volume of 1 mole of real gas with the molar volume of an ideal gas at the same temperature and pressure condition ($PV = ZRT$). The compressibility factor can be defined as

$$Z = \frac{\text{molar volume of real gas at same } T \text{ and } P}{\text{molar volume of ideal gas at same } T \text{ and } P} = \frac{PV}{RT} \tag{2.8}$$

For real gas, Z may be higher or lesser than one. If the value of Z is close to one, it means the real gas behaves like an ideal gas. If the value of Z is higher than one, it means the gas is less compressible. On the other hand, the gas is more compressible when Z is lesser than one.

In this section, the compressibility factor for carbon dioxide (CO_2) is calculated using the equation of state (EOS). Two EOSs are typically provided, which are Peng-Robinson EOS [14] and Angus EOS [15]. The Peng-Robinson EOS was derived theoretically, while the Angus EOS obtained the value from the curve fit from the experimental data. Also, the Angus EOS is the based equation for the database PROPATH [16], which is used to find the value of CO_2 in a review of the present work.

2.2.1 CO_2 compressible factor calculated from the Peng-Robinson EOS [14]

The Peng-Robinson EOS;

$$P = \frac{RT}{V-b} - \frac{a(T)}{V(V+b)+b(V-b)} \tag{2.9}$$

which can be written in term of Z as

$$Z^3 - (1-B)Z^2 + (A - 3B^2 - 2B)Z - (AB - B^2 - B^3) = 0 \tag{2.10}$$

where

$$A = \frac{aP}{R^2T^2} \tag{2.11}$$

$$B = \frac{bP}{RT} \tag{2.12}$$

$$Z = \frac{PV}{RT} \tag{2.13}$$

Term of A and B at any temperature;

$$a(T) = a(T_c)\alpha(T_r, \omega) \tag{2.14}$$

$$b(T) = b(T_c) \tag{2.15}$$

where,

$$a(T_c) = 0.45724 \frac{R^2 T_c^2}{P_c} \tag{2.16}$$

$$b(T_c) = 0.07780 \frac{RT_c}{P_c} \tag{2.17}$$

and

$$\alpha(T_r, \omega) = 1 + (1 - T_r^{1/2})(0.37464 + 1.54226\omega - 0.26992\omega^2) \tag{2.18}$$

2.2.2 CO_2 compressible factor calculated from the Angus EOS [15]

The compressibility factor for CO_2 was calculated from the state equation;

$$P = \rho RTZ \tag{2.19}$$

in which Z (Angus EOS) is given as

$$Z = 1 + \frac{\rho}{\rho_c} \sum_{i=1}^{6} \sum_{j=1}^{9} a_{ij} \left(\frac{\rho}{\rho_c} - 1 \right)^i \left(\frac{T_c}{T} - 1 \right)^j \tag{2.20}$$

where ρ_c = 468 kg/m^3 and T_c = 304.2 K, which are CO_2 critical density and critical pressure, respectively, the coefficients a_{ij} of Angus EOS for CO_2 is tabulated in Table 2.1.

Table 2.1. Coefficients for a_{ij} [15].

i \ j	0	1	2	3	4	5	6
0	-0.725854437	-1.68332974	0.259587221	0.376945574	-0.67075537	-0.871456126	-0.149156928
1	0.447869183	1.26050691	5.96957049	15.4645885	19.4449475	8.64880497	0
2	-0.172011999	-1.83458178	-4.61487677	-3.81121926	3.6171349	4.92265552	0
3	0.004463049	-1.76300541	-11.1436705	-27.8215446	-27.168572	-6.42177872	0
4	0.255491571	2.37414246	7.50925141	6.61133318	-2.4266321	-2.57944032	0
5	0.05946673	1.16974683	7.4370641	15.0646731	9.57496845	0	0
6	-0.14796001	-1.69233071	-4.68219937	-3.13517448	0	0	0
7	0.013671044	-0.10049233	-1.63653806	-1.87082988	0	0	0
8	0.039228458	0.441503812	0.88674197	0	0	0	0
9	-0.01198721	-0.084605195	0.046456437	0	0	0	0

In comparison, the Angus EOS has more advantages compared with Peng-Robinson EOS in accuracy to represent measured CO_2 data. In this thesis, all properties of CO_2 are obtained and calculated based on the PROPATH [16], which have been cited from the IUPC Table [15].

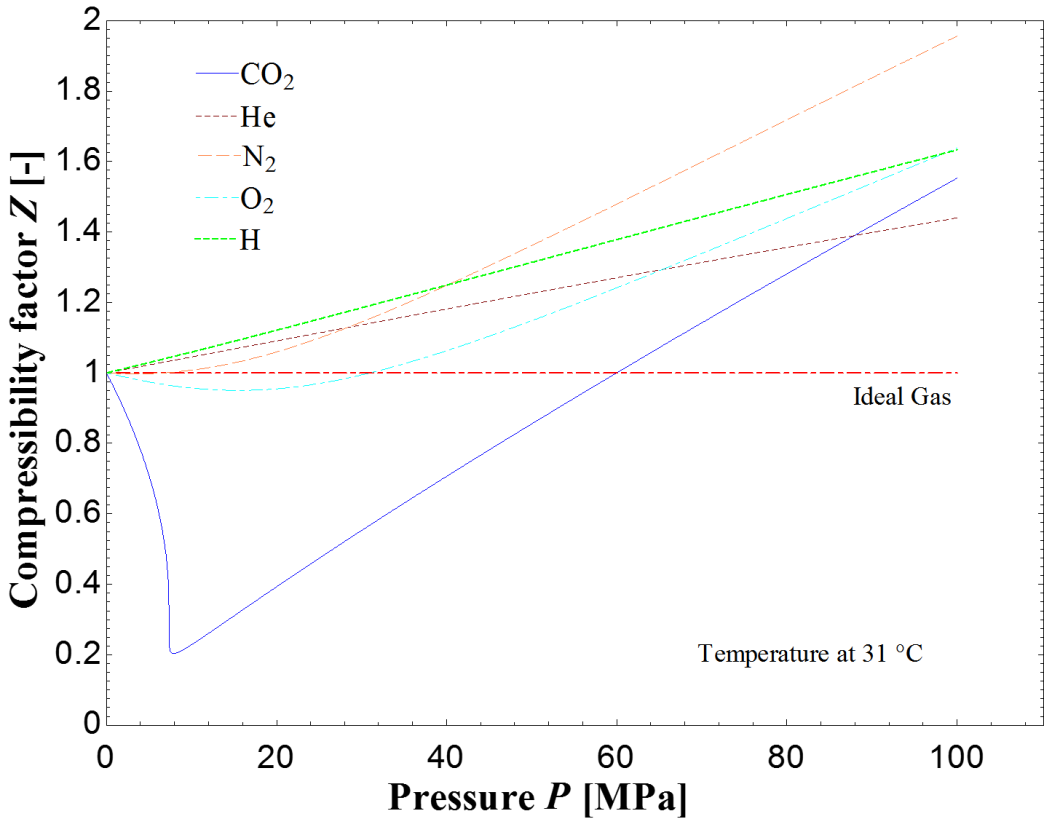

Figure 2.6. The compressibility factor (Z) of various working fluids with pressure.

Figure 2.6 shows plots of the compressibility factor of various working fluid with higher pressure range. It can be seen that the ideal gas law is not suitable to describe the behavior of real gas as the pressure being a higher range. Hydrogen (H) and Helium (He), Z are greater than one for all pressure state, while other working fluids (Nitrogen (N_2) and Oxygen (O_2)), Z are lower than one at relatively lower pressure and greater than one at high-pressure state, which means these working fluids are more compressible and less compressible at lower and higher pressure states, respectively. In the case of CO_2, on the other hand, the pressure increases largely as Z decreases to a minimum, the value of which is approximately 0.27 at the critical temperature and pressure point [17]. At higher pressure, Z is kept at above one, where CO_2 is no longer compressible. At this condition, specific volume becomes smaller, while the density becomes greater compared with Z being lower than one.

In a real gas, heat absorbing and emitting occur, when it undergoes two separate phase changes in an energy conversion process such as in an ordinary Rankine cycle. When the phase change process occurs in a real gas, the internal energy and kinetic energy of the real gas are changed [18]. The phase change of real gas refers to the molecular bond energy, while the temperature of the real gas is kept at constant. Figure 2.7 (a) is a plot of the enthalpy with the temperature variation (constant pressure at 6 MPa), it is seen during the phase change, heat is added to the working fluid without an increase in temperature, the presence of the latent heat as it observed in an ordinary Rankine cycle before superheating. The phase change is shown in Figure 2.7 (a) can be considered as a first order phase transition. However, in the supercritical Rankine cycle, the heat absorbing with enthalpy change (for temperature variation with constant pressure at 9 MPa) occurs as indicated in Figure 2.7 (b), where CO_2 undergoes liquid to supercritical states (as this process is explained in details in later section), while heat emitting process follows the same as an ordinary phase change without constant temperature process, no latent heat exists. In the case of Figure 2.7 (b), it is similar to a higher order phase transition. However, it is not considered as a phase transition phenomenon [19~20]. The phase transition could not exist in the supercritical region, only properties transition can be observed.

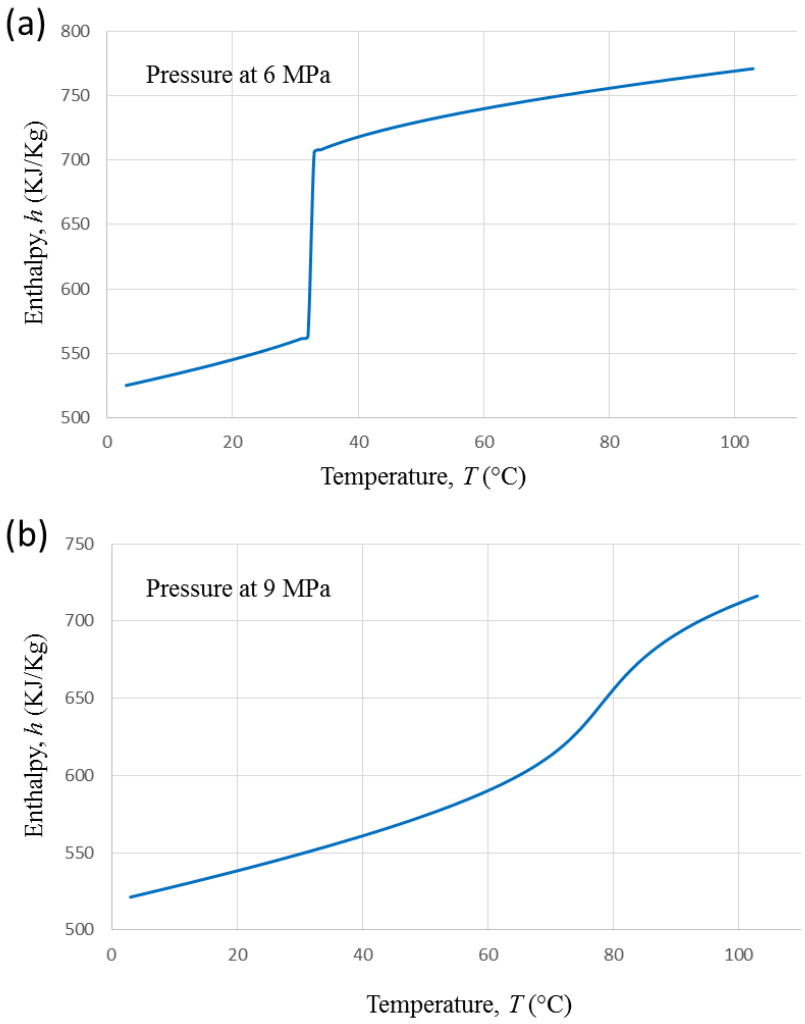

Figure 2.7. Enthalpy for CO_2 temperature variation at (a) 6 MPa and (b) 9 MPa.

As explained earlier, CO_2 used as a working fluid is operated at supercritical state in the Rankin cycle, in which properties are much different from the ideal gas state (ideal gas as a working fluid). In the following section, the properties of CO_2 are discussed and clarified in detail, in which the unique properties of CO_2 in its supercritical state is focused in detail.

2.3 CO_2 in a supercritical state

CO_2 has been regarded as a promising next-generation working fluid for various purposes due to its ecological and environmentally safe. Besides of high pressure and temperature supercritical state, which is used in the power generation cycle of Rankine cycle (in this study), it is mentioned here that a dry ice solid-gas state of CO_2 is also an exciting phase for use in a heat pump cycle as a cooling/refrigeration mechanism, such as being investigated in CO_2 cascade refrigeration cycle system. The challenging heat pump system can achieve the temperature below the triple point temperature of CO_2 as - 56.6 °C [21]. The Phase diagram (*P*-*T* diagram) of CO_2 is shown in Figure 2.8 (b), in which the critical point of CO_2 is marked (at temperature of 31.1 °C and pressure of 7.38 MPa), while the sublimation point and the triple point are also marked respectively at -78.5 °C and 0.101 MPa, and -56.6 °C and 0.518 MPa of temperature and pressure.

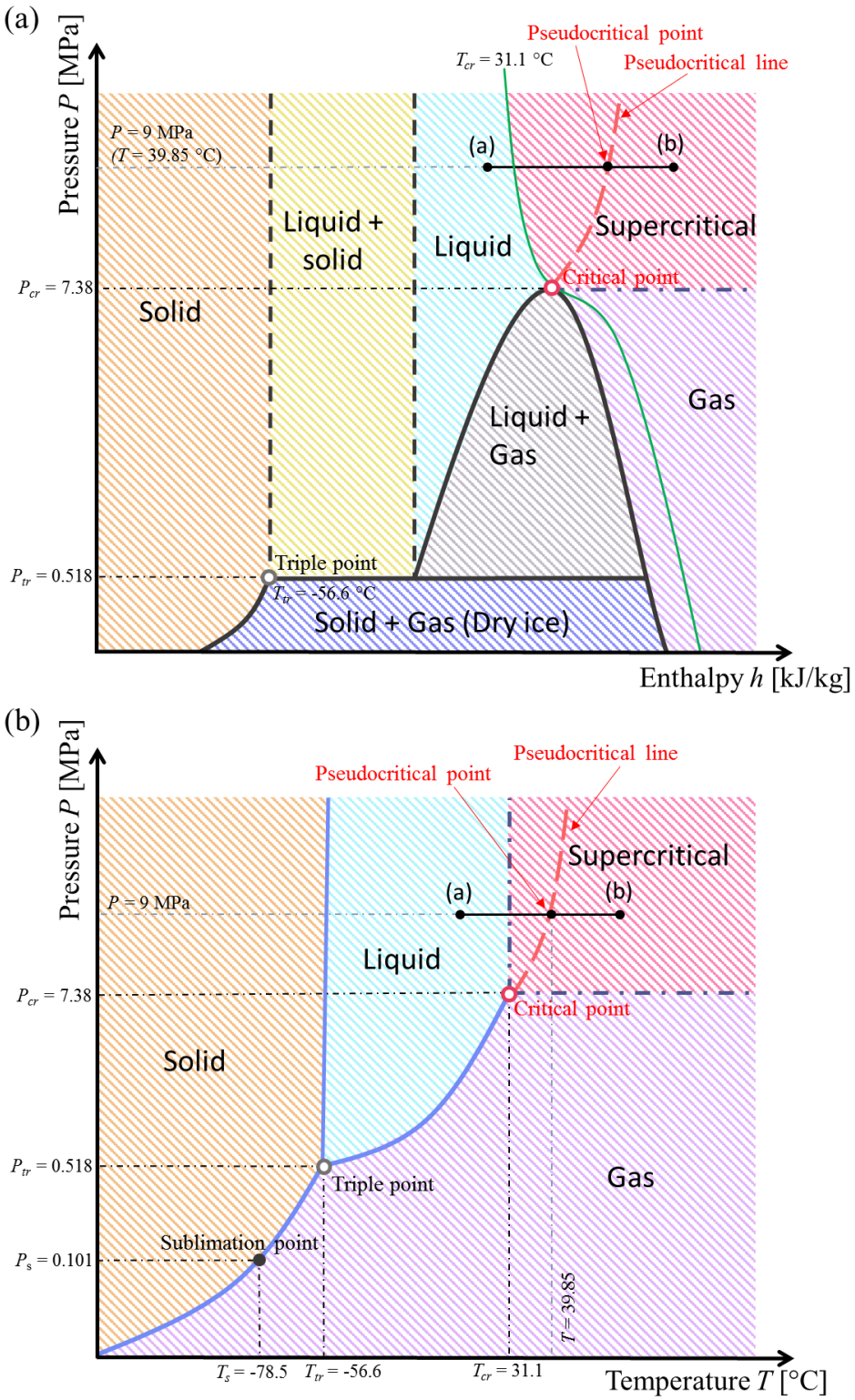

Figure 2.8. (a) Mollier (*P-h*) diagram and (b) Phase (*P-T*) diagram of CO_2.

A supercritical fluid has many different properties compared to regular fluid in general, where the state of the fluid is neither liquid state nor gas state (nor the mixture of the both), but it is a substance in a unique state, which exists above the critical point as shown in Figure 2.8. As also displayed in Figure 2.8 (a) and (b) for respectively Mollier diagram and Phase diagram, the pseudocritical line consists of pseudocritical points, which are the points at a temperature above the critical temperature ($T > T_{cr}$) corresponding to the maximum value of the specific heat at the specific pressure [22]. It is to be

noted that the similar phenomenon of maximum specific heat is also found when liquid CO_2 falls in the saturation line entering gas state at the specific pressure [23]. If a process at a constant pressure (such as described at $P = 9.0$ MPa) undertakes from (a) to (b), say the line (a) – (b), a crossing point at which the line (a) – (b) crosses the pseudocritical line, is so called the pseudocritical point, where the pseudocritical temperature (also called the transposed critical temperature) $T_{pc} = 39.85$ °C. Through the temperature at the pseudocritical point, when $T < T_{pc}$, the supercritical CO_2 behaves like a liquid state with high density named as pseudoliquid, while like a gas state with low density named as pseudogas when $T > T_{pc}$.

Following the path of phase change (pseudo phase transition) of CO_2 in supercritical region, it seems that CO_2 can make a transition from the liquid to the supercritical phase (and in reverse) without a phase traversing boundary, whereas supercritical phase is just simplified the area above critical point (Figure 2.8 (b)). The pseudocritical line can be considered as the saturation line between supercritical like-liquid and like-gas phase or known as pseudoliuid and pseudogas, respectively. As described earlier that the phase change in supercritical state is considered as a properties transition, the maximum of specific heat on the pseducritical point is observed from that the energy from the heat input (increasing in temperature) overcomes the bonds, from pseudoliquid to pseudogas, in which the molecular bonds were broken and be released in the term of kinetic molecular energy, and observed as specific heat. The reason may come from the unique characteristic of supercritical CO_2 in the pseudocritical region that the change of properties along the temperature results in the momentum and buoyant force change in the heat flux direction [24~25]. Furthermore, the details of properties transition through the pseudocritical point is later shown and confirm the phase change phenomenon in the supercritical region by extremely in density change.

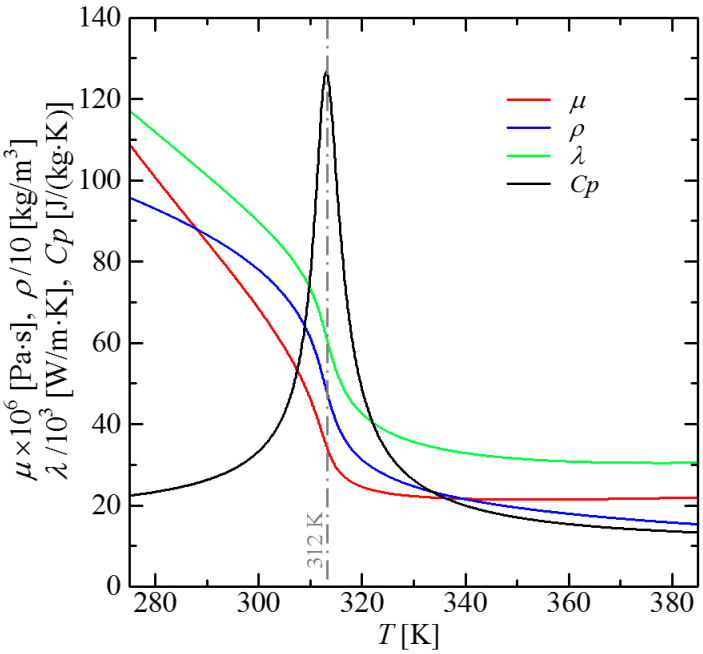

Figure 2.9. Various of thermophysical properties with the temperature at 9 Mpa, density $\rho \times 10^{-1}$ (kg/m^3), specific heat c_p (J/Kg·K), thermal conductivity $\lambda \times 10^{-3}$ (W/m·K) and dynamic viscosity $\mu \times 10^6$ (Pa·s) [26].

The supercritical state CO_2 at 9 MPa, which is a representative operation pressure in the present power cycle, system (SRCS) [26], has the remarkable energy transfer (heat transfer) characteristic in which its thermophysical properties exhibit rapid variation with a change in temperature, especially near the pseudocritical point (around 312 K) as indicated in Figure 2.9. It has the transitions in its properties, such as flow viscosity, thermal conductivity, and density, as the temperature is increased

across the pseudocritical point at the given pressure, all the properties (except for c_p) decrease significantly. On the other hand, the specific heat (c_p) reaches the peak at the pseudocritical point. This characteristic brings many different features of heat transfer from the constant properties of ordinary fluids. It should be noted that, when the temperature increases higher than the pseudocritical region, CO_2 has slowly changed in its properties, i.e., specific heat and density become smaller, while viscosity and thermal conductivity increase along the temperature variation due to the reason that supercritical CO_2 has highly compressible. The charge of characteristic properties of supercritical CO_2 at 9 MPa is shown in Figure 2.9, calculated from PROPATH [16].

The forced convection heat transfer is a high mode of transferring the thermal energy of working fluid in the power cycle under consideration (the supercritical Rankine cycle) since the heat transfer efficiency in the forced convection heat transfer can be largely increased by operating the working fluid at a supercritical region. In the supercritical region, working fluid behaves much different, as seen in Figure 2.9, from an ordinary power cycle operation condition. The significant change in the fluid properties enhances the convection heat transfer coefficient of working fluid in the supercritical Rankine cycle, particularly the change in specific heat (c_p) as described below [27].

Figure 2.10 shows the temperature dependence of specific heat (c_p) of CO_2 at various pressures. It can be seen that the specific heat is substantially increased at critical region (7 – 8 MPa) and the critical pressure point (7.38 MPa), the specific heat goes much larger beyond the other values. By using CO_2 as a working fluid in the power cycle, the operation temperature and pressure is critical factors to achieve the highest output energy value as the specific heat is one of the significant factors in heat transfer process. The Prandtl number (as defined $Pr = \nu/\alpha$ where ν and α are the momentum diffusivity rate and thermal diffusivity, respectively) of CO_2, which is used to measure the heat transfer effectiveness regarding fluid properties of the thermal conductivity and specific heat, is used to examine the convective heat transfer coefficient in the supercritical region. Similarly to Figure 2.10, in Figure 2.11, the temperature variation of the Prandtl number of CO_2 at various pressures are plotted at the supercritical region, the Prandtl number goes to a high peak, in which it can be confirmed that the higher convective heat transfer coefficient of CO_2 at the pseudocritical point can be feasibly acclaimed [28].

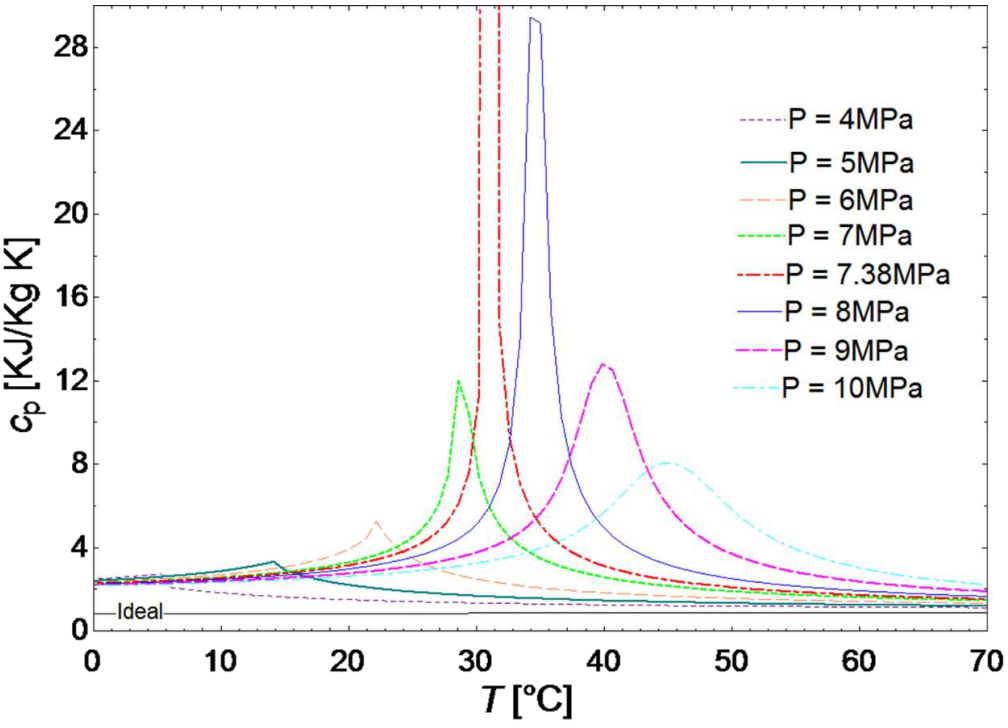

Figure 2.10. Specific heat (c_p) of CO_2 with various pressure.

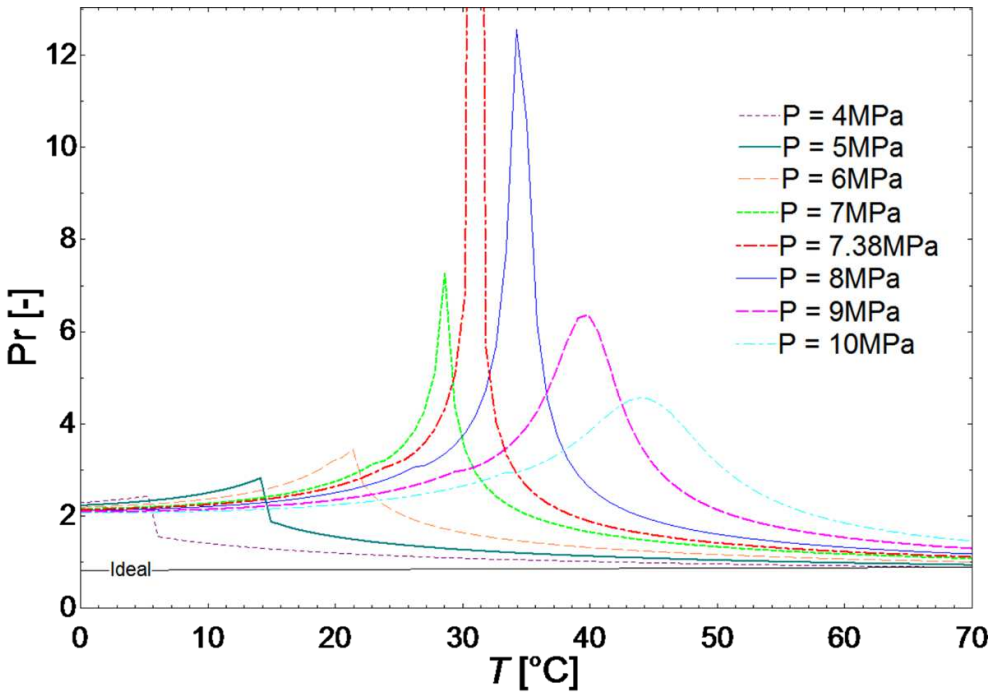

Figure 2.11. Prandtl number (Pr) of CO_2 under various pressure.

From the maximum of specific heat and Prandtl number observe in Figure 2.10 and 2.11, respectively, the peaks at each specific temperature condition occur at the molecular bonds of CO_2 are broken. In the case of CO_2 pressure lower than the critical pressure, the peaks are found when CO_2 starts to change its phase from liquid to gas (1st order phase transition) while at the critical pressure (P = 7.38 MPa), the peak gives the highest as the critical point or so-called a second order phase transition. For the CO_2 in the supercritical region, as mentioned above, peaks give in the pseudocritical points, which are the properties transition. To enhance the high heat transfer properties in the supercritical region, CO_2 gives the promised performance to the cycle with its supercritical state.

References

[1] Short, B.E., 1953. *Engineering thermodynamics*. Harper.
[2] Rennó, N.O. and Ingersoll, A.P., 1996. Natural convection as a heat engine: A theory for CAPE. *Journal of the Atmospheric Sciences*, *53*(4), pp.572-585.
[3] Beér, J.M., 2007. High efficiency electric power generation: The environmental role. *Progress in Energy and Combustion Science*, *33*(2), pp.107-134.
[4] Bass, J.C., HIZ TECHNOLOGIES Inc, 1997. *Thermoelectric generator for motor vehicle*. U.S. Patent 5,625,245.
[5] Curzon, F.L. and Ahlborn, B., 1975. Efficiency of a Carnot engine at maximum power output. *American Journal of Physics*, *43*(1), pp.22-24.
[6] Chen, L., Sun, F., Wu, C. and Kiang, R.L., 1997. Theoretical analysis of the performance of a regenerative closed Brayton cycle with internal irreversibilities. *Energy Conversion and Management*, *38*(9), pp.871-877.
[7] Callendar, H.L., 1910. The caloric theory of heat and Carnot's principle. *Proceedings of the Physical Society of London*, *23*(1), p.153.
[8] Frank, S.E., 1940. *Steam generator or water heater*. U.S. Patent 2,218,898.
[9] Kapooria, R.K., Kumar, S. and Kasana, K.S., 2008. An analysis of a thermal power plant working on a Rankine cycle: A theoretical investigation. *Journal of Energy in Southern Africa*, *19*(1), pp.77-83.
[10] Winterbone, D.E., Advanced thermodynamics for engineers, 1997. *Arnold, London*, p.64-84.

[11] Hough, S., 2009. Supercritical Rankine Cycle. *University of Idaho. Technical Paper. ME-517 http://www. if. uidaho. edu/~ gunner/ME443-543/HW/rankine. pdf*.
[12] Mocarsk, S., and Borsukiewicz-Gozdur, A. (2015). Selected aspects of operation of supercritical (transcritical) organic Rankine cycle. *Archives of Thermodynamics*, *36*(2), 85-103.
[13] Wakefield, C.B., 1996. *Non ideal gas behavior* (No. CONF-960220--). University of Central Oklahoma, Edmond, OK (United States).
[14] Peng, D.Y. and Robinson, D.B., 1976. A new two-constant equation of state. *Industrial & Engineering Chemistry Fundamentals*, *15*(1), pp.59-64.
[15] Angus, S., Armstrong, B. and De Reuck, K.M., 1976. Carbon Dioxide: International Thermodynamic Tables of the Fluid State-3. *Carbon Dioxide: International Thermodynamic Table of the Fluid State*.
[16] PROPATH Group, 1997. PROPATH: a program package for thermophysical properties.
[17] Ahmed, T., 2006. Reservoir engineering handbook Gulf Professional. *Burlington, MA, USA*.
[18] Rogers, G.F.C. and Mayhew, Y.R., Engineering Thermodynamics, Work and Heat Transfer, 1992.
[19] Zhu, J., Zhang, P., Wang, H. and Site, L.D., 2014. Is there a third order phase transition for supercritical fluids?. *The Journal of chemical physics*, *140*(1), p.014502.
[20] Wang, H., Site, L.D. and Zhang, P., 2011. On the existence of a third-order phase transition beyond the Andrews critical point: A molecular dynamics study. *The Journal of chemical physics*, *135*(22), p.224506.
[21] Yamaguchi, H., Zhang, X.R. and Fujima, K., 2008. Basic study on new cryogenic refrigeration using CO_2 solid–gas two phase flow. *international journal of refrigeration*, *31*(3), pp.404-410.
[22] Kawai, S., 2016. Direct numerical simulation of transcritical turbulent boundary layers at supercritical pressures with strong real fluid effects. In *54th AIAA Aerospace Sciences Meeting* (p. 1934).
[23] Poling, B.E., Prausnitz, J.M., John Paul, O.C. and Reid, R.C., 2001. *The properties of gases and liquids* (Vol. 5). New York: Mcgraw-hill.
[24] Hoffmann, H.J., 2008. Phase diagrams beyond the critical point. *Materialwissenschaft und Werkstofftechnik*, *39*(7), pp.455-459.
[25] Yang, J., Ma, Y., Liu, S. and Zeng, X., 2006, May. Comparison investigation on the heat transfer characteristics for supercritical CO_2 fluid and conventional refrigerants. In *Proceedings of the 7th IIR Gustav Lorentzen Conference on Natural Working Fluids, Trondheim, Norway* (pp. 28-31).
[26] Zhang, X.R., Yamaguchi, H., Uneno, D., Fujima, K., Enomoto, M. and Sawada, N., 2006. Analysis of a novel solar energy-powered Rankine cycle for combined power and heat generation using supercritical carbon dioxide. *Renewable Energy*, *31*(12), pp.1839-1854.
[27] Yunus, C.A. and Afshin, J.G., 2011. *Heat and mass transfer: fundamentals and applications*. McGraw-Hill Higher Education.
[28] Yamaguchi, H., 2008. *Engineering fluid mechanics* (Vol. 85). Springer Science & Business Media.

Chapter 3

Basic feature of supercritical CO_2 solar Rankine cycle system and its development on key elements

As mentioned in the properties of CO_2 in supercritical state and energy conversion cycle, the using CO_2 as working fluid in the thermo-fluid cycle can also be considered as one way of preventing the global warming. The gases emitted from industrial plants or transportation system will be recycled by separating CO_2 from other gas with membrane technology or other means. After CO_2 purification process, CO_2 will be stored in gas bottle or cylinder in convenient. CO_2 can be efficiently supplied to the user and used as working fluid for the thermo-fluid cycle for generating energy as power output and/or supplying thermal (heat) energy in household usage [1].

Figure 3.1. The outlook of supercritical CO_2 solar Rankine cycle system.

In term of protecting the world environment and sustainable development, the application of renewable energies to electric power generation and thermal energy supplies are the key to success [2]. The renewable energy has been promoted for decades and more, and various researchers have worked on developing and improving new combined power/heat thermo-fluid cycle. In 2004, supercritical CO_2 solar Rankine cycle system (SRCS), which utilizes solar energy as the energy source and CO_2 as working fluid originally was designed, constructed and developed from the analytical result that the system efficiency would be higher than that of the ordinary photovoltaic cell (PV solar cell). This system has been originally installed on the rooftop of the Energy Conversion Research Center at Doshisha University, Kyoto, Japan as seen in Figure 3.1 [3].

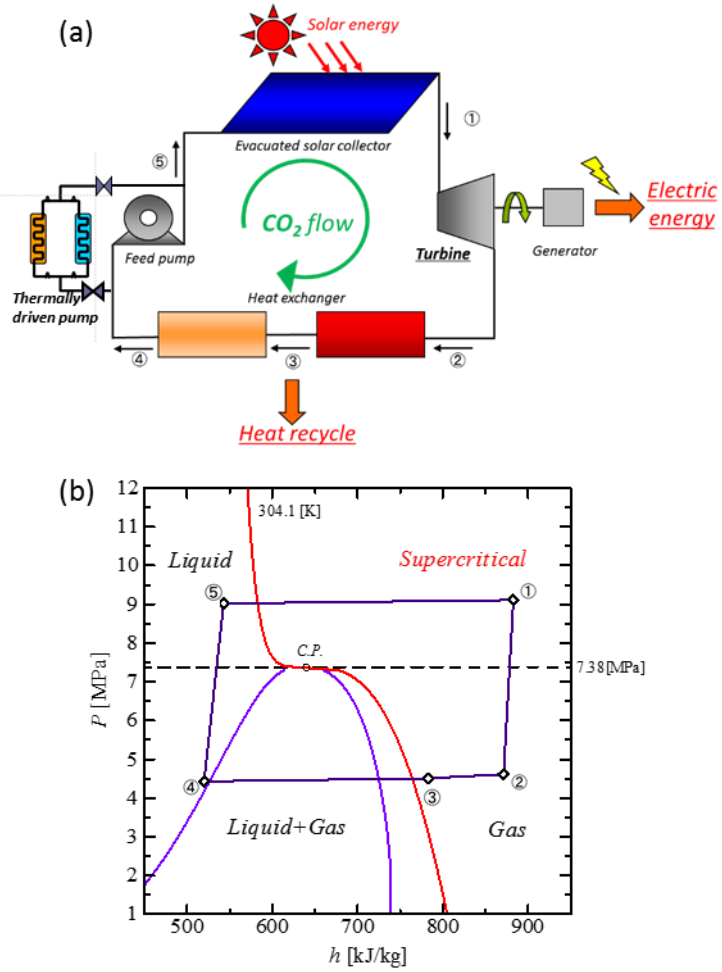

Figure 3.2. Supercritical CO_2 Solar Rankine cycle system: (a) the schematic diagram and (b) *P-h* diagram (cycle diagram).

3.1 Outline of supercritical CO_2 solar Rankine cycle system

Similar to the supercritical Rankine cycle as mentioned in last chapter, the present SRCS is composed of four main components, namely evacuated solar collector, turbine, heat exchanger units, mechanical feed pump (or lately a thermally driven pump, added in parallel arrangement) and also temperature and pressure sensors are installed to measure in-time data as displayed in Figure 3.2 [4]. The outline of the system is schematically shown in Figure 3.2 (a), and the *P-h* diagram of the cycle is attached in Figure 3.2 (b). From the figures, it can be seen that CO_2 is heated in the evacuated tube solar collector ⑤ → ①, where it becomes supercritical (high temperature and pressure) state (Figure 3.2 (b), state ①). After the heating process, the high-pressure supercritical CO_2 drives the turbine ① → ② to generate an electric power output and expands to the gaseous state (Figure 3.2 (b), state ②). Due to the remaining high-temperature state, the circulation CO_2 is cooled in the high-temperature heat exchanger ② → ③, with which heat energy can be recovered to use as a heat source for the refrigeration cycle (Figure 3.2 (b), state ③). The low-temperature heat exchanger is used to further cool down CO_2 to the liquid state (③ → ④), where the thermal energy is obtained from the process, and heat output can be utilized efficiently for hot water supply or other thermal usages (Figure 3.2 (b), state ④). After leaving the heat exchanger units, CO_2 is pumped back ④ → ⑤ to the evacuated tube solar collector into the high-pressure liquid state (Figure 3.2 (b), state ⑤) by the mechanical feed pump or newly developed thermally driven pump [5]. The primary purpose of the system is to generate an electric power output and to supply the thermal energy as hot water from the solar thermal energy with

environment preservation by combining the renewable energy (solar energy) and ecologically safe working fluid (CO_2) in the perspective of future energy creation in green energy resources.

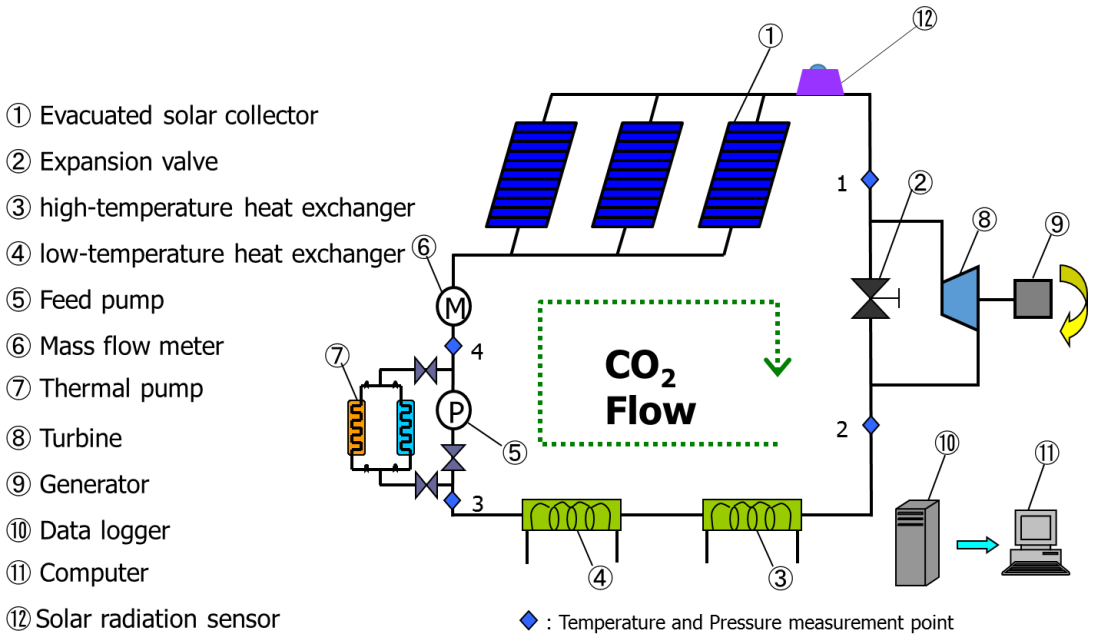

Figure 3.3. Schematic diagram of the experiment facility prototype.

In the development of the original prototype system, however, the supercritical turbine is newly designed and tested, also at the same time, the thermally driven pump is newly manufactured and installed in the system. Those new system elements are described in detail later. The amount of 8 – 13 kg of CO_2 is charged in the system, where the highest operating pressure is designed as 12 MPa. In processing data gained from experiments, the thermo-physical properties of CO_2 are determined referring the measuring data with a Program Package for Thermo-physical Properties of Fluids PROPATH database [6]. Figure 3.3 shows the schematic diagram of the experimental facility of the prototype [4].

3.1.1 Evacuated solar collector

Due to the characteristic of the evacuated tube solar collector, which plays an essential role in the supercritical CO_2 solar Rankine cycle, the functional solar thermal absorption characteristic is required for the successful operation. To efficiently heat CO_2 to a high temperature above the supercritical state, all-glass evacuated U-tube heat removal device, the so-called evacuated solar tube collector, are used, as shown in Figure 3.4. The 15 units of evacuated tube solar collectors were installed, in which each unit consists of 13 U-tubes (4.35 mm of diameter and 3500 mm of total length) with total solar collection active area of 1.43 m^2. These collectors consist of an outer glass envelope (38 mm in diameter) and inner glass envelope (27 mm of inner diameter). The particular surface was employed for the collector tube with a high solar absorptivity of 0.927 and a low emissivity of 0.193 for the temperature at 100 °C with the wavelength of sunlight at 250 to 2000 nm. The transmissivity of the glass envelope is 0.930. The maximum temperature and pressure, to which the evacuated tube solar collector can be durable, is up to 250 °C and 12 MPa, respectively. In the experiment setup, the day measurement and sharing system were installed in the array of the collectors to achieve real-time data measurement, processing, and acquisition [7].

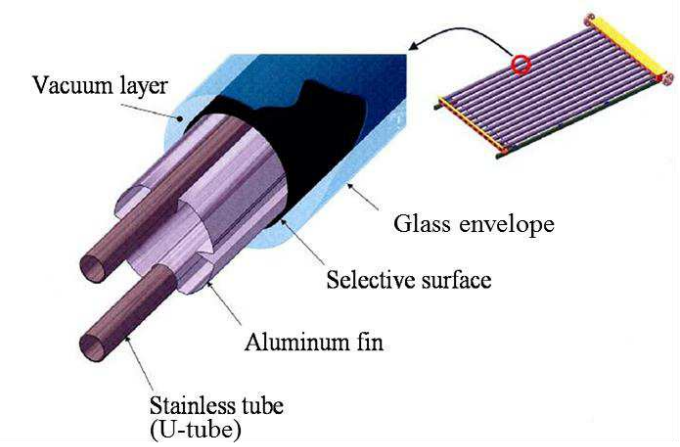

Figure 3.4. A sketch of the evacuated solar collector using in solar Rankine cycle.

3.1.2 Turbine

The turbine is also one of key components in the development of the supercritical CO_2 solar Rankine cycle system to generate electric power output. The outlook profile of a test turbine and its complete assembly are shown in Figure 3.5, and in Figure 3.6, respectively [8]. The test turbine is made of stainless steel SUS304 for enduring high working temperature and pressure during the running operation, also for the sake of avoiding leakage due to the supercritical state of CO_2 at the inlet point of the turbine, in which high temperature, high pressure, and low viscosity state persist. In constructing the test turbine, a magnetic coupling structure is employed as schematically displayed in Figure 3.6, in which magnetic coupling structure has four magnets with each two installed on one side. These magnets are made of neodymium with a dimension of $\varphi 10 \times 20$ mm and 560 mT of magnetic flux. The magneto-electrical rotary and torque detector were installed for examining the rotation speed, rotation speed and the torque of the turbine.

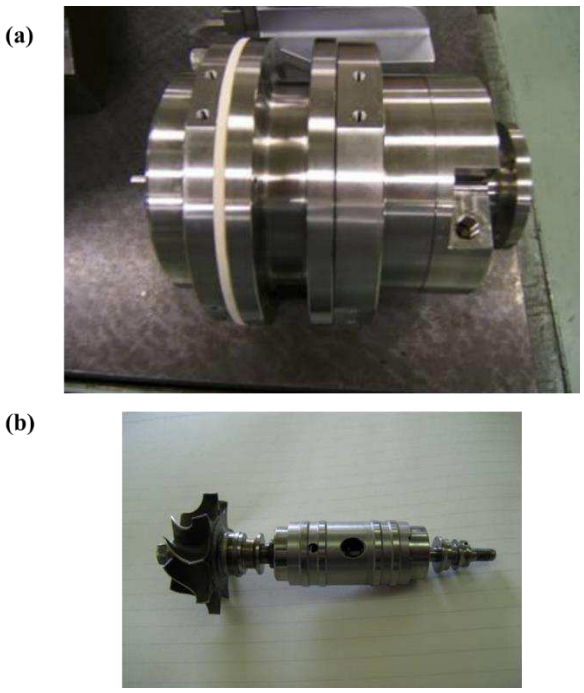

Figure 3.5. The outlook of (a) test turbine and (b) impeller.

The specific design of the turbine for supercritical CO_2 is necessarily required for obtaining high-performance electric power generation from SRCS. The radial turbine, which is intended to be used in the present SRCS, was investigated experimentally and analytically for development of a specific functional design purpose and will be detailed discussed later in this chapter.

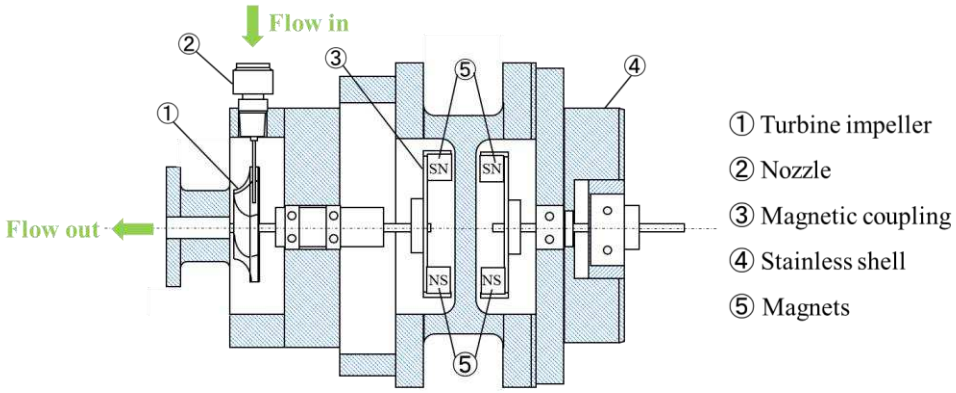

Figure 3.6. Schematic assembly diagram of test turbine.

3.1.3 Heat exchanger units

The heat exchangers are intended to recover heat in the supercritical CO_2 solar Rankine cycle system, in which concurrent CO_2 is cooled to the low-temperature liquid state to complete Rankine cycle. There is two heat exchanger device units in the supercritical CO_2 solar Rankine cycle system. Namely, a high-temperature heat exchanger (HX1) and a low-temperature heat exchanger (HX2) are respectively used to utilize heat as higher temperature water (in the high-temperature heat recovery unit) and lower temperature water (in the low-temperature heat recovery unit). The heat exchanging rate of CO_2 in the CO_2/water heat exchanger is calculated based on the average temperature of the CO_2 side of the heat exchanger. The total heat exchanger area is approximately 0.76 m^2. To achieve the high capability of heat exchanging rate between water and CO_2, the shell and tube design of heat exchanger is selected by tube side of CO_2 and the shell side of the water. Four platinum resistor temperature sensors are installed in heat exchangers to measure inlet and outlet of water temperatures, plus two water flow meters to measure the water outlet flow of each heat exchanger unit.

3.1.4 Mechanical feed pump

A plunger pump (mechanical feed pump) was originally installed for feeding liquid CO_2 to the evacuated tube solar collector in the supercritical CO_2 solar Rankine cycle system [4]. The canned motor plunger pump, specially designed for the purpose with a maximum power output of 750 W×4 pistons (Figure 3.7), which can provide a maximum operating pressure of 12 MPa and 0.03 kg/s of flow rate. The outlook of the mechanical feed pump is shown in Figure 3.8 (a) while the dimension is given in Figure 3.8 (b). The flow rate meter is also installed in the downstream side of the mechanical feed pump to measure and record the mass flow rate of liquid CO_2 from the mechanical feed pump as well as temperature and pressure measuring devices. The flow meter is a type of a Coriolis effect mass flow meter to measure and record the mass flow rate of CO_2, which can endure the maximum operating pressure at 12 MPa as well. Its measurement range is approximately 0.09 – 1.0 kg/min.

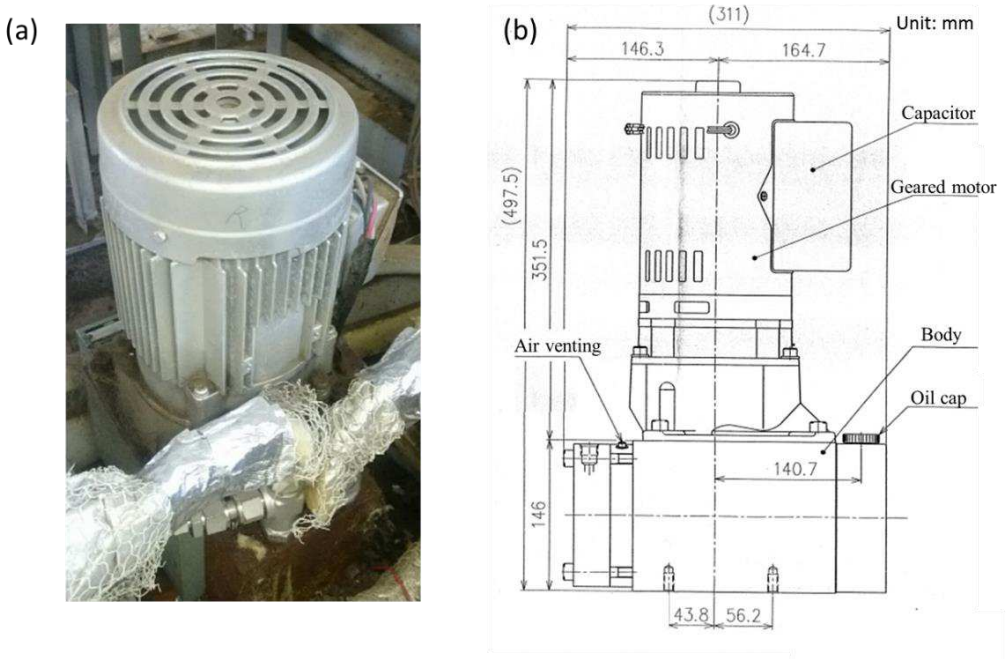

Figure 3.7. Mechanical feed pump (plunger pump): (a) outlook and (b) drawing.

In the typical SRCS, the mechanical feed pump is used to feed liquid CO_2 back to the evacuated solar collector at high-pressure state. However, the mechanical feed pump consumed a very high rate of energy and also has large mechanical loss, which decreases the total efficiency of the system [9]. The thermally driven pump is newly introduced to be used for the replacement of the mechanical feed pump under developing stage of SRCS. The detailed new development in the thermally driven pump will be given in this chapter.

3.2 Development of key elements in supercritical CO_2 solar Rankine cycle system

The performance of supercritical CO_2 solar Rankine cycle system is strongly depended on the appropriate designs of each element. Due to the reasons that the supercritical state of CO_2 has highly compressible with large density and viscosity variation, the specific key elements of system design, namely evacuated solar collector, supercritical CO_2 turbine, and thermally driven pump are investigated for the objective of achieving the best performance of the actual supercritical CO_2 solar Rankine cycle system. It is to be noted here that the development of evacuated solar collector has been referenced to understand the investigation of the key elements [10].

3.2.1 The investigation on evacuated solar collector arrangement

The evacuated solar collector can be arranged in three arrangements, as shown in Figure 3.5, where (a), (b) and (c) are respectively; (a) parallel with each 5 units, (b) cascade with each 5 units in series and (c) 5 units only in series. The performance of SRCS with three independent arrangements of the evacuated solar collector was evaluated by considering the heat collection amount (Q_c), CO_2 mass flow rate ($\dot{m}$) at collector's inlet and temperature (T_1) at the outlet of the evacuated solar collector. Also, the solar radiation intensity (I) is measured for the reference. Q_c is calculated with the enthalpy (h) of CO_2 between inlet and outlet of the evacuated solar collector (as positioned in Figure 3.2 (a) and (b)) obtained from measured temperature and pressure by using PROPATH database [6], the formulas used for the evaluation is as follows [10];

$$Q_c = \int \dot{m}(h_1 - h_4)dt \tag{3.1}$$

The thermal energy (heat) gain from solar radiation (Q_{SR}) was evaluated based on the total solar collective active area and solar radiation intensity, which can be defined as

$$Q_{SR} = \int AIdt \tag{3.2}$$

where A is an active heat collection area.

For calculating the heat collection efficiency η_c can be found by

$$\eta_c = \frac{Q_c}{Q_{SR}} \tag{3.3}$$

The results of heat collection efficiency, solar radiation, CO_2 temperature at the outlet of evacuated solar collector and CO_2 mass flow rate at inlet of evacuated solar collector with optimum time for the SRCS with three arrangements of evacuated solar collector units were obtained and the performance was evaluated on a typical sunny day in winter season of Kyoto, Japan. Figure 3.6 (a) and (b) show the results obtained from an evacuated solar collector with the arrangement of parallel with each five units in series. In Figure 3.6 (a), the amount of solar radiation and heat collection efficiency were plotted for the operation time. In the morning period, the number of solar radiation increases from 0.09 kW/m^2 at the beginning to a high value of 0.5 kW/m^2, and vice versa at noon till the zero at sunset. The heat collection efficiency also increases from the beginning of the operation and stays relatively stable at time 9:00 to 14:00, which is not so depended with the solar radiation at that time, and then decreases to zero at a time around 16:00. Corresponding with Figure 3.6 (a), Figure 3.6 (b) shows CO_2 mass flow rate at the inlet of evacuated solar collector achieved the highest value of approximately 0.6 kg/min during time 9:00 to 14:00. The CO_2 temperature at the outlet of the evacuated solar collector is raised from the beginning from 10 °C to be the highest temperature of 110 °C at 11:30 and decreases to 20 °C at last measuring here.

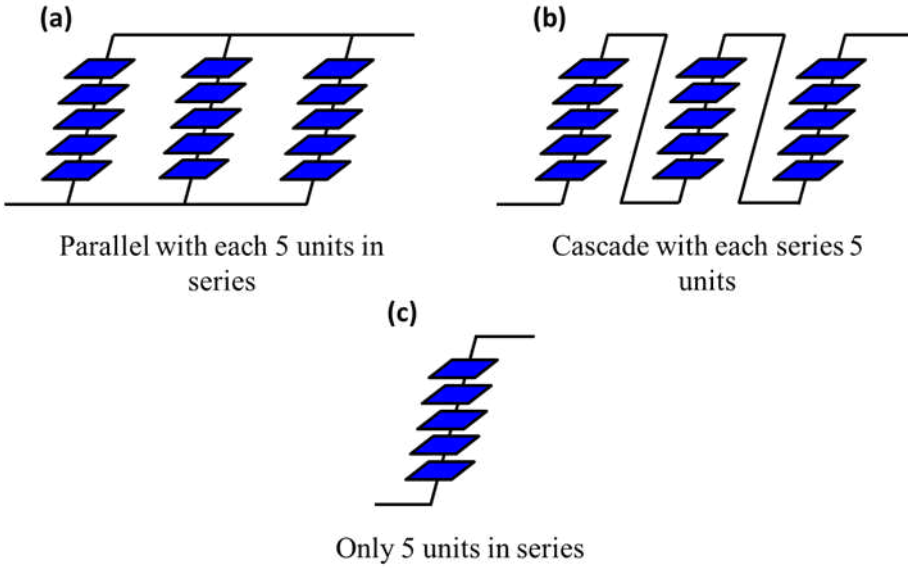

Figure 3.5. Three arrangements of evacuated solar collector [10].

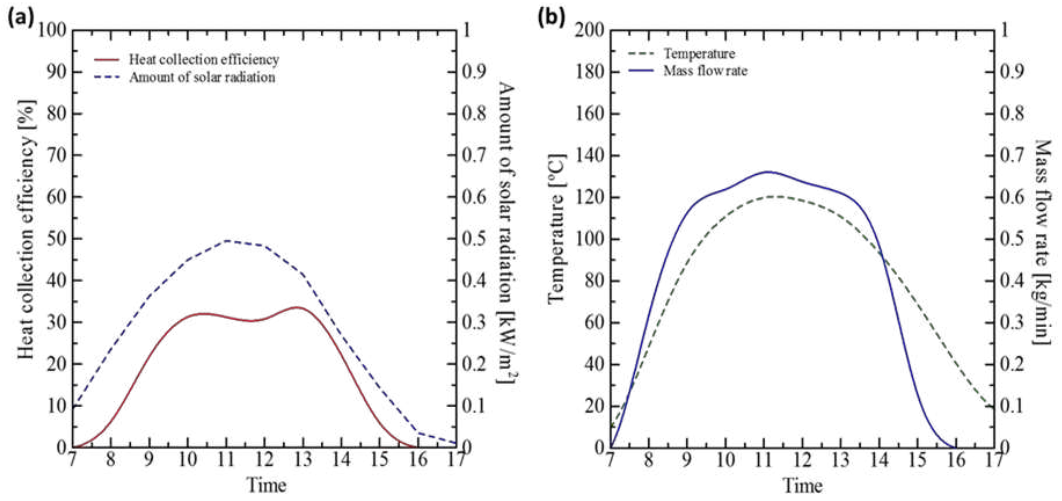

Figure 3.6. (a) Heat collection efficiency and solar radiation, and (b) CO_2 temperature at the outlet of collectors and CO_2 mass flow rate at the outlet of the feed pump against the operation time from 7:00 to 17:00 measured in the SRCS with the solar collector units having parallel arrangement with each 5 units in series [10].

Similar to Figure 3.6, the results of the SRCS with the cascade arrangement of the evacuated solar collector with each series five units are shown in Figure 3.7. It can be found that the results in the cascade arrangement have similar behavior with the parallel arrangement (Figure 3.6). However, the cascade arrangement can be achieved a higher value of heat collection efficiency (40 %), the CO_2 temperature at the outlet of the evacuated solar collector (154.5 °C) and CO_2 mass flow rate at the inlet of the evacuated solar collector (0.75 kg/min) compared with the parallel arrangement.

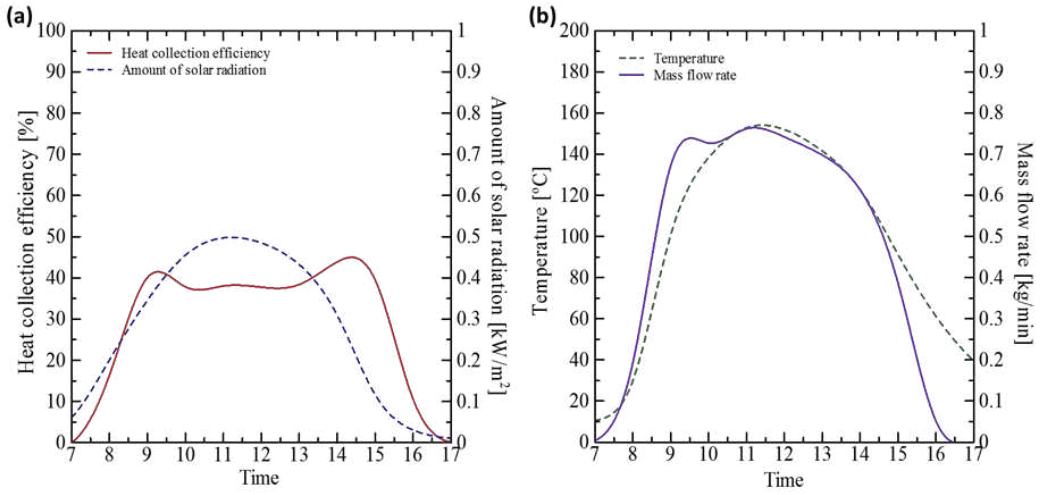

Figure 3.7. (a) Heat collection efficiency and solar radiation, and (b) CO_2 temperature at the outlet of collectors and CO_2 mass flow rate at the outlet of the feed pump against the operation time from 7:00 to 17:00 measured in the SRCS with the solar collector units having cascade arrangement with each 5 units in series [10].

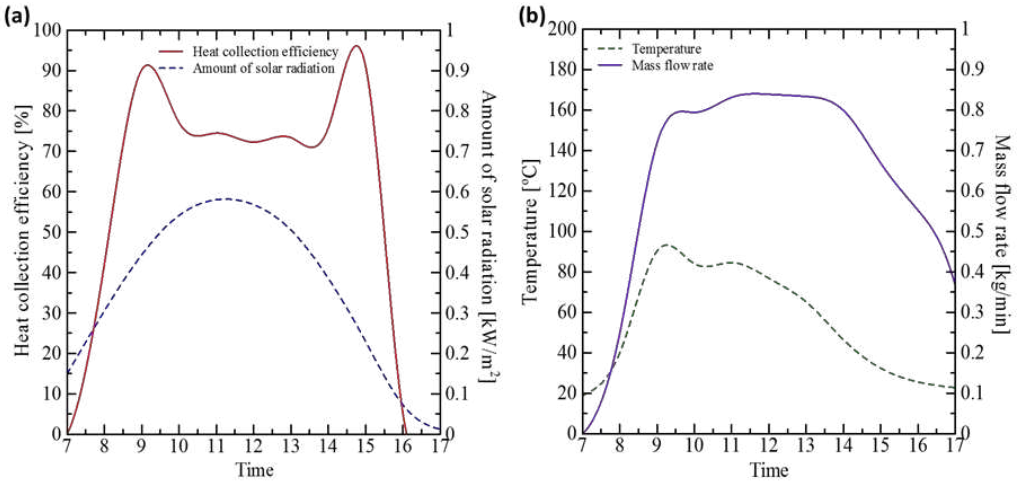

Figure 3.8. (a) Heat collection efficiency and solar radiation, and (b) CO_2 temperature at the outlet of collectors and CO_2 mass flow rate at the outlet of the feed pump against the operation time from 7:00 to 17:00 measured in the SRCS with the solar collector units having only 5 in series [10].

To investigate the effect of heat collection area, Figure 3.8 (a) and (b) show the results of SRCS with the arrangement of the evacuated solar collector in only five units in series. The heat collection efficiency and CO_2 mass flow rate at the outlet of the evacuated solar collector are found much higher than in parallel arrangement (Figure 3.6) and cascade arrangement (Figure 3.7), in which the highest values are obtained as 90 % and 0.85 kg/min, respectively. The reasons may be thought of the fact that the flow pathway of CO_2 in 5 series is shorter than other. Thus the CO_2 mass flow rate is more significant compared with the other two arrangements with the same amount of CO_2 in the system. Therefore, since the heat collection area is smaller than others, the fact leads the CO_2 temperature at the outlet of evacuated solar collector become lower than others with the highest value of 90 °C. From the results of three arrangements for the aim of electric power generation and heat utilization, it can be suggested that the cascade arrangement in series would give high performance in the CO_2 temperature and the CO_2 mass flow rate at outlet and inlet of the evacuated solar collector, respectively.

The performance of evacuated solar collector is not only depended on the construction or collectors' arrangements itself but also on the flow behavior of working fluid (CO_2) inside the evacuated solar collector, in which active forced convection heat transfer is taking place. Moreover, CO_2 particularly near to the pseudocritical point, the supercritical state properties enhance strong convective flows, which improve heat transfer characteristic mainly.

3.2.2 New design aspect for supercritical CO_2 turbine

Turbine is an essential component to generate electric power in the supercritical CO_2 solar Rankine cycle system. To date, there is no literature available for specific turbine design in supercritical CO_2 power generation cycles. Due to the critical state, which is the distinguish state between liquid and gas (or vapor) phase, a specific new design for supercritical CO_2 is strongly required for achieving the best performance of the system. The choked flow in the nozzle of the turbine, which would give a limitation on the supercritical CO_2 flow, was found to occur as Mach number equals to one along the nozzle length, and in effect, it limits the CO_2 flow, and resultantly the efficiency of turbine [11]. The turbine nozzle with various diameter was examined for designing purpose in the study. The results are shown in Figure 3.9. It is found that the choked flow occurred at the diameter of 0.5 mm to 0.6 mm in this particular nozzle design. By 0.5 mm, totally choked flow occurs at the beginning of the entrance region around L = 0.015 m, while for 0.6 mm, the choked flow can be found occurring around 0.016 m

of the nozzle length. It is suggested that the nozzle diameter bigger than 0.6 mm is appropriate for designing this specific supercritical turbine with the specific rotor mode as adapted in the study [12]. It is mentioned here that the approach adopted in the study is valid for any specific design of turbine in this type in general.

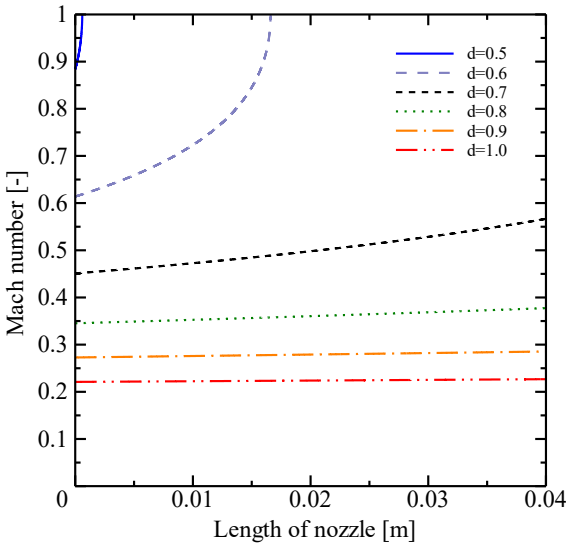

Figure 3.9. Variation of Mach number along with the turbine nozzle [12].

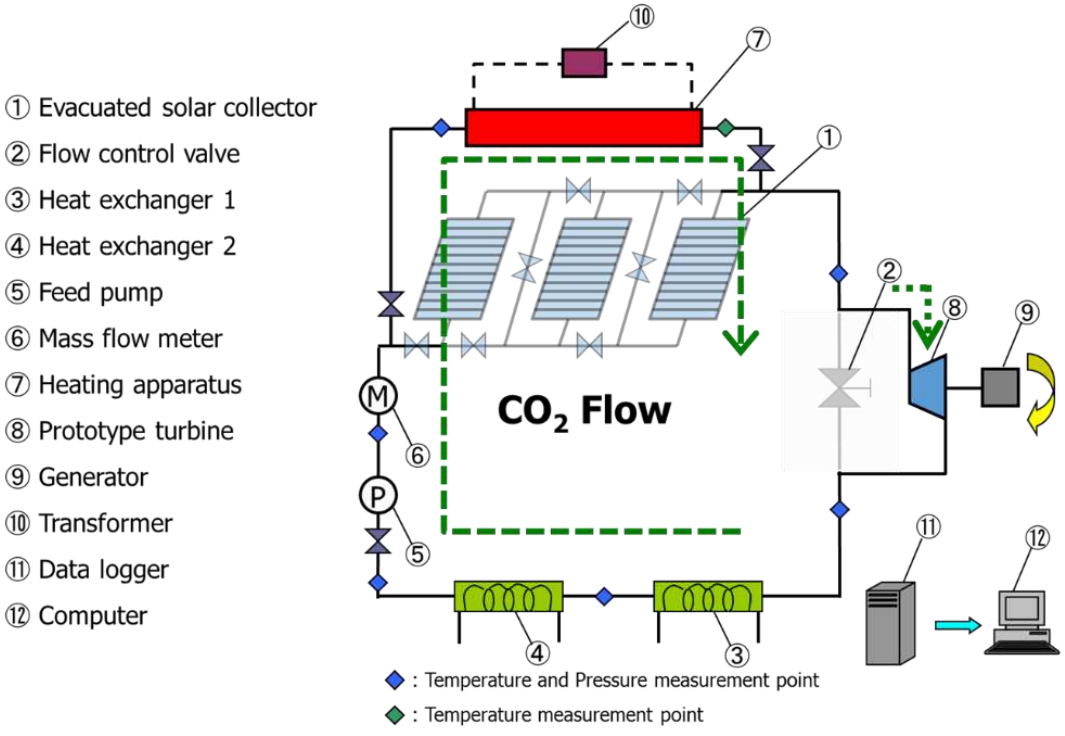

Figure 3.10. Experiment setup for turbine investigation.

In this chapter, the new primary design of turbine is provided to attempt, the length of connecting part is 0.25 inch, and the test nozzle is connected with the flow cycle path from the heating tube (test section), or SRCS evacuated solar collector. The guide vane, which is generally used in the conventional turbine for adjusting the flow angle of fluid is not necessary for this first step of turbine

design; the nozzle is used instead. The new primary design of turbine is attempted by using 1.0 mm of nozzle diameter to avoid the chocked flow with the length of the turbine nozzle at 25, 29 and 33 mm.

Beside of using an evacuated solar collector, as shown in Figure 3.10 for the experiment setup, heating apparatus ⑦ is newly constructed to heat up CO_2 in turbine test experiments to avoid the unstable weather conditions, which had many effects to the supercritical CO_2 solar Rankine cycle system [8]. The experimental (prototype) turbine is schematically displayed in Figure 3.11. T-type thermocouples were installed at the inlet and outlet points of the test turbine to measure in-time data of CO_2 temperature and pressure inside the turbine (Figure 3.11) during experiments. In this system, operation pressure and the temperature are approximately 12 MPa and 30 °C to 200 °C, respectively.

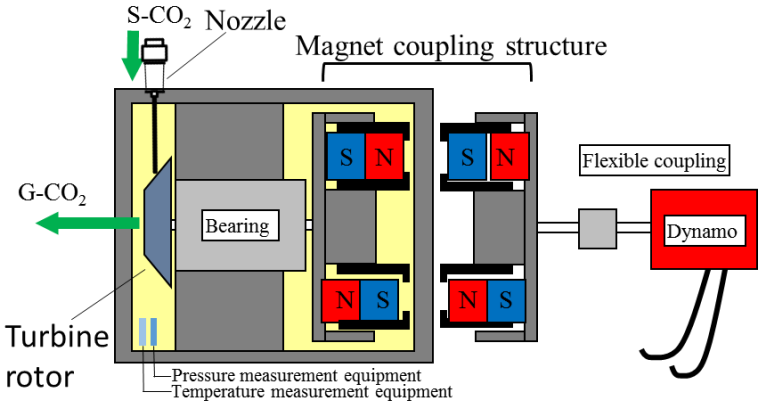

Figure 3.11. Schematic of turbine investigation.

In Figure 3.12 (a), frontal view of the prototype turbine is displayed; the turbine rotor has a commercial centrifugal turbine blade, to which gas-nozzle (in the supercritical state) is attached. The velocity triangle in the turbine is displayed in Figure 3.12 (b), by the tangential nozzle angle to a turbine blade is set at 15 °, and 155.3 ° for inlet β_{in} and outlet β_{out} of the turbine, respectively, where V is tangential fluid velocity and q is fluid velocity. The prototype turbine works as an impulse turbine in the supercritical states. In this work, particular attention is given to the nozzle (performance) to improve turbine rotational speed (resultantly turbine performance itself).

The prototype turbine, by installing the various nozzle configuration (length), was run at the condition summarized in Table 3.1 at a fixed 1.0 mm nozzle diameter. The flow control valve ② controls the mass flow rate (of supercritical CO_2), pressure and temperature to the nozzle (as shown in Figure 3.10) with controlling the heat input by heating apparatus and heat exchanger units ③ and ④.

In parallel with the experiment, a numerical analysis is performed to estimate the nozzle (the same configuration as the experiment) performance. The numerical analysis is based on the one-dimensional compressible gas dynamics, to which Fanno-flow type gas with the condition of constant wall function (viscosity) is assumed throughout the analysis.

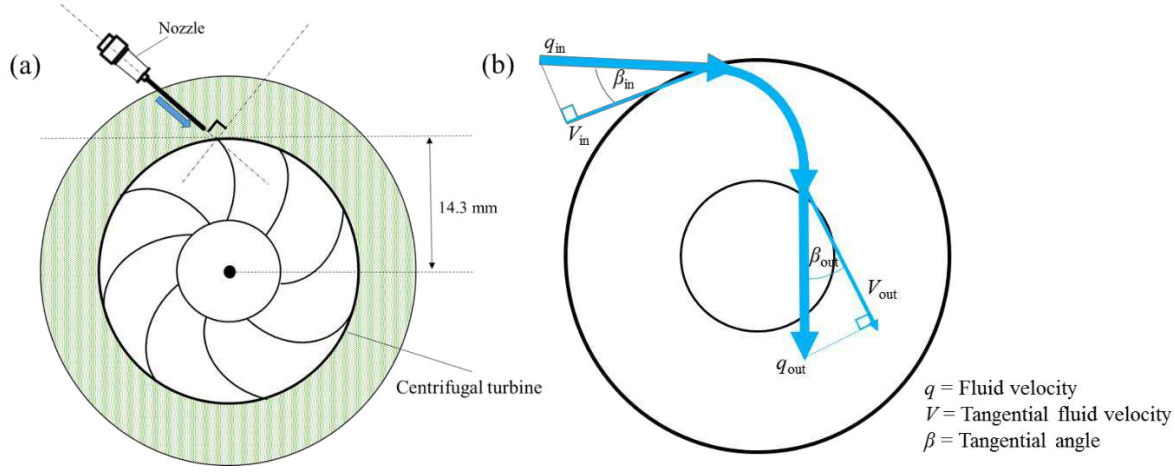

Figure 3.12. Turbine: (a) frontal view of the rotor and nozzle and (b) velocity triangle flow in the turbine.

The structure of the nozzle for experiments is shown in Figure 3.13 (a). At the inlet of the turbine (from the outlet of the nozzle), due to the compressible flow effect, choked flow can occur, and which usually causes decrease the overall efficiency of the turbine. However, as described above, to avoid the choked flow, d_n = 1.0 mm is used for the performance test.

The domain of the nozzle is shown in Figure 3.13 (b), where the length is sub-divided for n = 1000, $d_n = L_n/n$, as L_n is the length and d_n is the diameter. In numerical calculation, the thermo-physical properties of CO_2 are calculated from the PROPATH database [6].

Table 3.1. Turbine test condition (d_n = 1.0 mm)

Nozzle Diameter [mm]	1.0		
Nozzle Length [mm]	25, 29 ,33	25, 29 ,33	25, 29 ,33
Inlet of Turbine Pressure [Mpa]	6.88	6.45	6.20
Outlet of Turbine Pressure[Mpa]	4.64	4.62	4.60
Inlet of Turbine Temperature [°C]	56.1	44.3	38.5
Outlet of Turbine Temperature [°C]	30.3	22.1	19.7
Mass Flow Rate [kg/s]	0.74	0.72	0.54

In the numerical analysis for examining the nozzle, the equation governing the Fanno flow in the nozzle can be given as equations (3.4) ~ (3.6) [13],

$$\frac{d\rho}{\rho}+\frac{du}{u}=0 \tag{3.4}$$

$$\frac{du}{u}+\frac{1}{kM^2}\frac{dp}{p}+\frac{c_f}{2}\left(\frac{4}{d_n}\right)dx=0 \tag{3.5}$$

$$\frac{dT}{T}+(k-1)M^2\frac{du}{u}=0 \tag{3.6}$$

where u is velocity, P is pressure, ρ is density and T is temperature of the flow. M and k are Mach number and specific heat ratio, respectively.

It is noted that in equation (3.5), c_f is Fanning friction coefficient, and in the supercritical state, the factor appeared in equation (3.4) ~ (3.5) is generally unknown. However, for the sake of giving an

estimate to flow state in the nozzle at the first approximation, conventional general treatment of the gas-dynamics equation is adopted in the numerical analysis (all thermo-physical properties at given states are derived from the database PROPATH). The relationship between Fanning friction coefficient and Darcy friction coefficient (λ) can be described $\lambda = 4c_f$, assuming CO_2 as a gaseous state.

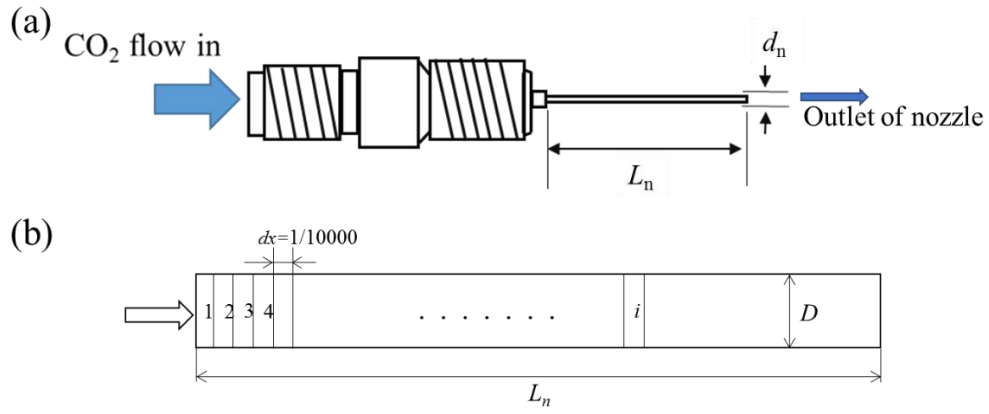

Figure 3.13. Detail of nozzle (a) and numerical calculation model (b).

At the Reynolds number $3\times10^3<Re<10^5$, Darcy friction coefficient is represented connectional by the expression of Blasius [14],

$$\lambda = 0.3164 \times \mathrm{Re}^{-0.25} \tag{3.7}$$

and when $10^5<Re<10^6$, λ is presented by Karman-Nikuradse equation [15],

$$\lambda = 0.0032 + 0.221 \times \mathrm{Re}^{-0.237} \tag{3.8}$$

The pressure P is determined from the state equation of a CO_2 as,

$$P = \rho RTZ \tag{3.9}$$

where Z is the compression factor, which is given by density ρ, CO_2 Temperature T, the critical density ρ_c = 468.0 kg/m^3 and critical temperature T_c = 304.1 K with the following equation,

$$Z = 1 + \frac{\rho}{\rho} \sum_{i=0}^{6} \sum_{j=0}^{9} a_{ij} \left(\frac{\rho}{\rho_c} - 1 \right)^i \left(\frac{T_c}{T} - 1 \right)^j \tag{3.10}$$

In equation (3.10), a_{ij} is CO_2 virial coefficient referred to Table 2.1 in Chapter 2. In order to calculate Mach number in the nozzle, the speed of sound w_s is derived from solution as follows,

$$w_s^2 = \left(\frac{c_p}{c_v} \right) \left(\frac{\partial P}{\partial \rho} \right)_T \tag{3.11}$$

where $(\partial P/\partial \rho)_T$ can be represented by following equation (3.12),

$$\left(\frac{\partial P}{\partial \rho} \right)_T = RT \times \left[1 + 2\omega \sum_{i=0}^{6} \sum_{j=0}^{9} b_{ij} (\tau - 1)^j (\omega - 1)^{i-1} \right] \tag{3.12}$$

It is noted that in equation (3.12), the parameters are defined in such a way that, $\omega = \rho/\rho_c$ and $\tau = T_c/T$. In the numerical analysis, after mathematical manipulation, the following set of equations, equation (3.13) ~ (3.16) are solved by finite difference technique with defining Mach number as M = u/w_s,

$$\frac{du}{u}=\frac{k\mathrm{M}^2\psi}{1-\mathrm{M}^2}\frac{4c_\mathrm{f}}{d_\mathrm{n}}dx,\psi=1+\frac{k-1}{2}\mathrm{M}^2 \tag{3.13}$$

$$\frac{d\rho}{\rho}=-\frac{k\mathrm{M}^2\psi}{1-\mathrm{M}^2}\frac{4c_f}{d_n}dx \tag{3.14}$$

$$\frac{dp}{p}=-\frac{k\mathrm{M}^2\left[1+(k-1)\mathrm{M}^2\right]}{2\left(1-\mathrm{M}^2\right)}\frac{4c_\mathrm{f}}{d_\mathrm{n}}dx \tag{3.15}$$

$$\frac{d\mathrm{M}}{\mathrm{M}}=\frac{k\mathrm{M}^2\left\{(k-1)\mathrm{M}^2+2\right\}}{1-\mathrm{M}^2}\frac{c_\mathrm{f}}{d_\mathrm{n}}dx \tag{3.16}$$

Finally, from the solution of the equation (3.13) ~ (3.16), the maximum length of nozzle L_{max} mm can be calculated by equation (3.17),

$$L_{\max}=\frac{d_\mathrm{n}}{4c_\mathrm{f}}\left\{\frac{1-\mathrm{M}^2}{k\mathrm{M}^2}+\frac{k+1}{2k}\ln\left[\frac{(k+1)\mathrm{M}^2}{(k-1)\mathrm{M}^2+2}\right]\right\} \tag{3.17}$$

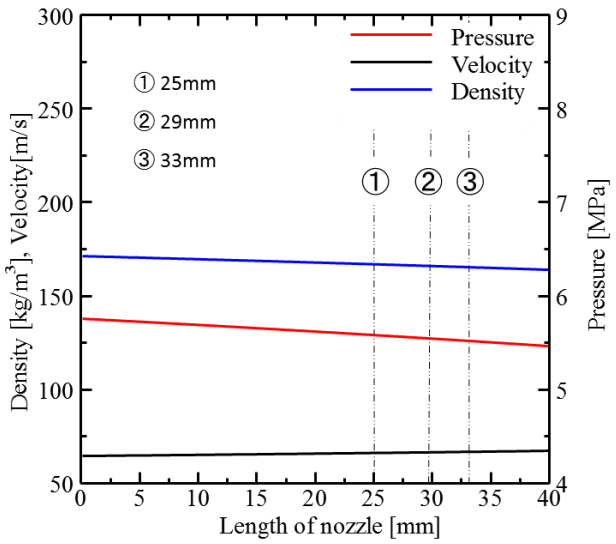

Figure 3.14. Numerical result of CO_2 thermal physical property in nozzle (d_n = 1.0mm).

The performance of the turbine is characterized by various parameters, in which the rotational speed of the turbine is the primary factor (to the turbine's power output) in discussing its performance. Due to the nature of the impulse turbine, which is used in the SRCS, the rotational speed of turbine depends on the pressure and momentum of CO_2 at the inlet of turbine impeller (outlet of the nozzle length). In order to verify the change of flow state inside the nozzle, the CO_2 properties (pressure, velocity, and density) are examined here. Since the phase of CO_2 in the turbine is the supercritical state with high pressure and temperature, it is difficult to measure CO_2 properties directly. To solve this issue, the numerical analysis is performed as formulated shown previously. From the set of governing equation written above, the density, pressure, and velocity are calculated in Figure 3.14, up to the nozzle length of 40 mm by fixing representative nozzle diameter of d_n = 1.0 mm. The conditions used in the representative calculation in Figure 3.14 are such; 9.04 Mpa, 50.8 °C and 0.60 kg/min of pressure,

temperature, and mass flow rate, respectively. From Figure 3.14, the density and pressure of CO_2 decrease while the velocity increases along with nozzle length. It is found that the properties of CO_2 flow in the nozzle are non-linear that can be physically explained by Mach number of CO_2 flow in the nozzle.

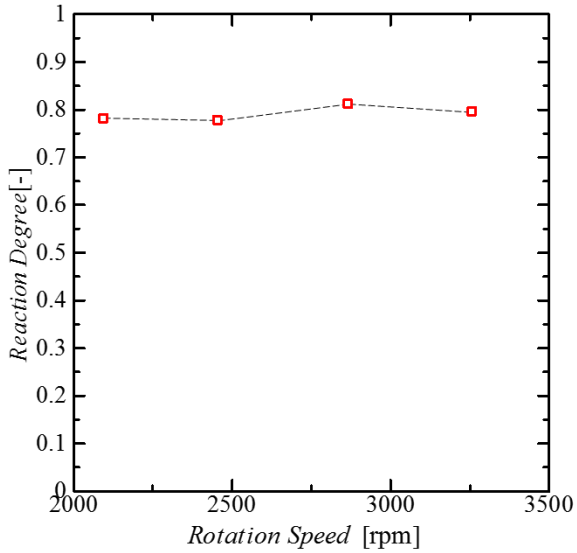

Figure 3.15. Reaction degree.

The performance of the turbine to generate power is depended on the design and type of turbine impeller which can be classified into impulse-type and reaction-type. For an impulse turbine, only kinetic energy is used to generate energy. While, reaction turbine, both pressure, and kinetic energy are used. The types of the turbine can be considered by the degree of reaction, from the equation below;

$$N_{reaction} = \frac{\left(U_2^2 - U_1^2\right) + \left(W_1^2 - W_2^2\right)}{\left(U_2^2 - U_1^2\right) + \left(C_2^2 - C_1^2\right) + \left(W_1^2 - W_2^2\right)} \times 100 \tag{3.18}$$

by the degree of reaction $N_{reaction}$ %, the absolute velocity C m/s, the relative velocity of fluid W m/s and speed of turbine impeller U m/s. When determined the degree of reaction, the pressure becomes more influence when higher than 50 % of the degree of reaction. On the other hand, as the degree of reaction is less than 50 %, the effect of momentum increase.

As shown in Figure 3.15, the result of the degree of reaction is more significant than 80% in all operation condition. Which means the reaction type of turbine is used to process in this study [16]. The result that the rotational force of the impeller has a large proportion of the pressure compared with momentum.

In examining turbine performance (output test), finally, the total energy E which affects the rotation of rotor vane at the exit of a nozzle can be estimated by following equation [17],

$$E = \frac{1}{2}u^2 + \left(\frac{k}{k-1}\right)\frac{P}{\rho} \tag{3.19}$$

where u is the initial velocity.

By calculating equation (3.19), the sum of the velocity head and pressure head can be obtained and displayed together with experimental verification in Figure 3.16. In particular, the velocity head

and pressure head with nozzle length at 25 mm, 29 mm and 33 mm are displayed in Figure 3.16. For the change of head differences for the nozzles of 25 mm to 29 mm and to 33 mm, both of pressure head and density head shows a small increasing trend. It is shown, by comparison with the experimental data and analytical verification in Figure 3.16, that both results show good qualitative agreement.

It is mentioned that, although the qualitative agreement for the comparison (between the analytical and experimental) is reached, these are apparent quantitative disagreements between the two. Though the numerical choice (for the nozzle length of 25 mm, 29 mm and 33 mm) gives reasonably good estimates; internal flow phenomena must be more completed rather than conventional treatment of the gas-dynamics (it was merely given by equations (3.7) and (3.8)). However, it is out-scope of the present work. For more detailed and advanced treatment of the numerical work, the points mentioned above should be cleared in the further studies.

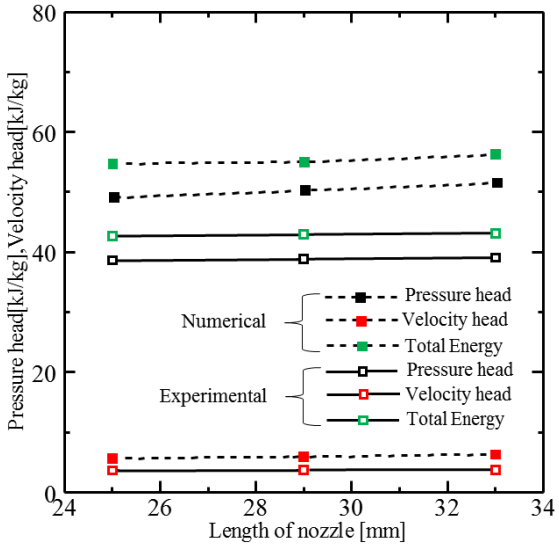

Figure 3.16. Experimental result in comparison with the numerical result for head differences for three nozzles (d_n = 1.0 mm).

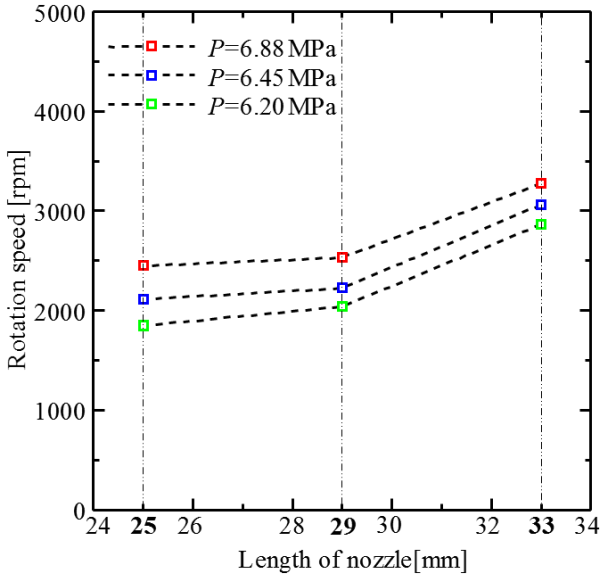

Figure 3.17. Experimental results of the rotational speed of turbine for nozzles of 25, 29 and 33 mm (d_n = 1.0 mm).

In Figure 3.17, the experimental result of rotational speeds of the turbine are displayed in three representative pressure conditions, which are verified by equation (3.19) and determined by the analytical results displayed in Figure 3.16 for characteristic nozzle length at 25 mm, 29 mm and 33 mm. As seen in Figure 3.17, substantial increases in the rotational speed of the turbine by increasing nozzles of rotational speed for the turbine are evident for the given pressures. The increase rates (for each given pressure) are almost the same. It is thought that within the geometric limitation of nozzle length installing to the impulse turbine, the nozzle length of 33 mm (with the maximum nozzle diameter of d_n = 1.0 mm) gives the best geometric configuration for the current turbine performance design.

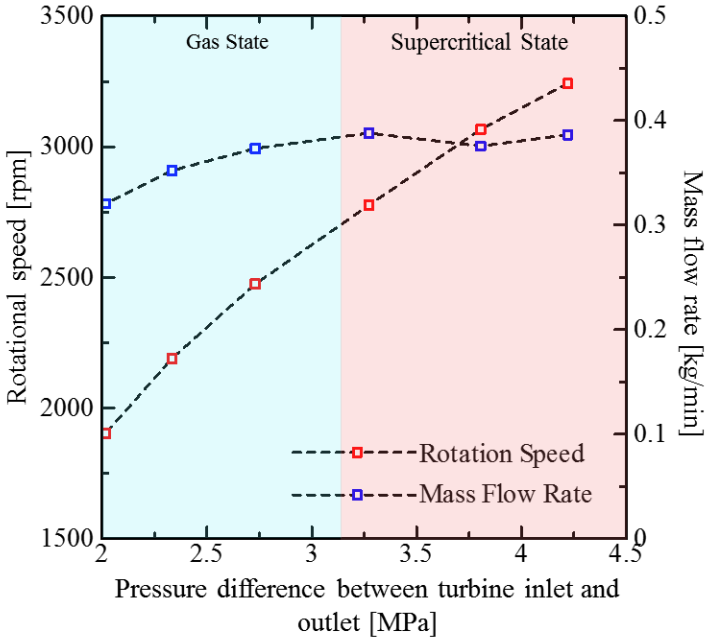

Figure 3.18. Experimental results of the rotation speed and mass flow rate of CO_2 (Difference gas and supercritical state) [16].

In order to further investigate the effect of fluid due to the different phase of the inlet, the experiment on turbine based on the condition of 0.7 mm inner diameter and 29 mm nozzle length has been carried out. The performance of supercritical CO_2 solar Rankine cycle system depends on solar radiation and weather condition. Because of that, the phase of CO_2 at the turbine inlet is various depend on temperature, pressure, and mass flow rate. The change of rotational speed and mass flow rate due to the phase change of CO_2 from a gas state to a supercritical state with the pressure difference of the turbine inlet and outlet is shown in Figure 3.18. The rotational speed of the turbine shows an improvement tendency with the rise of the pressure difference, and the mass flow rate also rises with the transition to the supercritical state.

The change in pressure due to the difference in phase state from the nozzle inlet to the nozzle outlet is shown in Figure 3.19, one-dimensional compressible flow analysis calculates the pressure. From the nozzle inlet to outlet, the pressure difference is found as small in both of gas state or supercritical state. For this reason, it can be concluded that the condition of CO_2 does not affect the rotational speed of the turbine.

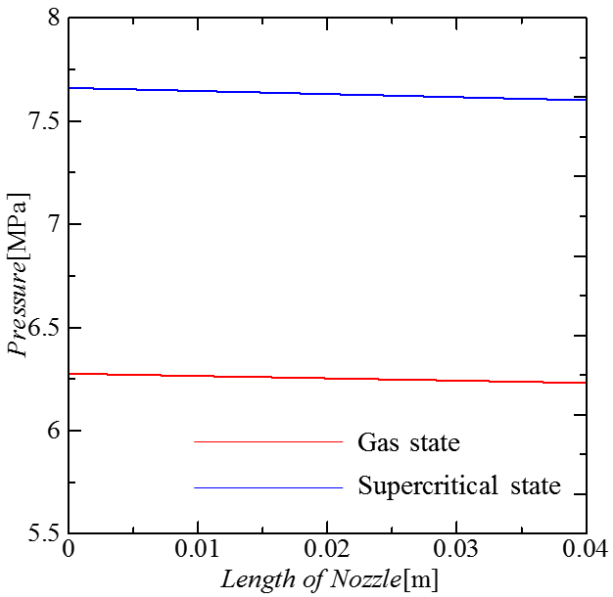

Figure 3.19. The calculation result of a change in pressure with difference inlet state, 6.63 MPa for gas state and 7.66 MPa for the supercritical state at nozzle diameter 0.7 mm [16].

Further study is necessary for obtaining higher performance turbine, as the supercritical CO_2 fluid flow exhibits the loss inside the turbine, it should be considered to include friction loss, vortex loss, impact loss and leak loss together with two (or three) dimensional gas-dynamics treatment in the nozzle.

3.2.3 Construction of novel thermally driven pump

In the early development of supercritical CO_2 solar Rankine cycle system, as described, the mechanical feed pump was preliminarily installed, which required relatively sizeable electric energy with the mechanical loss, resultantly making the overall efficiency of the system to decrease. Due to these problems, there remains a long-term need for developing a way of pressurizing and transferring working fluid with minimum power consumption and with no mechanical loss and better reliability. A novel thermally driven pump is considered as a solution with advantages of zero power consumption and high reliability compared with the conventional mechanical feed pump [5,9].

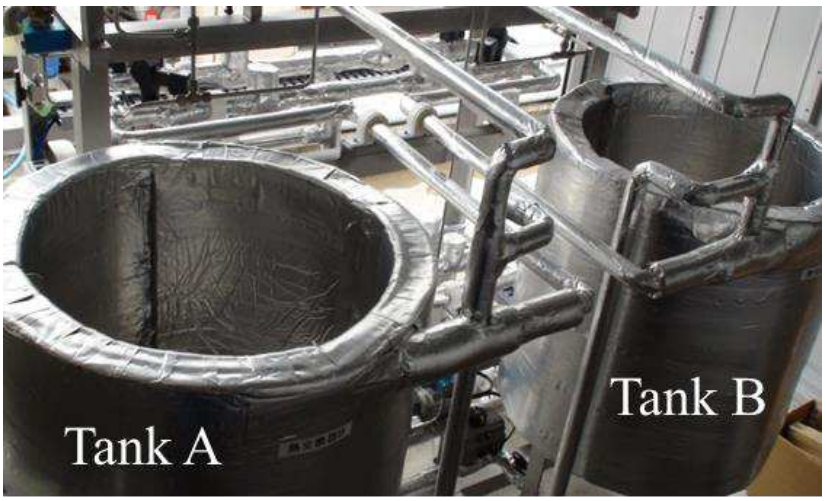

Figure 3.20. The outlook of thermally driven pump composed of Tank A and Tank B.

In the progress of the current system, the mechanical feed pump is replaced by a thermally driven pump. The thermally driven pump in supercritical CO_2 solar Rankine cycle system consists of

two expansion tanks as the outlook of the test device is shown in Figure 3.20. In each tank, the CO_2 tube is made of stainless steel SUS304 to enduring a high working pressure with 23.6 m of total length. The tube is structured as a double tube; the water tube covers the CO_2 tube to cooling/heating CO_2 (Figure 3.21). The diameter of CO_2 and water tube are 12.7 mm and 25.4 mm, respectively. The maximum value of CO_2 in each tank can be estimated as 5.8 ℓ.

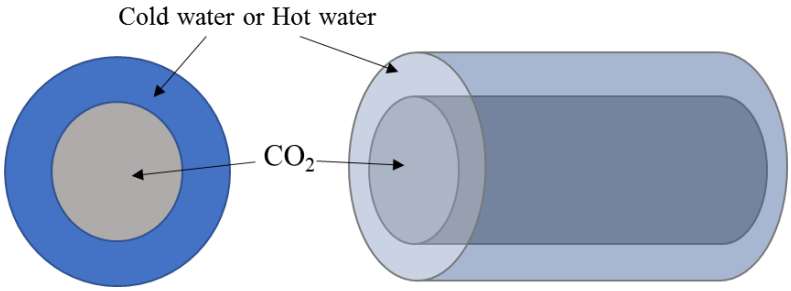

Figure 3.21. Section view of CO_2 inside the thermally driven pump.

The thermally driven pump is a working fluid (liquid state CO_2)-circulating pump with spiral tube structure, as the schematic of the test device is shown in Figure 3.22, which consists of two expansion tanks ① with heating/cooling apparatus in each tank ②, a CO_2 inlet path ③, a CO_2 discharge path ④, open/close valves ⑤ and pressure-regulating valve ⑥. Also, a check valve ⑦ is installed in the CO_2 inlet path to prevent reverse flow. The expansion tanks are manufactured as high-pressure vessels, working at room temperature with a maximum pressure of 12 MPa.

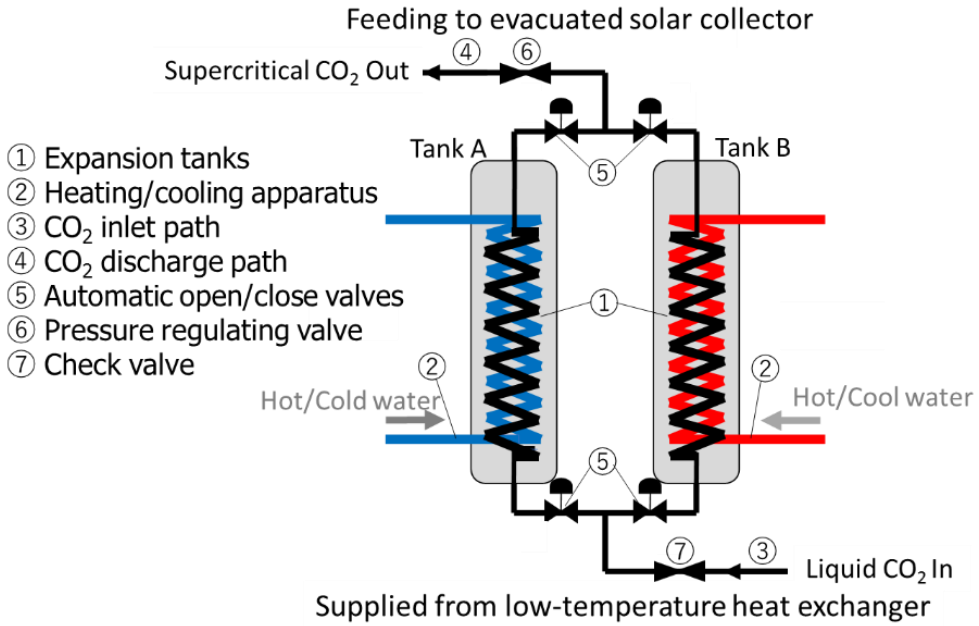

Figure 3.22. Schematic of novel-concept thermally driven pump in the test set-up.

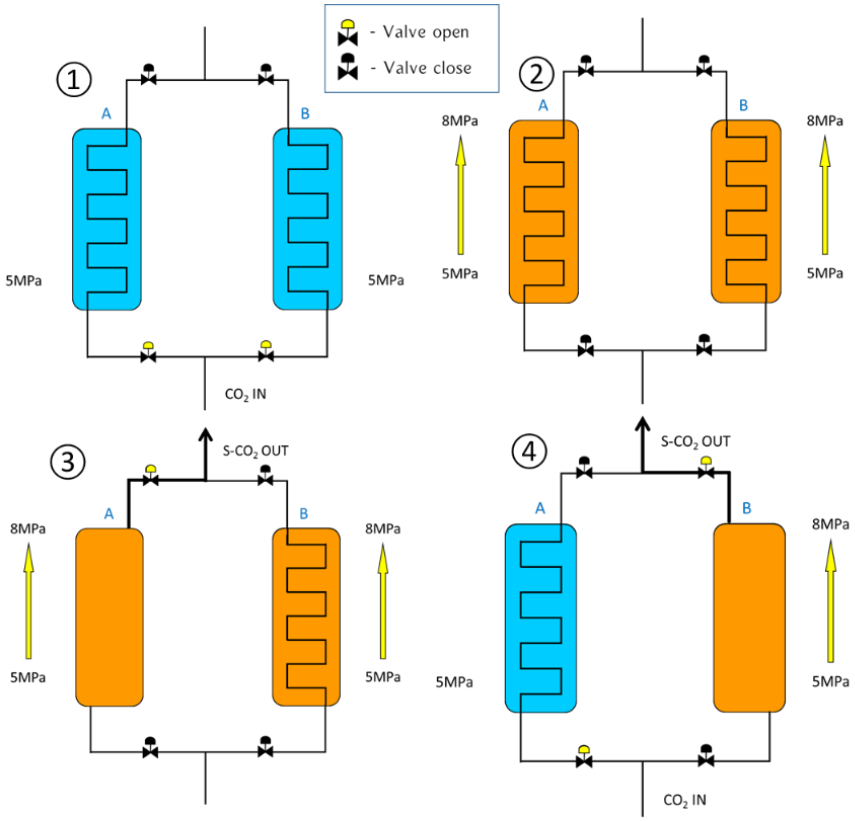

Figure 3.23. Schematic of the thermally driving pump working principle.

As shown in Figure 3.22, the thermally driven pump is a refrigerant (liquid CO_2)-circulation pump, which is composed of two expansion tanks. The substantial pressure difference between the thermally driven pump and outside of the pump (evacuated solar collector and low-temperature heat exchanger) are generated by using hot and cold water (secondary circulation fluid) for heating and cooling CO_2 inside the tank. The pressure difference drives CO_2 without any mechanical movement and electric power required. Because of the superiority, a prototype thermally driven pump was newly installed and tested to be utilized in the actual Rankine cycle instead of the mechanical feed pump. The working principle of the thermally driven pump are described below (referring ① - ④ operation process as displayed in Figure 3.23;

①: When lower valves are opened, low-pressure CO_2 (5 MPa) flows from heat exchanger by the pressure difference.

②: When lower valves are closed, hot water is heated CO_2 to high pressure (5 MPa to 8 MPa), CO_2 turns into a supercritical state.

③: When the upper valve tank A is opened, supercritical CO_2 (8 MPa) flows to evacuated solar collector by the pressure difference. Then cold water is used to cool down tank A (where the pressure is reduced to lower than 5 MPa).

④: When the upper valve of tank B is opened to let supercritical CO_2 flow, the lower valve of tank A is opened to let low-pressure CO_2 (5 MPa) flow in the tank. Moreover, cycle recommences.

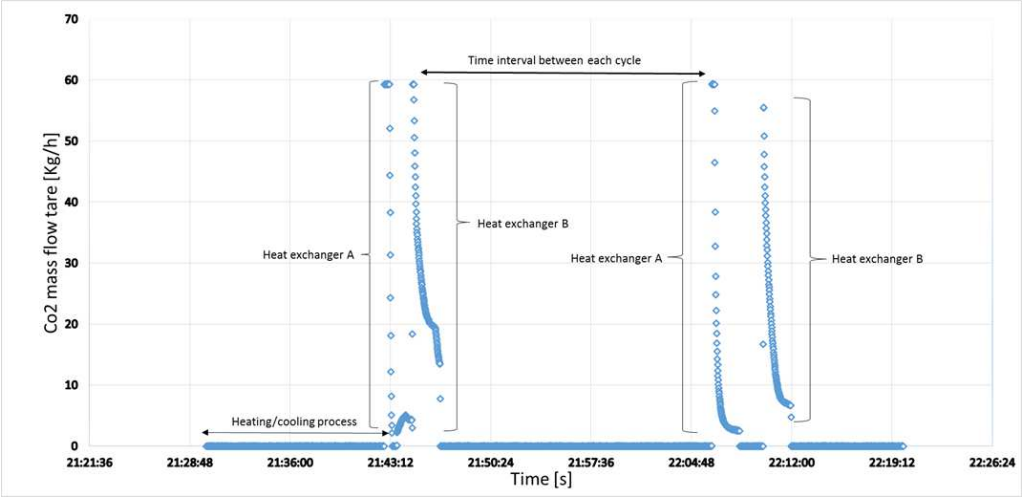

Figure 3.24. CO_2 mass flow rate in the thermally driven pump.

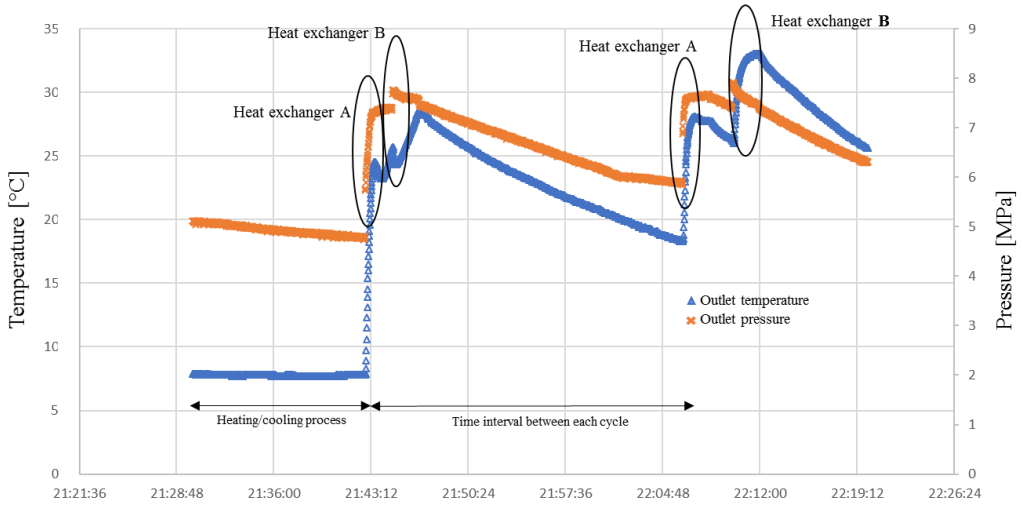

Figure 3.25. Pressure and temperature of outlet CO_2 in the thermally driven pump.

The experimental results were obtained, and representative data are displayed for the outlet flow from the thermally driven pump as it was installed in the CO_2 supercritical Rankine cycle for a trial test. The resultant mass flow rate and pressure and temperature at the exit point of the thermally driven pump are shown in Figure 3.24 and 3.25, respectively [18]. In Figure 3.24, the outlet flow (mass flow rate) of CO_2 can be found as high as 60 kg/h at the peak point. However, as observed the peak point is occurred in an only short period, due to the nature of the function of the thermally driven pump (batch processing) and the interval time between each peak is found to be quite long due to the nature of the operation. Due to these reasons, the CO_2 outlet flow from the thermally driven pump is not continuous. The pressure and temperature of CO_2 at the exit point of the thermally driven pump from the same experimental are also plotted in Figure 3.25. It is found that, at the peak points, both temperature and pressure are achieved to be in the supercritical region. These feeding mechanism (as shown in Figure 3.24 and Figure 3.25) improves the performance of SRCS because CO_2 turns to be a supercritical state before entering the evacuated solar collector. This phenomenon can be confirmed by the *P-h* (Mollier) diagram of SRCS with the thermally driven pump as indicated in Figure 3.26 [9], the large enthalpy (Δh) occurs between state ③ to ④. In which CO_2 is directly turned into the supercritical state from the low-pressure state without passing to the high-pressure state, which does not occur in ordinary SRCS operation process (Figure 3.2 (b)).

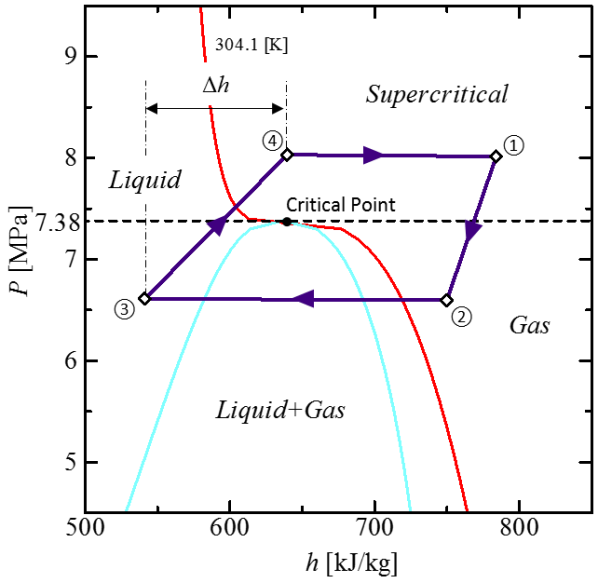

Figure 3.26. Characteristic *P-h* diagram of SRCS with the thermally driven pump.

From mentioned above that the non-continues flow of CO_2 with the thermally driven pump was found due to the lagging time of cooling and heating process. Hot water temperature in the heating process is considered as a significant factor to shorten the time of the heating process.

To deal with the problem in the non-continuous flow of CO_2 with thermally driven pump, which is directly related to the performance of the system itself, the simple one-dimension quasi-flow model is considered to investigate the flow of the heat exchanging process in the thermally driven pump. The basic design of a thermally driven pump dependent on designing a spiral flow pathway, where unique properties of the supercritical CO_2 flow passes. By the working principle, the high enthalpy Δh with associated mass flow rate enhances the performance of the pumping process of the pump. The flow of CO_2 is assumed to be laminar flow, and the following manner can approximate the mass flow rate (by the thermally driven pump).

The energy conservation equation, which relates moving fluid's pressure P, density ρ, velocity v, height y, and also enthalpy h and friction loss f in the fluid flow in the tube, can be written by the one-dimensional energy equation from inside the thermally driven pump (Point 1 in Figure 3.27) to outlet of the thermally driven pump (Point 2 in Figure 3.27) as

$$P_1 + \frac{1}{2}\rho_1 v_1^2 + \rho_1 g y_1 + h_1 = P_2 + \frac{1}{2}\rho_2 v_2^2 + \rho_2 g y_2 + h_2 + f \tag{3.20}$$

From the process of the thermally driven pump, stagnant flow (at Point 1) having zero velocity existing ($v_1 = 0$) at to the valve opening, while fluid passing outlet point of pipe (at Point 2) has velocity as v_2. The equation (3.21) becomes as

$$\frac{1}{2}\rho_2 v_2^2 = \Delta P + \Delta h - \rho_2 g y_2 - f \tag{3.21}$$

where the friction loss f can be combined with the friction loss in the swirling flow [19] and the loss due to change in mass of the two-phase flow regime [20].

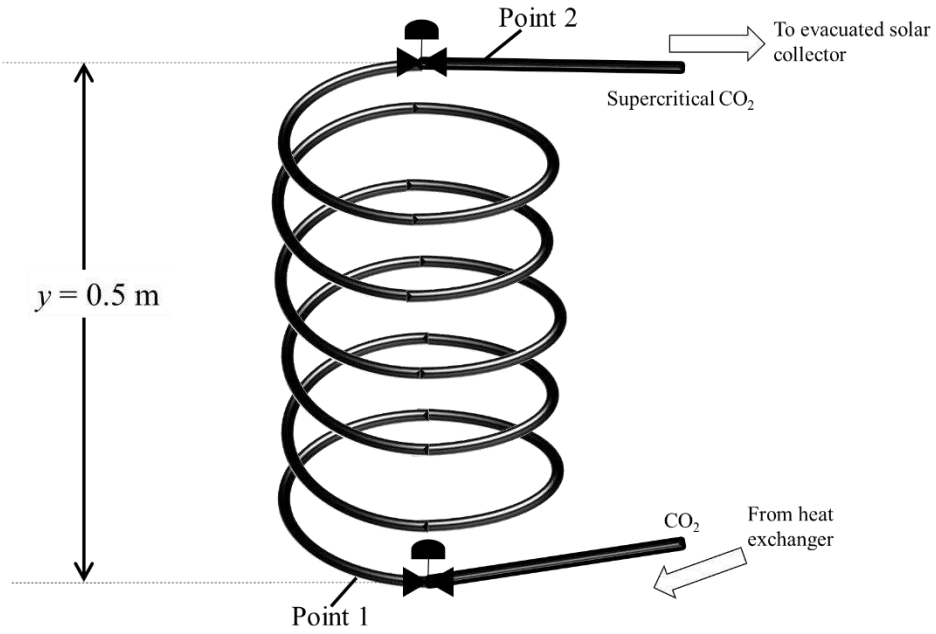

Figure 3.27. Quasi-static flow model of the thermally driven pump.

The result obtained from the analytical estimation (equation (3.21)) gives CO_2 mass flow rate as approximately 30% (at a maximum flow rate) lower from the experimental result, i.e. 46.8 kg/h and 60 kg/h (shown in Figure 3.24), respectively. This is due to the fact that the energy conservation equation is still not sufficient (only first order energy balance equation) to estimate more accurate supercritical CO_2 mass flow rate in the thermally driven pump. It must be further commented from the primary analysis, that the key parameters of CO_2 outlet flow from the thermally driven pump are the pressure difference ΔP and the enthalpy difference (the high enthalpy Δh) between inside the pump (Point 1) and outlet of the pump (Point 2). The parameters ΔP and Δh have significant influence on the CO_2 mass flow rate of the thermally driven pump, as approximately 90 % in total. On the other hand, the parameters such as height and friction loss have a very small influence on the CO_2 mass flow rate. In future analysis, the parameters for accurate estimation of pressure P and enthalpy h have to be considered as the priority to develop further advanced thermally driven pump.

To achieve the aim of replacing mechanical feed pump with thermally driven pump, it is to be expected that the efficiency of the cycle using thermally driven pump would be higher than using mechanical feed pump because there should not be any mechanical loss occurred in the pumping process. To confirm, the objective system efficiency of the total Rankine system, by either using mechanical feed pump and using thermally driven pump, were compared based on two conditions; the ideal condition, where the efficiency of the mechanical feed pump (η_P) was set at 100 % and practical condition, where efficiency of the mechanical feed pump (η_P) was set at 50 % [5]. In the initial state of development, power for pumping and heating water in the thermally driven pump are ignored. The efficiencies are calculated as

$$\eta_{thf} = \frac{(h_1 - h_2) - (h_5 - h_4)/\eta_P}{h_1 - h_4} \tag{3.22}$$

$$\eta_{tht} = \frac{(h_1 - h_2)}{h_1 - h_4} \tag{3.23}$$

where h is specific enthalpy on each position of process in the system (in Figure 3.2 (b)), h_1 - h_2, h_4 - h_3, h_1 - h_3 and h_1 - h_4 are the energy (enthalpy) drop through the turbine, and net energy (enthalpy) gain by the system with the thermally driven pump and mechanical feed pump, respectively.

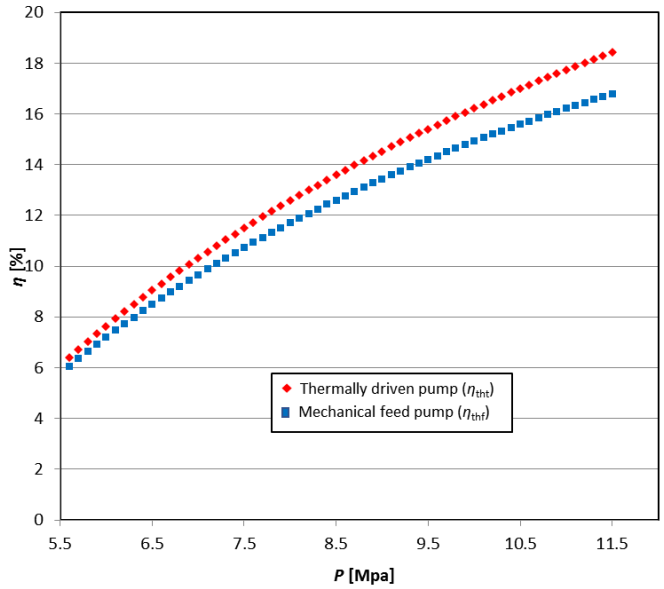

Figure 3.28. Comparisons of the system efficiencies of the loop system with thermally driven pump and mechanical feed pump in ideal condition.

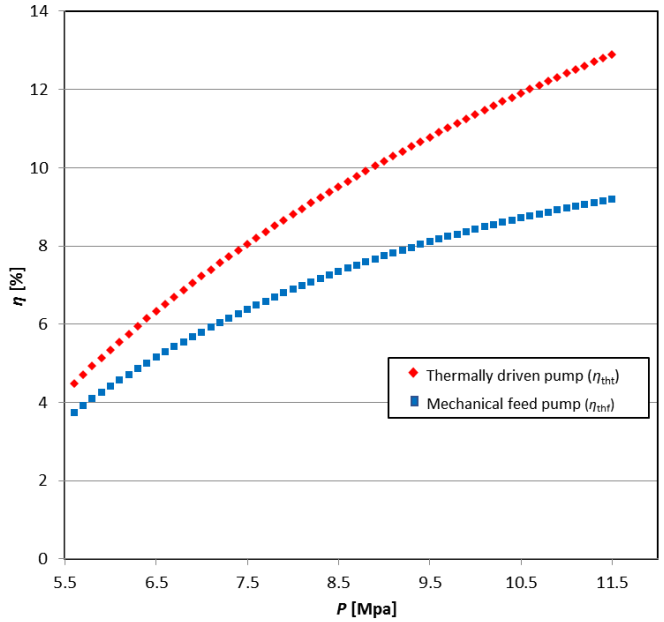

Figure 3.29. Comparisons of the system efficiencies of the loop system with thermally driven pump and mechanical feed pump in practical condition.

It can be seen the experimental results shown in Figure 3.28 and Figure 3.29 [4], which show the comparison of the system efficiencies of the loop cycle system while using thermally driven pump and mechanical feed pump in the driven part with different pressure at the outlet of evacuated tube solar collector (P_1) in the ideal and practical conditions, respectively. The outlet temperature of evacuated tube solar collector and heat exchanger are set at 200 °C and 5 °C, respectively, assuming the system under the given conditions in equations (3.22) and (3.23) as mentioned above. As shown in Figure 3.28 and Figure 3.29, they are observed that the system efficiency of the supercritical CO_2 solar Rankine

cycle system while using thermally driven is higher than using mechanical feed pump in the driven part. In the practical condition, the enhancement of the system efficiency of the loop system with using the thermally driven pump is approximately 3.5% higher compared with using the mechanical feed pump at outlet pressure from evacuated tube solar collector is at 11 MPa.

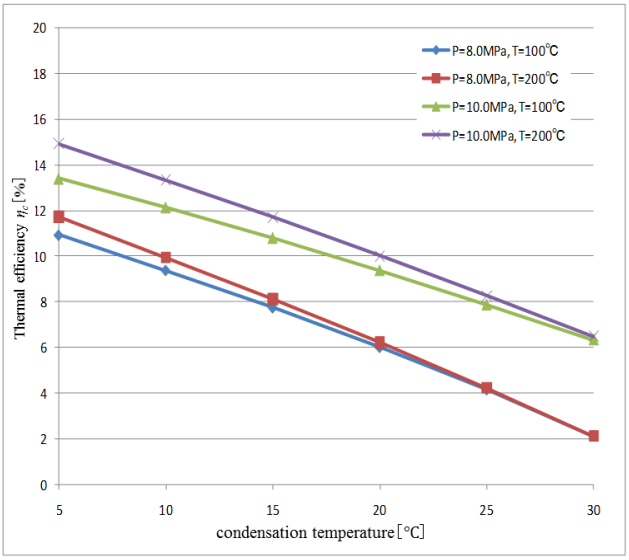

Figure 3.30. Thermal efficiencies of the system using a mechanical feed pump.

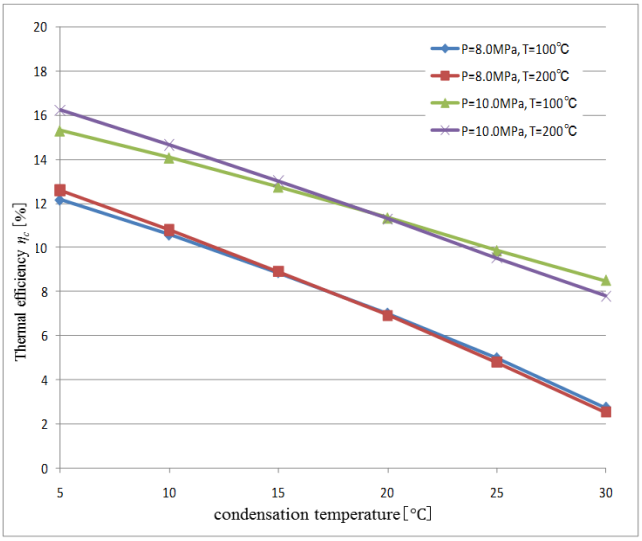

Figure 3.31. Thermal efficiencies of the system using the thermally driven pump.

The thermal efficiencies of supercritical CO_2 Rankine cycle system with mechanical feed pump and thermally driven pump in the ideal condition varying with the outlet temperature of solar collector unit at two different pressures P = 8.0 and 10.0 MPa and two temperatures T = 100 °C and 200 °C are estimated with outlet temperature of heat exchanger (condensation temperature). The results of estimates are shown in Figure 3.30 for the mechanical feed pump and Figure 3.31 for the thermally driven pump [18]. It can be confirmed that the system thermal efficiency of the supercritical CO_2 solar Rankine cycle system increases with pressure. However, the effect of the outlet temperature of the evacuated solar collector on the system thermal is small, as observed in Figure 3.30 and Figure 3.31. The outlet temperature from the heat exchanger has a significant effect on the system thermal efficiency. With temperature increasing, the system thermal efficiency decreases. Compared the efficiency of the mechanical feed pump and thermally driven pump from Figure 3.30 and Figure 3.31, supercritical CO_2

Rankine cycle system with the thermally driven pump has higher thermal efficiency than using mechanical feed pump in all operating condition. The highest thermal efficiency was with the condition of 10.0 MPa and 200 °C of pressure and temperature, respectively.

3.3 Conclusions

The supercritical CO_2 solar Rankine cycle system is proposed to contribute to giving a new solution to the global warming crisis. The system is a combination of the most significant renewable energy source and accessible to use, the solar energy, and 'truly natural' working fluid, CO_2, for producing a combined generation of electric power and heat output.

Based on the proposed cycle, the supercritical CO_2 solar Rankine cycle system has been designed, constructed and tested. The system works well with the transcritical cycle throughout the test hours, giving promising results for achieving electric power generation and heat output with a reasonable thermodynamic efficiency, and also give a clue for improvement of the local environmental issue which might be valued.

In the typical working condition of CO_2, the energy conversion performance is too low to be used as a working fluid in the power cycle compared with other working fluid. However, where CO_2 is operated in the supercritical region, the rate of heat transfer is found much higher, and resultantly the system would be able to achieve high-performance characteristics. This is the primary motivation for developing the supercritical CO_2 solar Rankine cycle system which can achieve the excellent system performance, adapting unique properties of supercritical CO_2.

In the development of components in SRCS to date, it is summarized as

- Evacuated solar collector: the performance can be improved by the flow passage arrangement and a flow condition of supercritical CO_2. The heat transfer is enhanced with the unique properties of supercritical CO_2.
- Turbine: newly designed specific turbine for supercritical state CO_2 was introduced in the developing system of SRCS for gaining good performance in electric power generation, avoiding the choked flow in the test nozzle to prevent the decrease in efficiency of the turbine.
- Thermally driven pump: mechanical feed pump is replaced by the thermally driven pump for avoiding the mechanical loss and electric power requirement in the feeding operation. SRCS with thermally driven pump gives higher thermal efficiency than ordinary SRCS with mechanical feed pump. However, the outlet flow of the thermally driven pump is not continuous. For further improvement of the device, the critical operating parameters are the pressure difference and the enthalpy difference to shorter the discontinuous time interval.

The supercritical CO_2 solar Rankine cycle system is developed to generate electric and heat energy in the environmentally friendly manner by combining the solar energy and natural working fluid CO_2. The system can be regarded as one of the solutions for tackling global warming and climate change issue.

References

[1] Koytsoumpa, E.I., Bergins, C. and Kakaras, E., 2017. The CO_2 economy: Review of CO_2 capture and reuse technologies. *The Journal of Supercritical Fluids*.

[2] Dincer, I., 2000. Renewable energy and sustainable development: a crucial review. *Renewable and sustainable energy reviews*, *4*(2), pp.157-175.

[3] Zhang, X.R., Yamaguchi, H., Fujima, K., Enomoto, M. and Sawada, N., 2005. A feasibility study of CO_2-based Rankine cycle powered by solar energy. *JSME International Journal Series B Fluids and Thermal Engineering*, *48*(3), pp.540-547.

[4] Zhang, X.R., Yamaguchi, H., Uneno, D., Fujima, K., Enomoto, M. and Sawada, N., 2006. Analysis of a novel solar energy-powered Rankine cycle for combined power and heat generation using supercritical carbon dioxide. *Renewable Energy*, *31*(12), pp.1839-1854.

[5] Kuwahara, T., Niu, X.D., Yamaguchi, H., Iwamoto, Y. and Zhang, X.R., 2011. Performance study of supercritical CO_2-based solar Rankine cycle system with a novel-concept thermally driven pump. *Proceedings of the Institution of Mechanical Engineers, Part A: Journal of Power and Energy*, *225*(4), pp.413-419.

[6] PROPATH Group, 1997. PROPATH: a program package for thermophysical properties.

[7] Zhang, X.R., Yamaguchi, H. and Uneno, D., 2007. Thermodynamic analysis of the CO_2-based Rankine cycle powered by solar energy. *International Journal of Energy Research*, *31*(14), pp.1414-1424.

[8] Pumaneratkul, C., Iwamoto, Y. and Yamaguchi, H., 2015. Nozzle test in supercritical CO_2 turbine in Rankine cycle system. *Int J Adv Sci Technol*, pp.167-174.

[9] Yamaguchi, H., Zhang, X.R., Niu, X.D. and Hashitani, N., 2013. A novel thermally driven pump and its test in a supercritical CO_2 loop system. *International Journal of Energy Research*, *37*(11), pp.1331-1338.

[10] Niu, X.D., Yamaguchi, H., Iwamoto, Y. and Zhang, X.R., 2013. Optimal arrangement of the solar collectors of a supercritical CO_2-based solar Rankine cycle system. *Applied Thermal Engineering*, *50*(1), pp.505-510.

[11] Miller, R.W., 1983. *Flow measurement engineering handbook*, United States.

[12] Chen, M.F., Yamaguchi, H., Zhang, X.W. and Niu, X.D., 2015. Performance analyses of a particularly designed turbine for a supercritical CO_2-based solar Rankine cycle system. *International Journal of Energy Research*, *39*(13), pp.1819-1827.

[13] Yamaguchi, H., 2008. *Engineering fluid mechanics* (Vol. 85). Springer Science & Business Media.

[14] Parlange, J.Y., Braddock, R.D. and Sander, G., 1981. Analytical approximations to the solution of the Blasius equation. *Acta Mechanica*, *38*(1-2), pp.119-125.

[15] Nikuradse, J., 1950. *Laws of flow in rough pipes*. Washington: National Advisory Committee for Aeronautics.

[16] Yamaguchi, H., 2017. Supercritical Carbon Dioxide and Its Application to Rankine Cycle. In *Advanced Applications of Supercritical Fluids in Energy Systems* (pp. 335-368). IGI Global.

[17] Munson, B.R., Okiishi, T.H., Rothmayer, A.P. and Huebsch, W.W., 2014. *Fundamentals of fluid mechanics*. John Wiley & Sons.

[18] Pumaneratkul, C., Iwamoto, Y., Niu, X. D., Kuwahara, T. and Yamaguchi, H., 2015. Characteristics of thermally driven pump in supercritical CO_2 solar Rankine cycle system. *International Journal of Mechanical and Production Engineering*, *3*(4), pp. 1-6.

[19] White, C. M., 1932. Friction Factor and Its Relation to Heat Transfer. *Transactions of the Institution of Chemical Engineers*, *18*, pp. 66–86.

[20] Kakaç, S. and Ishil, M. eds., 2012. *Advances in two-phase flow and heat transfer: fundamentals and applications* (Vol. 64). Springer Science & Business Media.

Chapter 4

Exergy analysis of development on supercritical CO_2 solar Rankine cycle system

The study on the efficiencies of energy conversion system is carried out for the sake of the improvement of efficiencies. The analysis of the conventional thermodynamics can be described by the first law of thermodynamics, also known as energy analysis. For the engineering system, efficiency can generally be defined as the ratio of demand input to supply output. The exergy analysis, based on the second law of thermodynamics is used to improve the efficiency of the system by energy-resource use (for the quantities of the location, types, and magnitudes of wastes and losses) [1]. Exergy efficiency is the measure of how nearly the efficiency of a process approaches the ideal condition. On the contrary, the exergy analysis points out the specific weakness of the system to design a higher efficient system by reducing inefficiencies. For these reasons, the exergy analysis gives the meaningful method over energy analysis in term of efficiency evaluation [2~3].

In this chapter, the energy analysis and exergy analysis will be described in detail. Further the exergy analysis of supercritical CO_2 solar Rankine cycle system by using either conventional mechanical feed pump or newly developed thermally driven pump are investigated in a realistic operating condition (field test), and the results are verified to confirm the advantage and superior property of the thermally driven pump against the mechanical feed pump, in which exergy analysis is based on the combination of the first and the second laws of thermodynamics, also able to verify the losses of quality, or work potential in the system.

4.1 Energy Analysis

4.1.1 Energy balance

Energy is considered as the capacity for doing work. In the system, there are three various forms that energy can be stored [4]. The kinetic energy and the potential energy are macroscopic forms. While the internal energy consists of thermal (sensible and latent) energy, chemical energy and nuclear energy. The internal energy, kinetic energy, and potential energy balance, respectively, are

$$\Delta U = m\left(u_2 - u_1\right) \tag{4.1}$$

$$\Delta \mathrm{KE} = \frac{1}{2} m\left(V_2^2 - V_1^2\right) \tag{4.2}$$

$$\Delta \mathrm{PE} = \frac{1}{2} mg\left(z_2 - z_1\right) \tag{4.3}$$

where m is mass, u is specific internal energy, V is velocity, g is gravitational acceleration and z is elevation.

The total energy balance E of the system is the sum of its internal U, kinetic KE and potential PE energies, which can be expressed in equation (4.4) as

$$\Delta E = E_2 - E_1 = \Delta U + \Delta \mathrm{KE} + \Delta \mathrm{PE} \tag{4.4}$$

Usually, the kinetic energy and potential energy do not change in the process of energy balance. This is because of the change in the internal energy, which is shown as

$$\Delta E = \Delta U = m\left(u_2 - u_1\right) \tag{4.5}$$

For the energy per unit of time t or the rate of energy, it can be written as

$$\dot{E} = \frac{E}{\Delta t} \tag{4.6}$$

4.1.2 The First Law of Thermodynamics

The first law of thermodynamics shows the associations of various form in energy and energy interactions. The first law of thermodynamics, the conservation of energy principle can be observed in the experiment that the energy changes the forms during the process, neither create nor destroy [5]. Moreover, the first law of thermodynamics can be expressed for a general system in as much as the net change in the total energy of a system during a process, which equals to the difference between the total input energy entering and the total output energy of the system. It is shown as:

$$E_{\text{in}} - E_{\text{out}} = \Delta E_{\text{system}} \tag{4.7}$$

or

$$\dot{E}_{\text{in}} - \dot{E}_{\text{out}} = \frac{dE}{dt} \tag{4.8}$$

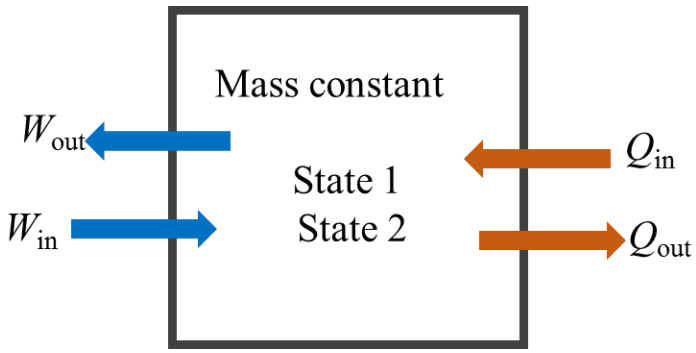

Figure 4.1. A conventional closed system with heat and work interactions.

Consider a closed system undergoing a process between a specified State 1 (initial) to another specified State 2 (final state) with heat Q and work W interactions with the surroundings shown in Figure 4.1; it can be rewritten from equation (4.7) as

$$\left(Q_{\text{in}} + W_{\text{in}}\right) - \left(Q_{\text{out}} + W_{\text{out}}\right) = \Delta U + \Delta\text{KE} + \Delta\text{PE} \tag{4.9}$$

If there is no change in kinetic and potential energies:

$$\left(Q_{\text{in}} + W_{\text{in}}\right) - \left(Q_{\text{out}} + W_{\text{out}}\right) = \Delta U = m\left(u_2 - u_1\right) \tag{4.10}$$

4.2 Exergy analysis

4.2.1. The Second law of thermodynamics

In the past decades of scientific research in energy conversion system, the concept of energy balance is only considered by the first law of thermodynamics, which deals with the quantity of energy. To more accurately energy conversion processes, the development of scientific thought has been replaced by the second law of thermodynamics, which asserts that energy has quality as well as quantity [6].

Energy can be considered as the conversed property that the process is unknown for taking place in violation of the first law of thermodynamics. It is observed that the energy process proceeds in a particular direction and not in the reverse direction. The first law of thermodynamics takes place with no restriction on the direction of a process, however, satisfying the first law of thermodynamics does not ensure that that the process will occur. This inadequacy of the first law of thermodynamics to identify whether a process can take place is remedied by introducing another general principle, the second law of thermodynamics.

The second law of thermodynamics is not only to identify the direction of the process but also confirms that energy has quality as well as quantity. The first law of thermodynamics is concerned with the quantity of energy and the transformations of energy from one form to another form without considering its quality. Preserving the quality of energy is of significant concern on the engineering viewpoint. The second law of thermodynamics gives the necessary means to determine the quality as well as the degree of degradation of energy during a process [7].

Furthermore, the second law of thermodynamics is also used to determine the theoretical limits for the performance of commonly used engineering systems such as heat engines and refrigerators, as well as predicting the degree of completion of chemical reactions. The second law of thermodynamics is also closely associated with the concept of perfection. In fact, the second law of thermodynamics can define perfection for thermodynamic processes. It can be used to quantify the level of perfection of a process and point out the direction to eliminate imperfections effectively.

The two classical statements of the second law of thermodynamics are as follows;

- **The Clausius statement** - The heat never inherently flows from the colder to the hotter reservoir without consuming some external work [8]:

"It is impossible to construct a device that operates in a cycle and produces no effect other than the transfer of heat from a lower temperature body to a higher temperature body."

- **The Kelvin-Planck statement -** It is not able to extract the heat from a system and convert total heat into work (or known as heat engine statement) [9]:

"It is impossible for any device that operates in a cycle to receive heat from a single reservoir and produce a net amount of work."

The system will receive heat from the hot reservoir and reject heat to the cold reservoir. For the heat engine operation, efficiency can be expressed as the ratio of total work done by the engine to the heat supplied. If $Q_C = 0$, $\eta_{th} = 1 - \frac{Q_C}{Q_H} = 1$, however, the second law of thermodynamics states that heat engine is impossible to be 100 % efficient, $\eta_{th} < 1$.

Figure 4.2 and 4.3 represent to Clausius statement and Kelvin-Planck statement, respectively.

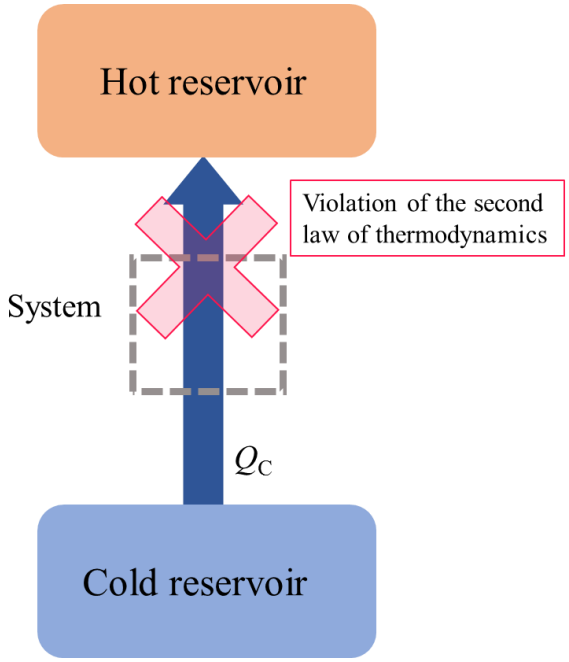

Figure 4.2. The Clausius statement of the second law of thermodynamics prohibits heat flows from cold to hot reservoir.

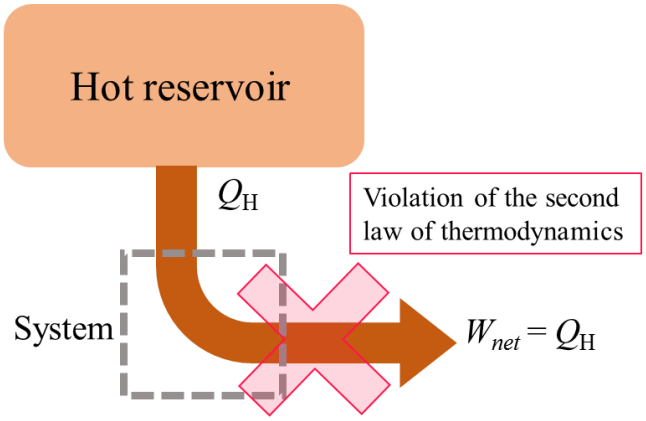

Figure 4.3. The Kelvin-Planck statement of the second law of thermodynamics remarks that heat is impossible to transfer into work entirely.

- **Equivalence of Clausius and Kelvin-Planck Statements:** It is remarkable that the two statements of the second law of thermodynamics are entirely equivalent. This equivalence can be substantiated by considering the violation of either statement results in a violation of another one. In Figure 4.4, two systems operate between the same hot and cold reservoirs. On the left system, Clausius violator pumps heat Q_C from the cold reservoir to the hot reservoir without external work, which is impossible. On the right system, the system takes Q_{H2} as heat input at the hot reservoir and converts a part into work W_{net} while heat Q_C is rejected to the cold reservoirs.

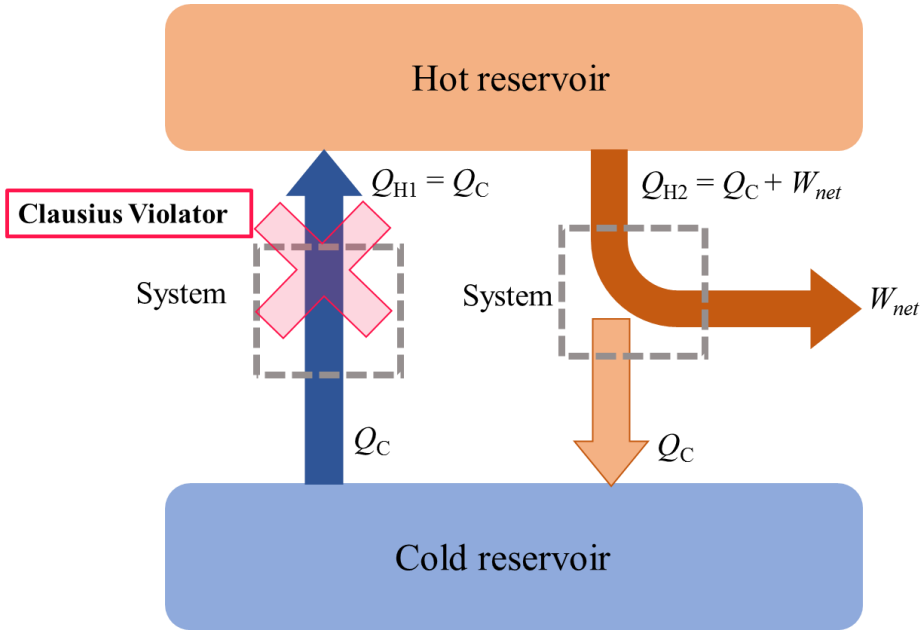

Figure 4.4. Equivalence of Clausius and Kelvin-Planck Statements with the Clausius violator.

The combination of two systems as shown in Figure 4.5 that work W_{net} produced from the right system is used as external work for the left system, and heat Q_C merely is pumped back from cold reservoir to hot reservoir. Thus, the continuous producing work with a single reservoir, which is Kelvin-Planck violator by extracting heat from a single reservoir and entirely converting to work. It is to say that if the system violates one statement, it also violates another statement and vice versa.

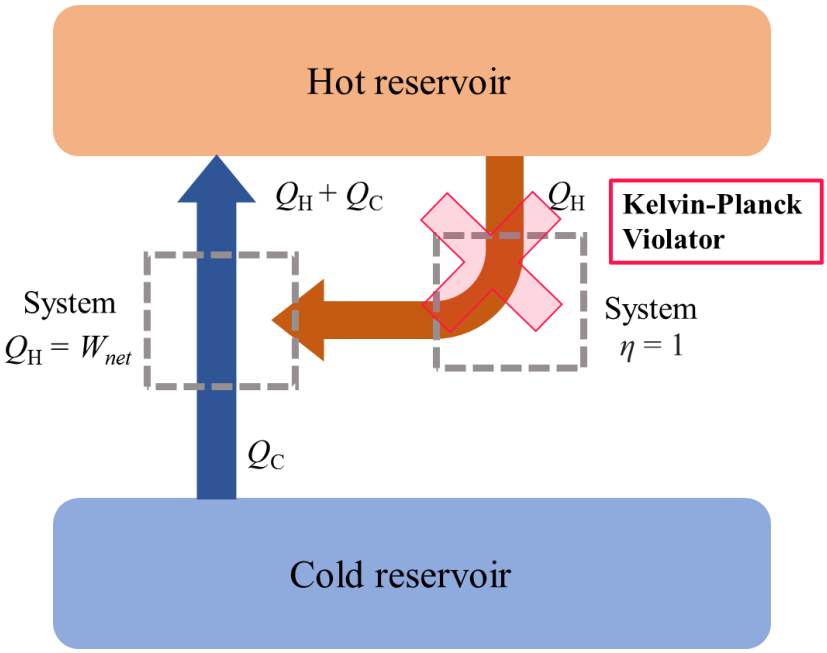

Figure 4.5. Equivalence of Clausius and Kelvin-Planck Statements with the Kelvin-Planck violator.

4.2.2 Entropy balance

In the second law of thermodynamics, it is stated that entropy can be created but cannot destroy. It means that the entropy change of the system during the process is higher compared with the entropy

transfer, in which the amount equals to the entropy generated S_g during the process in the system [10]. The entropy change ΔS is the sum of the entropy change between the system, and the environment can be expressed as

$$S_{in} - S_{out} + S_g = \Delta S \tag{4.11}$$

The relationship shown in equation (4.11) is referred to as the entropy balance and appropriate to the system through the process. Furthermore, it can be stated that the entropy change during the process within a system equals to the entropy generated in the system.

4.2.3 Exergy balance

Exergy of a thermodynamic system can be referred as the maximum amount of theoretical work that can be extracted from an overall system from its given state to the thermodynamic reference (dead) state with the environment, without intervention rather than its own and one of the environments [11]. The dead state is the state of that thermal and mechanical equilibrium is achieved at its both the temperature and pressure of the system is equal. Also, the kinetic and potential energies have no relation to the environment (zero velocity and zero elevation above a reference state) and no reaction to the environment (chemically inert) [12].

At a specific state of the system, exergy E can be expressed as

$$E = (U - U_0) + P_0(V - V_0) - T_0(S - S_0) + \mathrm{KE} + \mathrm{PE} \tag{4.12}$$

where U, V, S, KE, and PE imply to internal energy, volume, entropy, kinetic energy, and potential energy of the system at the specific state, respectively. While U_0, P_0, V_0, T_0, and S_0 donate internal energy, pressure, volume, temperature, and entropy of the system at the dead state, respectively.

From equation (4.12), it can be determined the exergy change between the two states, State 1 (initial state) and State 2 (finale state) as

$$E_2 - E_1 = (U_2 - U_1) + P_0(V_2 - V_1) - T_0(S_2 - S_1) + (\mathrm{KE}_2 - \mathrm{KE}_1) + (\mathrm{PE}_2 - \mathrm{PE}_1) \tag{4.13}$$

Similar to energy, exergy can be transferred across the boundary in a closed system. However, the exergy change in the system during the process is not necessary to equal with the net exergy transferred. It is because the exergy can be destroyed if the irreversibility process occurs in the system during the process. Figure 4.6 is schematics to understand the concept of exergy destruction in the second law of thermodynamics.

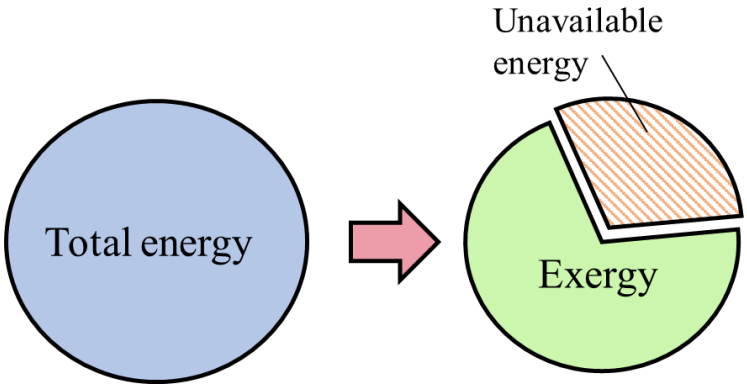

Figure 4.6. The irreversibility presents during the process.

The closed system exergy balance (from the initial state to final state) is given by

$$E_2 - E_1 = \int_1^2 \left(1 - \frac{T_0}{T_b}\right)\delta Q - \left[W - P_0\left(V_2 - V_1\right)\right] - T_0 \Delta S \tag{4.14}$$

in which exergy change E_2 - E_1 can be evaluated from equation (4.13).

From equation (4.14), it can be seen that the heat transfer is associated with the process. The term exergy transfer accompanying heat transfer E_q is

$$E_q = \int_1^2 \left(1 - \frac{T_0}{T_b}\right)\delta Q \tag{4.15}$$

where T_b is the temperature on the boundary during heat transfer process.

For the work, which is associated during the process, term of exergy transfer accompanying work E_w is

$$E_w = \left[W - P_0\left(V_2 - V_1\right)\right] \tag{4.16}$$

For the exergy destruction from the irreversibility in the system Π is

$$\Pi = T_0 \Delta S \tag{4.17}$$

with equations (4.15, 4.16 and 4.17), equation (4.14) can be alternative written as

$$E_2 - E_1 = E_q - E_w - \Pi \tag{4.18}$$

In the case of closed system exergy rate balance, the mass, energy and entropy balances, the convenient form can be expressed as [13]

$$\frac{dE}{dt} = \sum_j \left(1 - \frac{T_0}{T_j}\right)\dot{Q}_j - \left(\dot{W} - P_0 \frac{dV}{dt}\right) - \Pi \tag{4.19}$$

where dE/dt is the time rate change of exergy.

The exergy rate balance for control volumes at steady state, which is very useful for engineering analysis, can be modified from equation (4.19) that dE/dt and dV/dt equal to 0, the equation is written as

$$0 = \sum_j \left(1 - \frac{T_0}{T_j}\right)\dot{Q}_j - \dot{W} + \underline{\left(\sum_i \dot{m}_i e_i - \sum_e \dot{m}_e e_e\right)} - \Pi \tag{4.20}$$

where the underlined terms donate as the exergy transfer where mass is entering and exiting of the control volume. Term e_i and e_e are the exergy per unit of mass at entering and existing, respectively.

Term e is known as the specific flow exergy and expressed as

$$e = h - h_0 - T_0\left(s - s_0\right) + \frac{V^2}{2} + gz \tag{4.21}$$

In the same manner for the concept of energy balance, the kinetic energy, and potential energy can be neglected due to their minimal changes compared to enthalpy values during the process of exergy balance [14~15]. The equation can be rewritten as

$$e = h - h_0 - T_0\left(s - s_0\right) \tag{4.22}$$

alternatively, written as the change in exergy rate as

$$\dot{E} = \dot{m}\left[h - h_0 - T_0\left(s - s_0\right)\right] \tag{4.23}$$

where h and h_0 refer to specific entropy at the specific and dead state, respectively.

In the reversible processes of the system, all exergy is converted into work, however, in the practical, the irreversibility occurs in the process and total of work in the system is less than its exergy. The efficiency of the energy conversion system is equal to the ability to approach reversible operations [16]. The total exergy rate can describe the exergetic (second law) efficiency in the form output to input as

$$\eta_e = \frac{\text{Total exergy output}}{\text{Total exergy input}} = \frac{\dot{E}_{out}}{\dot{E}_{in}} \tag{4.24}$$

Figure 4.7 illustrates the energy, entropy, and exergy transfer from State 1 to State 2 where the temperature T_1 reduces to T_2, while the surrounding temperature is at T_0. Following the first law of thermodynamics, the transferred heat remains constant in quantity. In accordance with the second law of thermodynamics, the entropy and exergy transfer through the state of temperature reduction is accompanied with entropy creation and exergy destroyed, respectively [17].

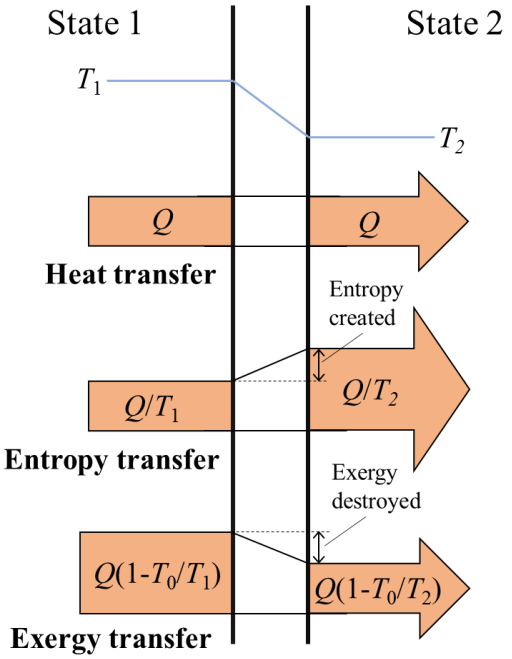

Figure 4.7. Relationship between energy, entropy, and exergy.

This study is to explain and use the exergy concept in the supercritical CO_2 Rankine cycle system be associated with the efficiency with based on the second law of thermodynamics.

4.3 Exergy analysis in supercritical CO_2 solar Rankine cycle system

The development of a thermally driven pump in supercritical CO_2 solar Rankine cycle system (SRCS) has been carried out and investigated to increase the system efficiency in field operation. In order to confirm the advantage of the thermally driven pump over conventional mechanical feed pump,

the energy and exergy balance of the system is calculated and discussed based on the theory verified in the previous section. It was found that the thermally driven pump operating under an actual climate condition gives the higher exergetic efficiency in output power compared with the mechanical feed pump. On the contrary, the high rate of exergy destruction is found in the evacuated solar collector under both system conditions. To increase the exergetic efficiency and to prevent the destruction rate, the proper components design, which can be considered as the essential factor to develop the higher performance system, are suggested in the present chapter.

The SRCS consists of an evacuated solar collector, turbine, heat exchanger units and the mechanical feed pump, with which in the previous investigation the fundamental system performance was investigated for the electric and thermal energy generation. However, in SRCS, the mechanical feed pump was used as a driving device that the external energy input is required to operate with the mechanical movement part, causing the mechanical loss. From these reasons, the mechanical fees pump resulted in decreasing the overall efficiency of the system with extra consumption from the electric energy generation of SRCS, which reduced the reliability and stability of the system at the same time. To conquer these problems, the new development in SRCS is attempted to develop a thermally driven pump, which was introduced and installed in the system instead of the mechanical feed pump [18~19]. The thermally driven pump is believed to give advantages of no energy consumption and high reliability to the system. However, in the recent development, non-continual flow symptom is found in CO_2 outlet of the thermally driven pump in a trial run due to its intermittent heating and cooling processes.

The details of SRCS with the thermally driven pump will be discussed in the next section together with the test conditions (in comparison with the mechanical feed pump).

4.3.1 System description

The schematic diagram of SRCS with the mechanical feed pump and with the thermally driven pump is outlined in Figure 4.8. The SRCS can be operated and examined its performance by either using the mechanical feed pump or the thermally driven pump. The working principle of SRCS is referred to section 3.1 in Chapter 3.

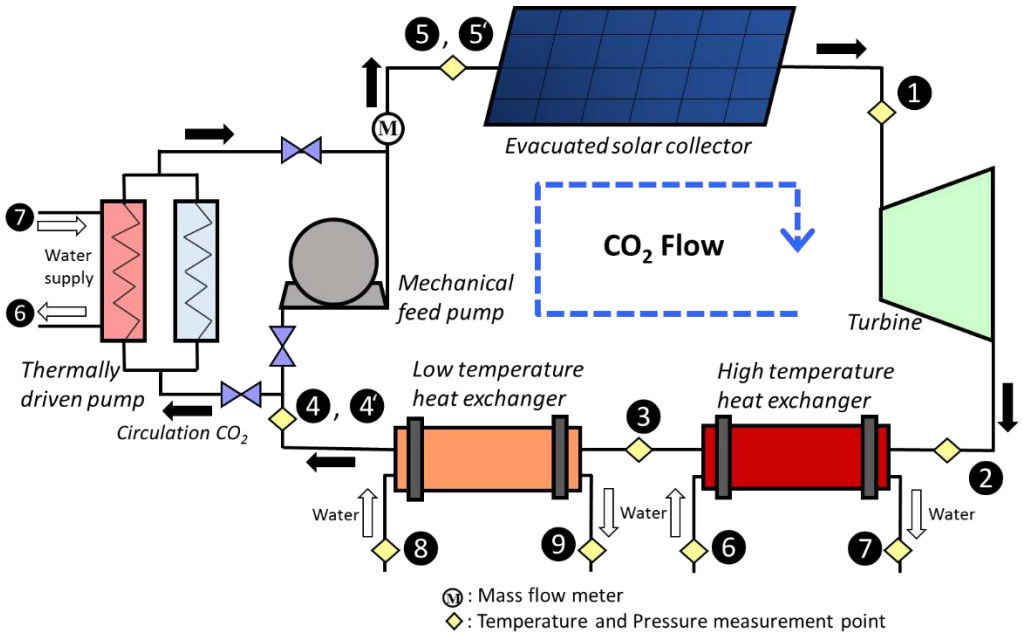

Figure 4.8. Schematic diagram of SRCS with the mechanical feed pump and with the thermally driven pump.

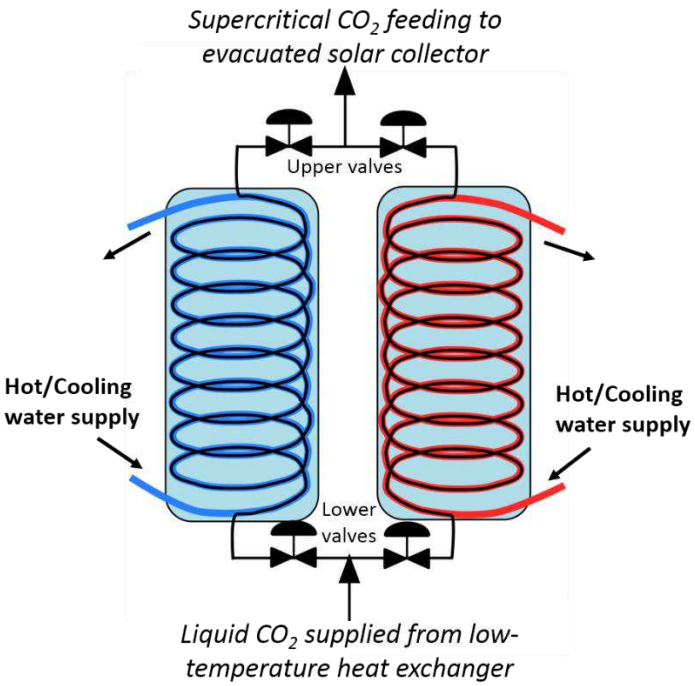

Figure 4.9. Schematic of the thermally driven pump using in SRCS.

The thermally driven pump is a refrigerant (liquid CO_2)-circulation pump, which uses hot and cold water for pressurizing and depressurizing CO_2 inside the device. The thermally driven pump consists of two expansion tanks with cooling and heating function. The schematic of the thermally driven pump is drawn in Figure 4.9. The expansion tanks are designed and manufactured as a high-pressure vessel with a maximum operating pressure of 12 MPa. In the operation of the thermally driven pump, lower valves are opened, and low-pressure CO_2 (5 MPa) from low-temperature heat exchanger flows into one (lower pressure tank, while another tank is kept at higher pressure) tank by the exerted pressure difference. After filling CO_2 in one tank, hot water is supplied subsequently for heating CO_2 to high-pressure supercritical state (5 MPa to 8 MPa), and CO_2 turns into a supercritical state. When CO_2 becomes a high-pressure state in the tank, the upper valve is opened, and the supercritical CO_2 expands and flows toward the evacuated solar collector by the exerted pressure difference. After CO_2 flowing out from the tank, cold water is used to reduce the pressure in the tank (to be lower than 5 MPa), and then the tank is filled by liquid CO_2 from the low-temperature heat exchanger. Following the process, both tanks are continuously operated to achieve progressively high-pressure state and low-pressure state in both tanks, making a thermally driven pump able to charge CO_2 into the evacuated solar collector as if the mechanical feed pump does.

4.4 Experimental factor

The field experiment to investigate the exergy and energy balance of SRCS, the typical sunny days of the winter season (12th December 2017 and 4th January 2018 for the mechanical feed pump and the thermally driven pump, respectively) at noon in Kyoto, Japan are selected as a reference for measurement. The cascade arrangement of the evacuated solar collector in 15 panels with the total solar collective area of 9.6 m^2 (A) is used for the experiment. The needle valve as an expander is used in the experiment, instead of an actual turbine, to prevent mechanical loss and to clarify the characteristic of the thermally driven pump alone in the system. The valve is operated in the ambient weather with an adjustable range of 0.0 to 30.00 mm. The temperature and pressure sensors are used to measure temperature and pressure by components in the SRCS while operated (refers to Figure 4.8). In the

present study, actual electric energy from the turbine generator is not generated from the system as stated above. Therefore the system performance is estimated based on thermodynamic cycle analysis.

4.4.1 Thermodynamic cycle analysis of SRCS

The system analysis as described above in field test is based on a steady state, namely steady flow process, for which mass, energy, and exergy balance equations are adopted by neglecting effects of potential and kinetic energy. The reference state of CO_2 is set for 0 °C at saturated liquid, which is 200 kJ/Kg of enthalpy and 1.0 kJ/kg·K of entropy, and the reference state of water is adjusted to set as 0 of enthalpy and entropy for 0 °C saturated liquid. The efficiencies for the turbine (η_t) and mechanical feed pump (η_{fp}) are assumed as 0.9 and 0.8, respectively for analysis in this study [20]. The energy and exergy balance analysis for SRCS with the mechanical feed pump and with the thermally driven pump are subsequently evaluated and compared in the same operating condition. The flow rate of water in the high-temperature heat exchanger ($\dot{m}_{HX1}$) and the low-temperature heat exchanger ($\dot{m}_{HX2}$) are fixed to the range of 600 to 700 kg/h and 1,200 to 1,300 kg/h, respectively.

It is noted that all CO_2 thermo-physical properties used in this study are obtained and calculated from the PROPATH database [21], while the properties of water are based on IAPWS [22].

4.5 Exergy evaluation

The thermodynamic cycle performance on energy balance following the first law of thermodynamics and exergy balance following the second law of thermodynamics in SRCS is obtained from a mathematical model in components [23~25]. The procedure of calculating by the parameters by components, (i) ~ (vi) and efficiencies (vii) can be written as follows, by number 1~9 indicate the positions ① ~ ⑨ shown in Figure 4.8, and 0 for the dead state;

(i) Evacuated solar collector (Process 5 – 1)

Heat transfer rate $\dot{Q}_s$ of CO_2 in the evacuated solar collector is:

$$\dot{Q}_s = \dot{m}_{CO_2}\left(h_1 - h_5\right) \tag{4.25}$$

Moreover, the heat loss $\dot{Q}_{loss,s}$ can be estimated:

$$\dot{Q}_{loss,s} = IA - \dot{Q}_s \tag{4.26}$$

Thus, the exergy rate which can be calculated from [26]:

$$\dot{E}_{\dot{Q}_s} = \dot{Q}_s\left[1 + \frac{1}{3}\left(T_0 / T_{sr}\right)^4 - \frac{4}{3}\left(T_0 / T_{sr}\right)\right] \tag{4.27}$$

where T_0 is the ambient temperature, and T_{sr} is the solar radiation temperature assumed as 5,800 K [27].

The change in exergy rate $\dot{E}_1 - \dot{E}_5$ across the evacuated solar collector can be determined from equation (4.23) as:

$$\dot{E}_1 - \dot{E}_5 = \dot{m}_{CO_2}\left[h_1 - h_5 - T_0\left(s_1 - s_5\right)\right] \tag{4.28}$$

Finally, the exergy destruction rate Π_s should be obtained as:

$$\Pi_s = \dot{E}_{\dot{Q}_s} - \left(\dot{E}_1 - \dot{E}_5\right) \tag{4.29}$$

(ii) Turbine (Process 1 –2)

Energy balance $\dot{Q}_t$ in turbine (the expansion valve) is:

$$\dot{Q}_t = \dot{m}_{CO_2}\left(h_1 - h_2\right) \tag{4.30}$$

The power W_t of turbine can be written as:

$$W_t = \dot{Q}_t \eta_t \tag{4.31}$$

And the exergy rate change $\dot{E}_1 - \dot{E}_2$ from the inlet and outlet of turbine is:

$$\dot{E}_1 - \dot{E}_2 = \dot{m}_{CO_2}\left[h_1 - h_2 - T_0\left(s_1 - s_2\right)\right] \tag{4.32}$$

Thus, the exergy destruction rate Π_t of turbine is calculated as:

$$\Pi_t = \left(\dot{E}_1 - \dot{E}_2\right) - W_t \tag{4.33}$$

(iii) High temperature heat exchanger (Process 2 – 3)

The heat transfer rate $\dot{Q}_{HX1}$ leaving high temperature heat exchanger is:

$$\dot{Q}_{HX1} = \dot{m}_{Water_{HX1}}\left(h_7 - h_6\right) \tag{4.34}$$

For heat loss $\dot{Q}_{loss,HX1}$ in high temperature heat exchanger, it can be calculated as:

$$\dot{Q}_{loss,HX1} = \dot{m}_{CO_2}\left(h_2 - h_3\right) - \dot{m}_{Water_{HX1}}\left(h_7 - h_6\right) \tag{4.35}$$

The exergy balance $\dot{E}_2 - \dot{E}_3$ across the high temperature heat exchanger can be written as:

$$\dot{E}_2 - \dot{E}_3 = \dot{m}_{CO_2}\left[h_2 - h_3 - T_0\left(s_2 - s_3\right)\right] \tag{4.36}$$

And exergy balance rate $\dot{E}_7 - \dot{E}_6$ for water heat absorption in the high temperature heat exchanger is determined as:

$$\dot{E}_7 - \dot{E}_6 = \dot{m}_{Water_{HX1}}\left[h_7 - h_6 - T_0\left(s_7 - s_6\right)\right] \tag{4.37}$$

Thus, the exergy destruction rate Π_{HX1} of high temperature heat exchanger can be obtained from:

$$\Pi_{HX1} = \left(\dot{E}_2 - \dot{E}_3\right) - \left(\dot{E}_7 - \dot{E}_6\right) \tag{4.38}$$

(iv) Low temperature heat exchanger (Process 3 – 4)

The heat transfer rate $\dot{Q}_{HX2}$ leaving low temperature heat exchanger is calculated as:

$$\dot{Q}_{HX2} = \dot{m}_{Water_{HX2}}\left(h_9 - h_8\right) \tag{4.39}$$

Heat loss $\dot{Q}_{loss,HX2}$ in low temperature heat exchanger is:

$$\dot{Q}_{loss,HX2} = \dot{m}_{CO_2}\left(h_3 - h_4\right) - \dot{m}_{Water_{HX2}}\left(h_9 - h_8\right) \tag{4.40}$$

For the exergy balance $\dot{E}_3 - \dot{E}_4$ across the low temperature heat exchanger, it can be obtained from:

$$\dot{E}_3 - \dot{E}_4 = \dot{m}_{CO_2}\left[h_3 - h_4 - T_0\left(s_3 - s_4\right)\right] \tag{4.41}$$

And exergy balance rate $\dot{E}_9 - \dot{E}_8$ for water heat absorption in the low temperature heat exchanger is:

$$\dot{E}_9 - \dot{E}_8 = \dot{m}_{\text{Water}_{\text{HX2}}} \left[h_9 - h_8 - T_0 \left(s_9 - s_8 \right) \right] \tag{4.42}$$

Hence, the exergy destruction rate Π_{HX2} of low temperature heat exchanger can be calculated as:

$$\Pi_{\text{HX2}} = \left(\dot{E}_3 - \dot{E}_4 \right) - \left(\dot{E}_9 - \dot{E}_8 \right) \tag{4.43}$$

(v) Mechanical feed pump (Process 4 – 5)

Energy balance $\dot{Q}_{\text{fp}}$ of mechanical feed pump is:

$$\dot{Q}_{\text{fp}} = \dot{m} \left(h_5 - h_4 \right) \tag{4.44}$$

And the power W_{fp} required for mechanical feed pump can be estimated as:

$$W_{\text{fp}} = \frac{\dot{Q}_{\text{fp}}}{\eta_{\text{fp}}} \tag{4.45}$$

The change of exergy $\dot{E}_5 - \dot{E}_4$ in mechanical feed pump process is:

$$\dot{E}_5 - \dot{E}_4 = \dot{m}_{\text{CO}_2} \left[h_5 - h_4 - T_0 \left(s_5 - s_4 \right) \right] \tag{4.46}$$

Thus, the exergy destruction rate Π_{fp} in mechanical feed pump is obtained from:

$$\Pi_{\text{fp}} = W_{\text{fp}} - \left(\dot{E}_5 - \dot{E}_4 \right) \tag{4.47}$$

(vi) Thermally driven pump (Process 4' – 5')

Energy balance $\dot{Q}_{\text{tp}}$ for thermally driven pump is:

$$\dot{Q}_{\text{tp}} = \dot{m} \left(h_{5'} - h_{4'} \right) \tag{4.48}$$

And change in exergy $\dot{E}_{5'} - \dot{E}_{4'}$ across thermally driven pump is calculated as:

$$\dot{E}_{5'} - \dot{E}_{4'} = \dot{m}_{\text{CO}_2} \left[h_{5'} - h_{4'} - T_0 \left(s_{5'} - s_{4'} \right) \right] \tag{4.49}$$

For the exergy destruction rate Π_{tp} in thermally driven pump, it can be estimated as:

$$\Pi_{\text{tp}} = \left(\dot{E}_{5'} - \dot{E}_{4'} \right) + \left(\dot{E}_7 - \dot{E}_6 \right) \tag{4.50}$$

(vii) Efficiencies analysis

Deriving the performance by components above, (i) ~ (vi), the overall performance of the system will be given for the system thermal efficiency of SRCS with the mechanical feed pump ($\eta_{\text{th,fp}}$) and with the thermally driven pump ($\eta_{\text{th,tp}}$), respectively:

$$\eta_{\text{th,fp}} = \frac{W_{\text{net}_{\text{fp}}}}{Q_{\text{in}}} = \frac{W_{\text{t}} + \dot{Q}_{\text{HX1}} + \dot{Q}_{\text{HX2}} - W_{\text{fp}}}{Q_{\text{s}}} \tag{4.51}$$

and

$$\eta_{\text{th,tp}} = \frac{W_{\text{net}_{\text{tp}}}}{Q_{\text{in}}} = \frac{W_{\text{t}} + \dot{Q}_{\text{HX2}}}{Q_{\text{s}}} \tag{4.52}$$

The exergetic efficiency (determined from equation (4.24)), the evaluation on the true performance of an energy system from the thermodynamic viewpoint of SRCS with the mechanical feed pump ($\eta_{e,fp}$) and with the thermally driven pump ($\eta_{e,tp}$) can be written as:

$$\eta_{e,fp} = \frac{W_t + \left(\dot{E}_7 - \dot{E}_6\right) + \left(\dot{E}_9 - \dot{E}_8\right)}{\dot{E}_{\dot{Q}_s} + W_{fp}} \tag{4.53}$$

and

$$\eta_{e,tp} = \frac{W_t + \left(\dot{E}_9 - \dot{E}_8\right)}{\dot{E}_{\dot{Q}_s}} \tag{4.54}$$

The exergy destruction, which is a measure of the irreversibility in an object is an essential parameter in exergy modeling. It can be defined here from the potential work lost due to the irreversibility in a particular element of the system. The total exergy destruction of SRCS with the mechanical feed pump ($\Pi_{Total,fp}$) and with the thermally driven pump ($\Pi_{Total,tp}$) can be thus defined as:

$$\Pi_{Total,fp} = \Pi_s + \Pi_t + \Pi_{HX1} + \Pi_{HX2} + \Pi_{fp} \tag{4.55}$$

and

$$\Pi_{Total,tp} = \Pi_s + \Pi_t + \Pi_{HX2} + \Pi_{tp} \tag{4.56}$$

By the contribution of components, (i) ~ (vi), the total exergy destruction rate $\eta_{\Pi i}$, in SRCS can be remitted as follows:

$$\eta_{\Pi_i} = \frac{\Pi_i}{\Pi_{Total}} \tag{4.57}$$

where Π_i is referred to the exergy destruction rate by each component in SRCS.

Finally, for by components of SRCS, the exergetic efficiency, which characterizes the performance of a system component from the thermodynamic viewpoint, can be defined by the exergetic availability [28]. The resultant equations for the exergetic efficiency for evacuated solar collector, turbine, high temperature heat exchanger, low temperature heat exchanger, mechanical feed pump and thermally driven pump can be found respectively below:

$$\eta_{x,s} = \frac{\dot{E}_1 - \dot{E}_5}{\dot{E}_{\dot{Q}_s}} \tag{4.58}$$

$$\eta_{x,t} = \frac{\dot{E}_t}{\dot{E}_1 - \dot{E}_2} = \frac{W_t}{\dot{E}_1 - \dot{E}_2} \tag{4.59}$$

$$\eta_{x,HX1} = \frac{\dot{E}_7 - \dot{E}_6}{\dot{E}_2 - \dot{E}_3} \tag{4.60}$$

$$\eta_{x,HX2} = \frac{\dot{E}_9 - \dot{E}_8}{\dot{E}_3 - \dot{E}_4} \tag{4.61}$$

$$\eta_{x,fp} = \frac{\dot{E}_5 - \dot{E}_4}{\dot{E}_{fp}} = \frac{\dot{E}_5 - \dot{E}_4}{W_{fp}} \tag{4.62}$$

$$\eta_{x,tp} = \frac{\dot{E}_{5'} - \dot{E}_{4'}}{\dot{E}_7 - \dot{E}_6} \tag{4.63}$$

4.6 Results and discussions

For the calculation on the energy and exergy balance of SRCS, the operation conditions of CO_2 circulation and hot/cooling water supply in each state are tabulated, where Table 4.1 and 4.2 present the parametric data for the operation of SRCS with the mechanical feed pump or the thermally driven pump, respectively. In the tables, it is noted that temperature, pressure, enthalpy, and mass flow rate of CO_2 circulation and hot/cooling water supply are given according to the thermodynamic process specified in Figure 4.8. As shown in Figure 4.8, high-pressure CO_2 is heated in an evacuated solar collector by solar energy, and it reaches the high-temperature supercritical state (⑤ → ①). At the outlet of the evacuated solar collector, supercritical CO_2 expands and drives the turbine generator. Electric energy is available and obtained from the turbine generator, while the CO_2 becomes a low-pressure state (① → ②). Due to the remaining high-temperature state, the circulation CO_2 is cooled in the high-temperature heat exchanger, with which heat energy can be recovered to use as a heat source for the refrigeration cycle (② → ③). In case of using the thermally driven pump in SRCS, heat energy obtained from the high-temperature heat exchanger is utilized as a heat source for the heating process in the thermally driven pump operation. The low-temperature heat exchanger is used to further cool down CO_2 to the liquid state, while the waste heat energy can be recycled for hot water supply purpose (③ → ④). After leaving heat exchanger units, CO_2 is pumped to the high-pressure state into the evacuated solar collector by the mechanical feed pump or by the thermally driven pump (④ → ⑤), and the cycle recommences. The SRCS is categorized as a trans-critical cycle involving to supercritical point and supercritical region CO_2 inside the Rankine cycle.

Table 4.1. Conditions of SRCS with the mechanical feed pump.

State	Fluid	Phase	$\dot{m}$ (kg/s)	P (MPa)	T (°C)	h (kJ/kg)	s (kJ/kg·K)
①	CO_2	Supercritical	0.0075	8.11	148.98	881.85	4.268
②	CO_2	Low pressure superheated vapor	0.0075	4.34	101.92	850.08	4.293
③	CO_2	Low pressure superheated vapor	0.0075	4.37	14.03	738.38	3.952
④	CO_2	Vapor-liquid mixture	0.0075	4.36	8.72	524.58	3.194
⑤	CO_2	Compressed liquid	0.0075	8.02	15.10	535.40	3.218
⑥	Water	Liquid	0.19	0.101325	20.88	87.36	0.308
⑦	Water	Liquid	0.19	0.101325	21.62	90.70	0.319
⑧	Water	Liquid	0.36	0.101325	6.33	26.58	0.096
⑨	Water	Liquid	0.36	0.101325	7.23	30.49	0.110

Table 4.2. Conditions of SRCS with the thermally driven pump.

State	Fluid	Phase	$\dot{m}$ (kg/s)	P (MPa)	T (°C)	h (kJ/kg)	s (kJ/kg·K)
①	CO_2	Supercritical	0.0085	7.89	105.21	829.45	4.141
②	CO_2	Low pressure superheated vapor	0.0085	6.26	85.02	816.34	4.142
③	CO_2	Low pressure superheated vapor	0.0085	6.44	38.29	742.84	3.919
④	CO_2	Low pressure liquid	0.0085	6.39	8.67	520.99	3.173
⑤	CO_2	Compressed liquid	0.0085	8.15	26.41	569.93	3.333
⑥	Water	Liquid	0.17	0.101325	41.20	172.63	0.588
⑦	Water	Liquid	0.17	0.101325	42.41	177.65	0.604
⑧	Water	Liquid	0.36	0.101325	8.71	36.66	0.131
⑨	Water	Liquid	0.36	0.101325	9.82	41.28	0.148

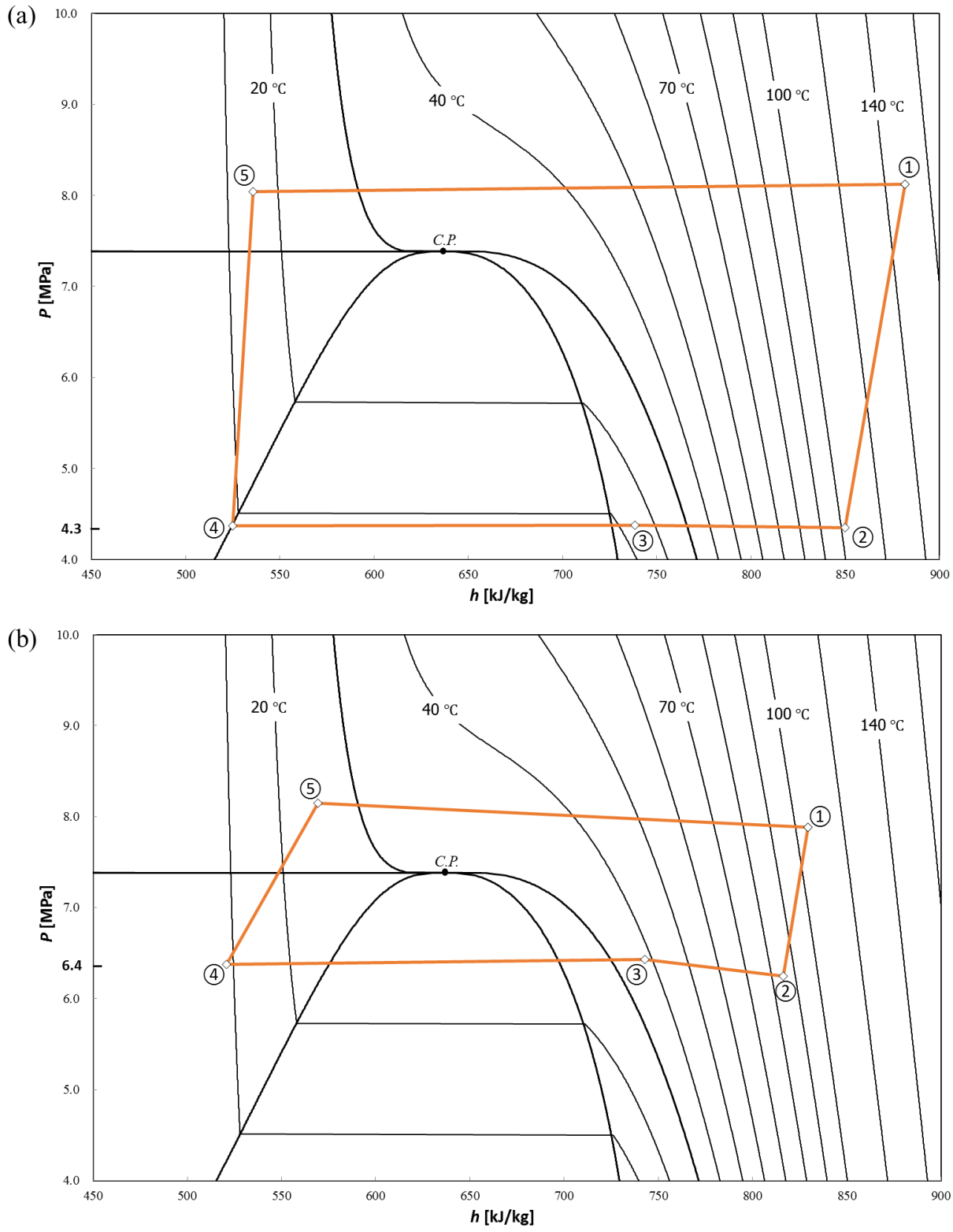

Figure 4.10. *P-h* diagram of SRCS with (a) mechanical feed pump and with (b) thermally driven pump.

The *P-h* cycle diagrams of SRCS with the two conditions (Table 4.1 and 4.2) are shown in Figure 4.10. Approximately the same value of solar radiation on time average during the experiments are selected for the field operation of SRCS for the sake of comparison between the mechanical feed

pump and the thermally driven pump. The time-averaged values are 0.459 kW/m^2 and 0.422 kW/m^2, respectively. As shown in the Figure 4.10, the transcritical CO_2 thermodynamic cycles are achieved in both SRCS with the mechanical feed pump and with the thermally driven pump throughout the operation. In Figure 4.10 (a), it can be obviously seen that the cycle reaches to the supercritical high pressure at around 8 MPa, where the simultaneous heating process takes place at the temperature from 15.1 °C to 148.98 °C in evacuated solar collector (⑤ → ① in Figure 4.10 (a)). For the subcritical low pressure, the pressure at around 4.3 MPa is obtained with heat recovery process of 101.92 °C to 8.72 °C in heat exchanger units (② → ④ in Figure 4.10 (a)). Particularly in case of SRCS with the thermally driven pump, the pressure of around 8 MPa and the temperature rise from 26.41 °C to 105.21 °C is achieved at supercritical high pressure in the heating process (evacuated solar collector, ⑤ → ① in Figure 4.10 (b)). For the subcritical low pressure, the pressure of around 6.4 MPa and the temperature from 85.02 °C to 8.67 °C is obtained in the heat recovery process (heat exchanger units, ② → ④ in Figure 4.10 (b)).

From both cycle conditions, it can be seen that the heating processes in the Rankine cycle are in the supercritical region for CO_2. That is to say, under the supercritical state, CO_2 absorbs the thermal energy (heat energy) in the evacuated solar collector. Also, small pressures changes are found between the pump component and evacuated solar collector, and between the heat exchanger units for both cycle conditions. It can be indicated that the flow through these components is continuous (in Figure 4.10). The pressure difference in the cycle (supercritical high pressure and subcritical low pressure) of SRCS with the mechanical feed pump and with the thermally driven pump is approximately 2.7 MPa and 1.6 MPa, respectively. The lower in pressure difference in the cycle with the thermally driven pump is due to the working principle of the thermally driven pump itself, indicating that the oscillatory flow in the cycle is inevitable throughout the alternative heating and cooling process [18~19]. In the operating range of the transcritical CO_2 cycle system, it is understood that the pressure difference of the turbine generator affects the system thermal efficiency in more significant extent [29].

Using the data provided in Table 4.1 and 4.2, the physical understanding of the energy and exergy of SRCS is then calculated using the equations provided in the previous section, and all necessary thermodynamic parameters are cited from the field experiment, as described in Figure 4.10. The phenomenological details on the rate of energy balance and exergy balance are explained in the following paragraphs [30].

In the analysis of energy balance, the input energy rate of SRCS obtained from equation (4.25) together with equation (4.45) is 4.508 kW, which comes from the evacuated solar collector, when the mechanical feed pump is used, while the output energy rate of operating SRCS is 2.257 kW, which comes from both the turbine generator (equation (4.31)) and heat recovery from heat exchanger units (equations (4.34) and (4.39)). For the SRCS with the thermally driven pump, however, the input energy rate is only from the evacuated solar collector, which is 4.032 kW, and the output energy of 1.763 kW comes from both the turbine and low-temperature heat exchanger, with equations (4.31) and (4.39), respectively. It can be found that the output energy rate of SRCS with the thermally driven pump is lower than that with the mechanical feed pump. The reason is chiefly that of the output energy from the high-temperature heat exchanger, for which additional energy has to be supplied to the thermally driven pump itself for operation, although there is no actual electric energy consumption is required in operation.

Based on the field operation as shown in Figure 4.10, the system thermal efficiency of SRCS can be calculated from equations (4.51) and (4.52). It is found that SRCS with the mechanical feed pump gives higher efficiency compared with the thermally driven pump, which is respectively 82.64 % and 79.87 %. The lower in thermal efficiency of SRCS with the thermally driven pump is due to the low-pressure difference in the cycle. Furthermore, the slightly lower solar radiation has also been affected by the thermal efficiency to some extent. It is noted here that there is no electric energy

consumption required to operate the thermally driven pump, with which the total electric energy can be generated genuinely from the power device (the turbine) of the system without any external electric energy consumption.

In term of exergetic efficiency, the rational performance to compare both quantities of input and output energy in the system, which can be obtained from equations (4.53) and (4.54) for SRCS with the mechanical feed pump and with the thermally driven pump, is 11.47 % and 20.28 %, respectively. The higher in the exergetic efficiency of SRCS with the thermally driven pump is derived from the fact that the thermally driven pump gives much high-quality energy that is available to convert to work compared with the mechanical feed pump. From the efficiencies analysis of the system, it can be speculated that the different values of the efficiency come from the irreversibility in the process of components in the thermal efficiency calculation.

Table 4.3 shows the contribution (in percent) of by components in the system to total exergy destruction rate, which is obtained in equations (4.55) to (4.57) for SRCS with the mechanical feed pump or with the thermally driven pump. The exergy destruction represents the exergy destroyed in the irreversibility process in by components, which are caused by many factors such as heat transfer loss, friction or chemical reaction [31]. In the case of SRCS with the mechanical feed pump, the evacuated solar collector has 89.99 % of exergy destruction rate, and the turbine has next highest percent contribution with a value of 3.31 %, following the mechanical feed pump, the low-temperature heat exchanger and the high-temperature heat exchanger (3.01 %, 2.47 %, and 1.23 %, respectively). For the SRCS with the thermally driven pump, the exergy destruction rate of 76.28 %, 12.63 % and 10.57 % are found in the evacuated solar collector, the low temperature heat exchanger and the thermally driven pump itself, respectively, while the lowest contribution can be found in the turbine at only 0.51 %, indicating that the thermally driven pump gives better performance characteristic in term of exergy efficiency in the electric energy generation to the system. From the Table 4.3, it can be observed that the highest contribution to the exergy destruction rate can be found in the evacuated solar collector for both system conditions. It is due to the heat losses occurred in the evacuated solar collector.

It is noticed from Table 4.3 that the thermally driven pump (Π_{tp}) itself has a higher order contribution to the total exergy destruction rate in comparison with the mechanical feed pump (Π_{fp}). The reason can be thought that the thermal energy (heat) of the thermally driven pump is much higher than that of the electric energy input to the mechanical feed pump when the exergy is calculated.

Table 4.3. Percentage of exergy destruction rate by components.

SRCS	Π_s	Π_t	Π_{HX1}	Π_{HX2}	Π_{fp}	Π_{tp}	%
with mechanical feed pump	89.99	3.31	1.23	2.47	3.01		
with thermally driven pump	76.28	0.51		12.63		10.57	

The calculated exergetic parameter in by components is listed in Table 4.4 for the representative operation (Figure 4.10) of SRCS with the mechanical feed pump or with the thermally driven pump. Table 4.4 shows exergetic efficiency (obtained from equations (4.58) through (4.63)) of evacuated solar collector $\eta_{x,s}$, turbine $\eta_{x,t}$, high temperature heat exchanger $\eta_{x,HX1}$, low temperature heat exchanger $\eta_{x,HX2}$, and the mechanical feed pump $\eta_{x,fp}$ or the thermally driven pump $\eta_{x,tp}$ for both system conditions. From the presented results, it can be inferred that the turbine has exergetic efficiencies of 72.86 % and 88.74 % for the operation of representative SRCS with the mechanical feed pump or with the thermally driven pump, respectively. These efficiencies can be considered as relatively high, indicating that the turbine component can be regarded as the highest performance component, in which the electric power generation from the turbine can be considered as a principal (high quality) output energy of SRCS rather than the thermal energy supplied from heat exchanger units. On the other hand, relative low exergetic efficiency is found in the evacuated solar collector component for both mechanical feed pump and thermally driven pump conditions (10.30 % and 7.84 %, respectively). The heat exchanger units in

SRCS with the mechanical feed pump has higher exergetic efficiencies, which are 60.00 % and 33.86 % for high temperature and low-temperature heat exchanger, respectively, compared with the thermally driven pump, 23.15 %, and 0.92 %, respectively. The reasons for low in the exergetic efficiency in heat exchanger units are mainly due to the irreversibility associated with heat transfer over finite temperature differences [32]. Moreover, the operation characteristic of the thermally driven pump can be considered as the same as the heat exchanger operation (evaporator), which resultantly shows lower in the exergetic efficiency (3.03 %).

The exergy destruction rates by components are given in Table 4.3, and exergetic efficiencies for each component are given in Table 4.4. Here, it can be observed from the tables that the evacuated solar collector has a maximum exergy destruction rate and low exergetic efficiency in both system conditions. In order to increase the performance and reduce the exergy destruction of SRCS, careful attention should be paid to the heat losses from the evacuated solar collector. The optimum design on the evacuated solar collector must be required to develop the further efficient system.

Table 4.4. Exergetic efficiencies by components.

SRCS	$\eta_{x,s}$	$\eta_{x,t}$	$\eta_{x,HX1}$	$\eta_{x,HX2}$	$\eta_{x,fp}$	$\eta_{x,tp}$	%
with mechanical feed pump	10.30	72.86	60.00	33.86	28.24		
with thermally driven pump	7.84	88.74	23.15	0.92		3.03	

Since the thermally driven pump has been developed to increase the overall performance of SRCS, weather conditions of summer and autumn are acquired to evaluate the exergetic efficiency of by components under SRCS operation. The typical days in summer (29th August 2017) and autumn (9th November 2017) are selected as references also of winter (4th January 2018) for the field test of SRCS with the thermally driven pump. Figure 4.11 presents the comparison of the exergetic efficiency of by components (i.e., evacuated solar collector, turbine, high-temperature heat exchanger, low-temperature heat exchanger and thermally driven pump) in three weather conditions. It can be seen that the exergetic efficiency of the turbine is the highest in winter condition. It is because of the pressure difference between the supercritical (high) pressure and subcritical (low) pressure in the cycle, i.e., a higher (1.6 MPa) in winter as compared with autumn and summer conditions (1.4 MPa and 0.9 MPa, respectively).

The exergetic efficiency of the high-temperature heat exchanger can be found at the highest in summer condition (64 %), while the lowest efficiency is in the winter condition (23.15 %) as shown in Figure 4.11. The trend comes from low ambient temperature in winter effects directly to water temperature used in the heat exchanger. However, the variation of exergetic efficiency in the evacuated solar collector, the low-temperature heat exchanger, and the thermally driven pump shows minimal change in weather conditions as shown in Figure. 4.11.

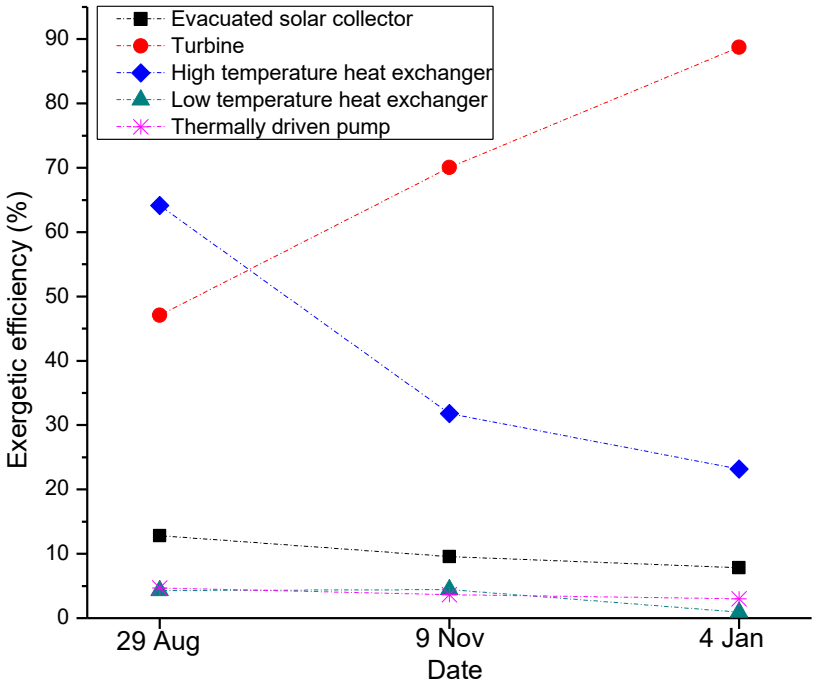

Figure 4.11. Percentage of exergetic efficiencies by components in SRCS with thermally driven pump in summer; August 29, 2017, autumn; November 9, 2017, and winter; January 4, 2018.

From the results as obtained in Figure 4.11, it can be observed that the factor in weather condition has much effect on the exergetic efficiency of the turbine and the high-temperature heat exchanger. Although in the present study the SRCS field test gave the excellent understanding to the performance characteristic of the system and as well as to the consisted by components, further factors (such as wind, humidity, etc.) may have to be considered for further obtaining accurate data in the more detailed understanding of the system.

The analysis of exergetic efficiency in SRCS is a methodological approach to investigate the performance of the system. It can help to assess and compare the energy system with different conditions. The energy analysis conducted in the present study provides a primary inspect of technological efficiencies, whereas the exergy analysis gives a detailed understanding of the imperfections of the energy conversion systems. The components in SRCS have to be developed with higher efforts to increase the energy and exergy efficiency, also to prevent the losses in term of energy and exergy, especially in the evacuated solar collector. Furthermore, the thermally driven pump, which plays an essential role as a critical development element in the renewable energy cycle system, has to be further investigated for higher overall efficiency.

4.7 Conclusions

The systematic comparison with the energy and exergy balance of SRCS with the mechanical feed pump or the thermally driven pump is given. Performance characteristics of significant components in the system are also investigated in term of exergetic efficiency. From the present field tests, the following results were obtained;

i. The thermal efficiency of SRCS with the mechanical feed pump is higher compared with the thermally driven pump. The reason comes from the lower value of the pressure difference between supercritical (high) pressure and subcritical (low) pressure with the thermally driven pump. There is no electric consumption to the system with the thermally driven pump.

ii. By using the thermally driven pump to the system, the exergetic efficiency was found higher compared with that of the mechanical feed pump; 20.28 % and 11.47 %, respectively.
iii. The highest rate of exergy destruction rate is found in the evacuated solar collector. In case of SRCS with the mechanical feed pump, higher exergy destruction rate (89.99 %) was obtained compared with the system with thermally driven pump (76.28 %). It is due to the heat loss in the evacuated solar collector.
iv. Weather (seasonal) conditions have much effect on the exergetic efficiency of by components in SRCS with the thermally driven pump, especially in turbine and high-temperature heat exchanger. In winter, the turbine gives highest exergetic efficiency, whereas the high-temperature heat exchanger gives the lowest exergetic efficiency in summer and autumn operations.

It can be concluded in term of energy and exergy analysis that the thermally driven pump helps the system to have higher performance characteristics. However, it is suggested that the optimization in designing by components is required to enhance the highest performance in seasonal operations.

References

[1] Kanoglu, M., Dincer, I. and Rosen, M.A., 2007. Understanding energy and exergy efficiencies for improved energy management in power plants. *Energy Policy*, 35(7), pp.3967-3978.
[2] Hepbasli, A., 2008. A key review on exergetic analysis and assessment of renewable energy resources for a sustainable future. *Renewable and sustainable energy reviews*, *12*(3), pp.593-661.
[3] Pope, K., Dincer, I. and Naterer, G.F., 2010. Energy and exergy efficiency comparison of horizontal and vertical axis wind turbines. *Renewable energy*, *35*(9), pp.2102-2113.
[4] Chandra, S., Energy and the First Law of Thermodynamics. *Energy, Entropy and Engines: An Introduction to Thermodynamics*, pp.72-132.
[5] Kanoğlu, M., Çengel, Y.A. and Dinçer, İ., 2012. The First and Second Laws of Thermodynamics. In *Efficiency Evaluation of Energy Systems* (pp. 9-26). Springer, New York, NY.
[6] Chandra, S., The Second Law of Thermodynamics. *Energy, Entropy and Engines: An Introduction to Thermodynamics*, pp.168-217.
[7] Çengel, Y.A. and Michael, A.B., Thermodynamics: An Engineering Approach, 6th edn., 2008.
[8] Clausius, R., 1850. Über die bewegende Kraft der Wärme und die Gesetze, welche sich daraus für die Wärmelehre selbst ableiten lassen. *Annalen der Physik*, *155*(3), pp.368-397.
[9] Planck, M., 1958. Treatise on Thermodynamics, trans. from seventh German ed., 1922.
[10] Winterbone, D. and Turan, A., 2015. *Advanced thermodynamics for engineers*. Butterworth-Heinemann.
[11] Krakow, K.I., 1991. Exergy analysis: dead-state definition. *ASHRAE Transactions*, *97*(1), pp.328-336.
[12] Dincer, I., 2002. The role of exergy in energy policy making. *Energy policy*, *30*(2), pp.137-149.
[13] Moran, M.J., Shapiro, H.N., Boettner, D.D. and Bailey, M.B., 2010. *Fundamentals of engineering thermodynamics*. John Wiley & Sons.
[14] Brzustowski, T.A. and Golem, P.J., 1976. Second-Law Analysis of Energy Processes Part I: Exergy—An Introduction. *Transactions of the Canadian Society for Mechanical Engineering*, *4*(4), pp.209-226.
[15] Moran, M.J., 1982. *Availability analysis: a guide to efficient energy use.* Prentice-Hall, Englewood Cliffs, N.J.
[16] Michaelides, E.E., 1984. The second law of thermodynamics as applied to energy conversion processes. *International journal of energy research*, *8*(3), pp.241-246.
[17] Sandnes, B., 2003. Exergy efficient production, storage and distribution of solar energy. *PhD. Dissertation of Department of Physics, University of Oslo, Oslo, Norway.*

[18] Yamaguchi, H., Zhang, X.R., Niu, X.D. and Hashitani, N., 2013. A novel thermally driven pump and its test in a supercritical CO_2 loop system. *International Journal of Energy Research*, *37*(11), pp.1331-1338.
[19] Kuwahara, T., Niu, X.D., Yamaguchi, H., Iwamoto, Y. and Zhang, X.R., 2011. Performance study of supercritical CO_2-based solar Rankine cycle system with a novel-concept thermally driven pump. *Proceedings of the Institution of Mechanical Engineers, Part A: Journal of Power and Energy*, *225*(4), pp.413-419.
[20] Zhang, X.R., Yamaguchi, H., Uneno, D., Fujima, K., Enomoto, M. and Sawada, N., 2006. Analysis of a novel solar energy-powered Rankine cycle for combined power and heat generation using supercritical carbon dioxide. *Renewable Energy*, *31*(12), pp.1839-1854.
[21] PROPATH Group, 1997. PROPATH: a program package for thermophysical properties.
[22] Wagner, W. and Pruß, A., 2002. The IAPWS formulation 1995 for the thermodynamic properties of ordinary water substance for general and scientific use. *Journal of physical and chemical reference data*, *31*(2), pp.387-535.
[23] Suzuki, A., 1988. General theory of exergy-balance analysis and application to solar collectors. *Energy*, *13*(2), pp.153-160.
[24] Tsatsaronis, G. and Cziesla, F., 2004. *Exergy and thermodynamic analysis*, Exergy, Energy system analysis, and optimization, EOLSS Publishers Company Ltd.
[25] Grosu, L., Marin, A., Dobrovicescu, A. and Queiros-Conde, D., 2016. Exergy analysis of a solar combined cycle: organic Rankine cycle and absorption cooling system. *International Journal of Energy and Environmental Engineering*, *7*(4), pp.449-459.
[26] Petela, R., 2003. Exergy of undiluted thermal radiation. *Solar Energy*, *74*(6), pp.469-488.
[27] Ruppel, W. and Wurfel, P., 1980. Upper limit for the conversion of solar energy. *IEEE Transactions on Electron Devices*, *27*(4), pp.877-882.
[28] Spayde, E., Mago, P.J. and Cho, H., 2017. Performance Evaluation of a Solar-Powered Regenerative Organic Rankine Cycle in Different Climate Conditions. *Energies*, *10*(1), p.94.
[29] Guo, T., Wang, H. and Zhang, S., 2010. Comparative analysis of CO_2-based transcritical Rankine cycle and HFC245fa-based subcritical organic Rankine cycle using low-temperature geothermal source. *Science China Technological Sciences*, *53*(6), pp.1638-1646.
[30] Pumaneratkul, C., Horino, T., Yamasaki, H. and Yamaguchi, H., 2018. Exergy Analysis of Development on Supercritical CO_2 Solar Rankine Cycle System with Thermally Driven Pump. *Cogent Engineering*, 5(1), p.1475440.
[31] Mago, P.J., Srinivasan, K.K., Chamra, L.M. and Somayaji, C., 2008. An examination of exergy destruction in organic Rankine cycles. *International Journal of Energy Research*, *32*(10), pp.926-938.
[32] Chen, Q., Wang, M., Pan, N. and Guo, Z.Y., 2009. Optimization principles for convective heat transfer. *Energy*, *34*(9), pp.1199-1206.

Chapter 5

Development of CO_2-based photovoltaic-thermal hybrid system

The current trend of solar energy utilization has much relied on the electric energy generation from the photovoltaic solar panel, which converts the energy of light directly into electric power energy, while the thermal energy from the solar photovoltaic panel is wasted or instead regarded that the thermal energy may cause the photovoltaic solar panel efficiency lowering.

The photovoltaic-thermal hybrid system is one of the simplest and most effective ways to utilize the solar electric power and solar thermal energy at the same time [1]. The photovoltaic-thermal hybrid system is a combination of the photovoltaic solar panel for electric energy generation with a solar thermal collector, where the waste heat can be removed from the photovoltaic solar panel and can be applied for thermal energy generation as well as improving the performance of the photovoltaic solar panel. The combination of electric and thermal energy generation leads the system to higher efficiency altogether, and the system gives the high efficiency compared with an ordinary photovoltaic solar panel [2~3].

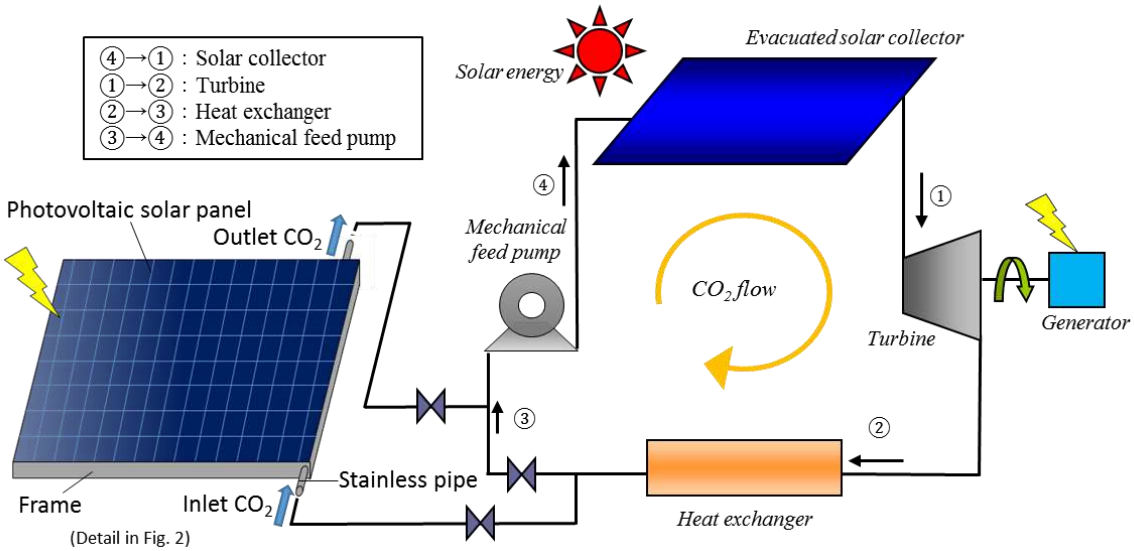

Figure 5.1. Schematic of the total system.

For the purpose of effectively using the solar energy, CO_2-based photovoltaic-thermal hybrid system has been designed and planned to install as an additional system of the supercritical CO_2 solar Rankine cycle system (SRCS), which utilizes solar energy as an energy source and CO_2 as a natural working fluid for the purpose of electric and thermal energy generation [4~5]. To improve the overall system efficiency, the CO_2-based photovoltaic-thermal hybrid system was installed at the outlet of the heat exchanger in SRCS in order to pre-heat CO_2 before feeding back to the evacuated solar collector by a mechanical feed pump. The schematic diagram and connection of SRCS and the CO_2-based photovoltaic-thermal hybrid system are drawn in Figure 5.1. It is to mention that the liquid CO_2 flow helps to decrease the surface temperature of the photovoltaic solar panel for the higher electric power generation as well as gaining thermal energy [6].

The (CO_2-based photovoltaic-thermal) hybrid system is composed of two main parts, namely an ordinary photovoltaic solar panel and the stainless pipe (as a heat exchanger from the solar panel to the liquid CO_2), which is installed on the backside of the photovoltaic solar panel via the thermally

conductive aluminum plate. The construction details of the CO_2-based photovoltaic-thermal hybrid system and its experiment apparatus will be discussed in the next section. The newly designed hybrid system solely operated and tested in a real representative weather conditions in Kyoto, Japan

In the standard fluid-based photovoltaic-thermal hybrid system, various type of working fluids has been selected to use by many researchers such as water or glycol [8]. From a CO_2-based photovoltaic-thermal hybrid system in this study, it is found that CO_2 gives better result in the trend of temperature distribution compared with using other type working fluids in the hybrid system, which is due to the low critical point and high thermophysical properties of CO_2 [9].

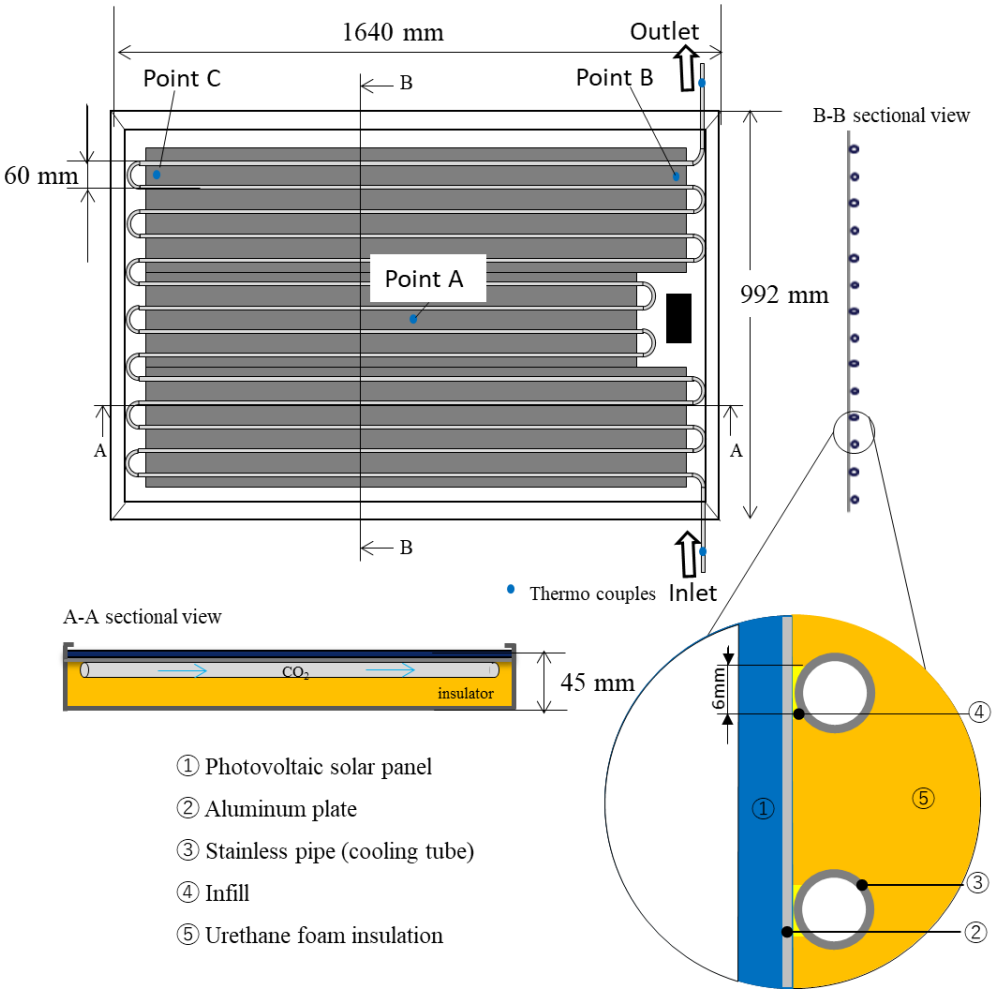

Figure 5.2. Detail view of CO_2-based photovoltaic-thermal hybrid system and sections.

To confirm the performance of CO_2 hybrid system in SRCS in power generation compared with an ordinary photovoltaic solar panel, the numerical analysis of temperature distribution on the surface of the hybrid system is further investigated in this study, in which the numerical analysis is compared with the experimental result for representative winter and summer conditions on the referenced point of the thermocouples installed in the hybrid system (Figure 5.2).

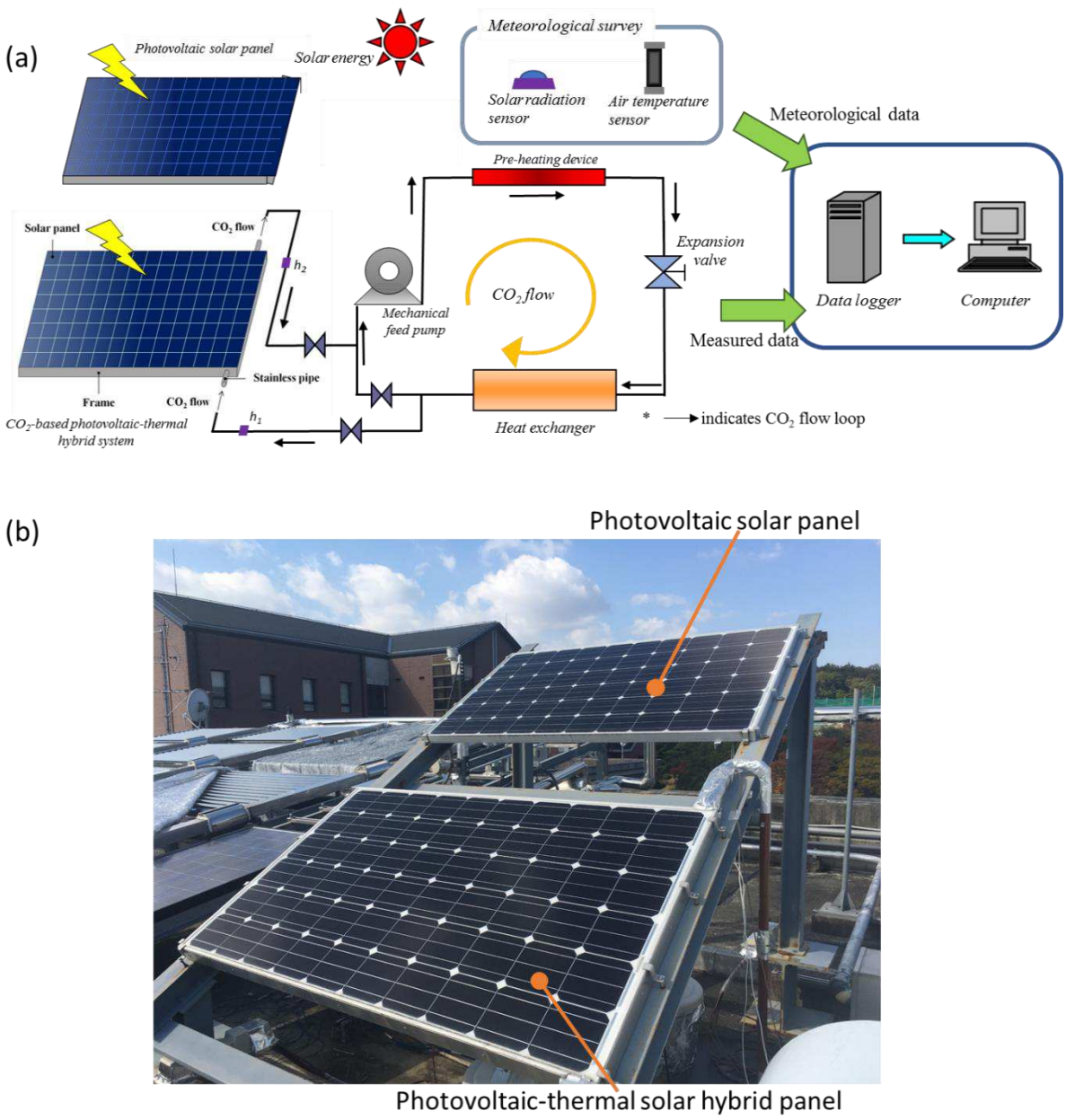

Figure 5.3. Photovoltaic solar panel and the hybrid system: (a) schematic diagram of the experimental apparatus and (b) its outlook.

5.1 System Configuration

5.1.1 CO_2-based photovoltaic-thermal hybrid system

The photovoltaic solar panel (commercially available ordinary product) model PS260M-20/U from K·I·S Co., Ltd is selected to use in this present study. The size of the photovoltaic solar panel is equal to 1640 mm × 992 mm, and its specific details are shown in Table 5.1. The aluminum plate mounted with the stainless pipe is installed on the back side of the photovoltaic solar panel for heat conduction from the surface of the panel to CO_2 flow. The detailed assembly diagram of the hybrid system is depicted in Figure 5.2. The urethane foam layer is used as the adiabatic insulator and is installed on the backside of the hybrid system. Also, the aluminum plate with stainless pipes is installed for heat absorption from the surface of the plate to CO_2 flow. The tube-plate connected area and inter-tube gap are 6 mm and 60 mm, respectively. Measurement and data processing devices are installed to achieve in-time data measurement, acquisition, and process. Three K-type thermocouples are placed at

various points on the backside of the hybrid system to detect the change of temperature of the panel. Furthermore, two thermocouples are installed to measure the temperature at the inlet and outlet of the CO_2 cooling tube. The accuracy of these thermocouples can be expressed as ±0.5 %. Moreover, the meteorological data of solar radiation and ambient temperature values for the field test are obtained from meteorological measuring device installed as depicted in Figure 5.3 (a), and the outlook of the system is shown in Figure 5.3 (b).

The hybrid system is placed facing the south with a setting angle of 30 ° to the horizontal line and installed on a roof-top of a testing facility. A reference photovoltaic solar panel of the identical product (the commercial photovoltaic panel) is also installed for the sake of comparison. To verify the practical potential of the system, the field test was conducted under real weather conditions as stated before. All signal data obtained from measurement devices are processed and recorded with instantaneous data acquisition system. The system performance obtained in the present field test may show different values when compared with the standard (laboratory controlled) test [10].

Table 5.1. Details of the photovoltaic solar panel

Model	**PS260M-20/U**
Maximum power (P_{max})	**260 W**
Conversion efficiency	**15.98 %**
Temperature-dependent coefficient	**-0.43 %/K**

※Standard Test Condition (STC)
Irradiance 1.0 kW/m^2, AM1.5, module temperature 25 ℃

5.1.2 Experimental Apparatus

The schematic of the experimental setup is as depicted and explained in detail in Figure 5.3. A total amount of 10 kg of CO_2 is contained in the system. In order to prevent the external factors affecting the standalone test for the hybrid system, such as weather or ambient temperature and to unify the thermodynamic conditions in the experiment, a heating module (preheating device) with 800 W input power is used to heat CO_2 in the system, instead of the evacuated solar collector unit for the total system performance evaluation (Figure 5.3 (a)). Moreover, in this study, the actual turbine is replaced by an expansion valve for the sake of unifying an operating condition in the Rankine cycle, while testing the hybrid system alone. The prototype of the hybrid system was tested for each day in the actual climate conditions in Kyoto region (34°47'58.1"N 135°46'04.6"E), namely, with typical winter and summer weather conditions.

To examine the physical insight taking place in the hybrid system, a numerical work is also conducted in the present study. The calculation domain of the numerical analysis of temperature distribution of the aluminum plate, on which the solar panel is installed (bonded) in the hybrid system, is depicted in Figure 5.4 (a) with the actual dimension of the plate; 992 mm, 1640 mm, and 40 mm with respect to x, y, and z-axis.

The sub-domain of the cooling tube mounted at the bottom of the aluminum plate, which is used in the numerical calculation, is displayed in Figure 5.4 (b), where the tube length is divided into n = 22,000, $dx = L/n$, where L is the tube length and d is the diameter.

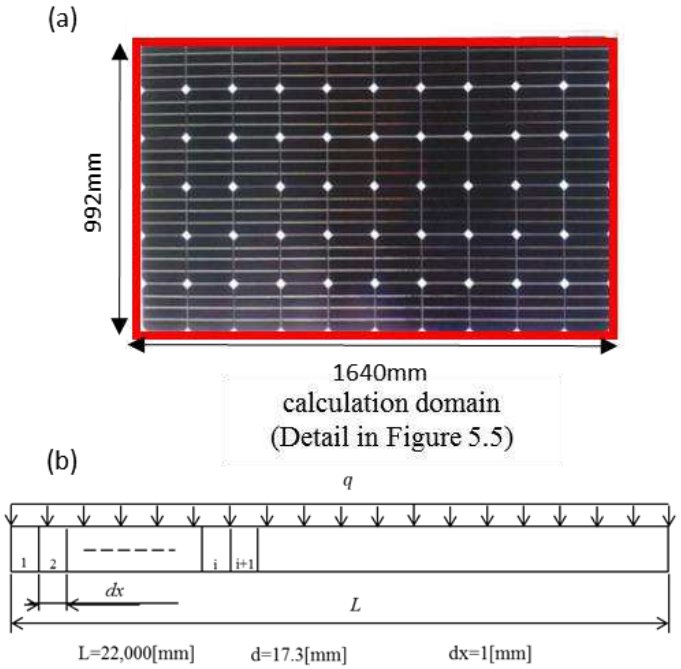

Figure 5.4. The numerical domain of temperature distribution (a) panel surface and (b) flow passage model of cooling tube.

5.2 Experimental Evaluation

Experiments are conducted in order to examine the performance of the hybrid system and to compare with the reference (ordinary) photovoltaic solar panel. The detailed experimental method will be described as follows. The results will be discussed and concluded in the next following sections.

The electric power generation (W_s) and its efficiency (η_s) can be calculated by equations (5.1) and (5.2), respectively [11],

$$W_s = \int_t w_s dt \tag{5.1}$$

and

$$\eta_s = \frac{\int_t w_s dt}{\int_t AI dt} \tag{5.2}$$

where w_s is instantaneous power generation. A is heat collection area, which equals to 1.63 m^2 and I is the amount of solar radiation per unit area obtained from real-time solar radiation sensor (shown in Figure 5.3 (a)), of which the accuracy is ±0.3 %.

The thermal energy gained from the hybrid system can be calculated by using enthalpy differences ($h_1 - h_2$) between inlet and outlet regions of CO_2 respectively, as shown in equation (5.3) [12],

$$Q_{in} = \int_t G\left(h_1 - h_2\right) dt \tag{5.3}$$

where G is average mass flow rate circulating in CO_2 Rankine cycle, and G is measured by a Coriolis mass flow meter, which provides a measurement range of 0.0015 to 0.0666 kg/min with the accuracy

of ±0.1 % as shown in Figure 5.3. In order to conduct an experiment under realistic field conditions of winter and summer time, G is fixed as reference values of 0.00375 kg/s and 0.00545 kg/s, respectively obtained from an actual test operation of SRCS. All necessary CO_2 thermophysical properties are obtained at any cycle points from a Program Package for Thermophysical Properties of Fluids database (PROPATH), which is a function type computer package for thermophysical properties [13].

5.3 Numerical Evaluation

The numerical analysis for examining the temperature distribution of the hybrid system is performed along the one-dimensional cooling tube passage (as illustrated in Figure 5.4 (b)) under constant heat flux input conditions. As the experimental cooling tube passage is covered with an insulator, ambient temperature is not considered in the calculation model of the passage. The governing equations (5.4) ~ (5.6), which are respectively mass conservation, momentum conservation, and energy conservation equation for CO_2 flow are the following [14]:

$$\frac{d(\rho u)}{dx} = 0 \tag{5.4}$$

$$\frac{d(\rho uu)}{dx} + \frac{dP}{dx} = 0 \tag{5.5}$$

$$\frac{d}{dx}\left(u\left(\rho\left(e+\frac{1}{2}u^2\right)+P\right)\right) = \frac{d}{dx}\left(\lambda\frac{dT}{dx}\right)+q \tag{5.6}$$

where u is velocity, P is pressure, ρ is density, T is the temperature of the CO_2 flow, q is heat flux input, and e and λ are internal energy and thermal conductivity, respectively. It is noted that the coordinate x appeared in equations (5.4) ~ (5.5) is the (one-dimensional) axial direction of the cooling tube.

The pressure is determined from the thermodynamic state equation (for CO_2) as,

$$P = \rho RTZ \tag{5.7}$$

where Z is the compression factor, which is given by density ρ, gas constant R, CO_2 temperature T, the critical density ρ_c = 468.0 kg/m^3 and critical temperature T_c = 304.1 K with the following equation [15],

$$Z = 1+\frac{\rho}{\rho_c}\sum_{i=1}^{6}\sum_{j=1}^{9}a_{i,j}\left(\frac{\rho}{\rho_c}-1\right)^i\left(\frac{T_c}{T}-1\right)^j \tag{5.8}$$

The internal energy e and thermal conductivity λ can be calculated as,

$$e = \left(h_T^{id}-h_0^{id}\right)+\int_0^{\rho}\frac{1}{\rho^2}\left[P-T\left(\frac{\partial P}{\partial T}\right)_{\rho}\right]d\rho - RT + \Delta h_0 \tag{5.9}$$

and

$$\lambda = \lambda_T \exp\left[\sum_{i=1}^{5}\sum_{j=0}^{2}b_{i,j}\left(\frac{T}{T_c}\right)^j\left(\frac{\rho}{\rho_c}\right)^i\right] \tag{5.10}$$

In the one-dimensional calculation for the temperature distribution in the cooling tube passage, a forward finite difference method is used to solve the model equations (5.4) ~ (5.6). As depicted in Figure 5.4 (b), a total length of the flow passage L (= 22,000 mm) is divided into segment length dx of 1 mm. In the calculation, the passage diameter d is fixed at 17.3 mm. The left and right points are specified as inlet and outlet, respectively. The thermophysical properties can be calculated in each segment length dx by a forward finite difference method. The inlet conditions of temperature, pressure, and mass flow are set as the same as experimental conditions in the referenced winter and summer weathers. The numerical calculation continues until the updated values of temperature and pressure become small ($\approx 1.0 \times 10^{-5}$) to judge the convergence, satisfying the conservation of total amount of heat flux input.

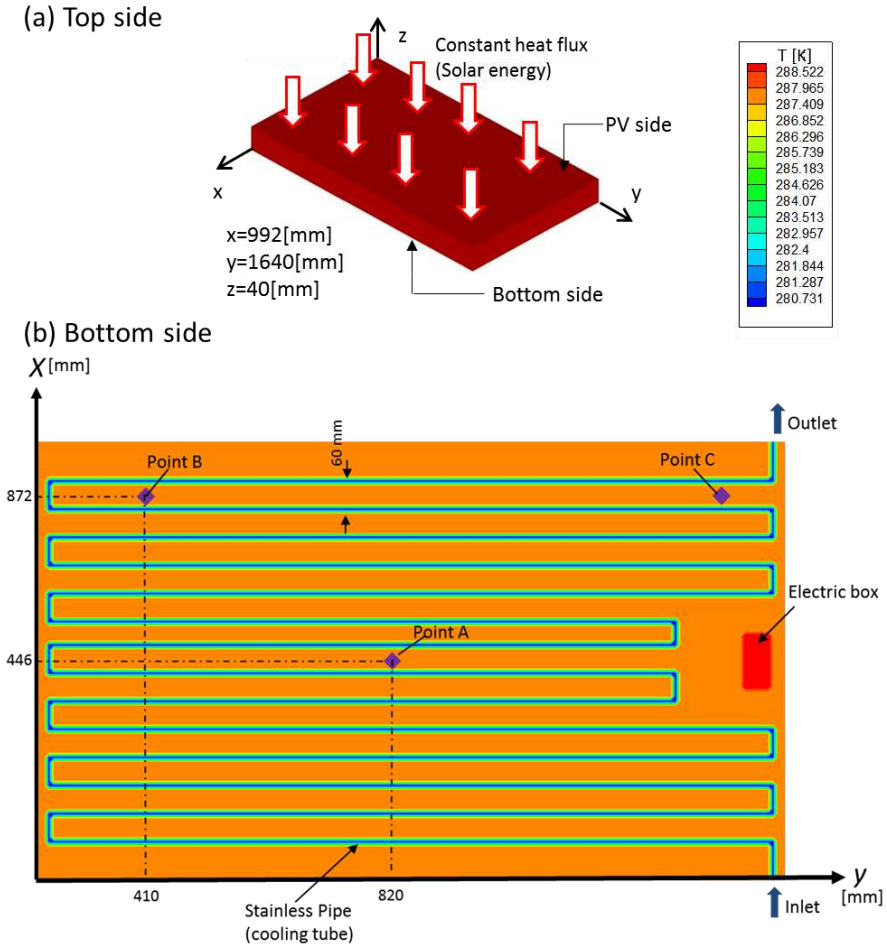

Figure 5.5. Three-dimensional calculation domain (a) plate surface and (b) cooling tube arrangement.

To investigate the temperature distribution of the hybrid system, a three-dimensional thermal conduction model is numerically solved, taking into account the thickness of the aluminum plate. The three-dimensional thermal conduction model is depicted in Figure 5.5 (a).

The three-dimensional thermal conduction equation (5.11) [16], which implies the aluminum plate with a thickness of 40 mm, as displayed in Figure 5.4 (a), is solved with the initial condition of temperature T as 310.0 K (excluding bonded area).

$$\frac{\partial T}{\partial t} = \alpha_{s,a}\left(\frac{\partial^2 T}{\partial x^2} + \frac{\partial^2 T}{\partial y^2} + \frac{\partial^2 T}{\partial z^2}\right) \tag{5.11}$$

The boundary condition on the topside is a constant heat flux condition (the solar radiation heat flux), while the four sides (edges) have the adiabatic condition. At the bottom, the stainless pipes and

cooling tube (Figure 5.4 (b)) are mounted as depicted in Figure 5.5 (b). At the boundary condition of the bottom side, the numerical calculation is coupled with the cooling tube temperature calculated by one-dimensional calculation and the other area is kept at the adiabatic condition.

The piping of CO_2 passage (as depicted in Figure 5.4 (b)) on the backside surface of the aluminum plate is arranged with 60 mm pitch length and 1.73 mm of piping diameter, where the liquid CO_2 undergoes temperature change with continuous properties variation (one-dimension distribution).

It is noted here that the three-dimensional coordinate system *x*-*y*-*z* as indicated in Figure 5.5 (a) is conveniently adopted in solving equation (5.11). The results of the numerical solution of equation (5.11) are later presented in Figure 5.12 as the *x*-*y* plane at the surface of a photovoltaic solar panel (Figure 5.5 (b)).

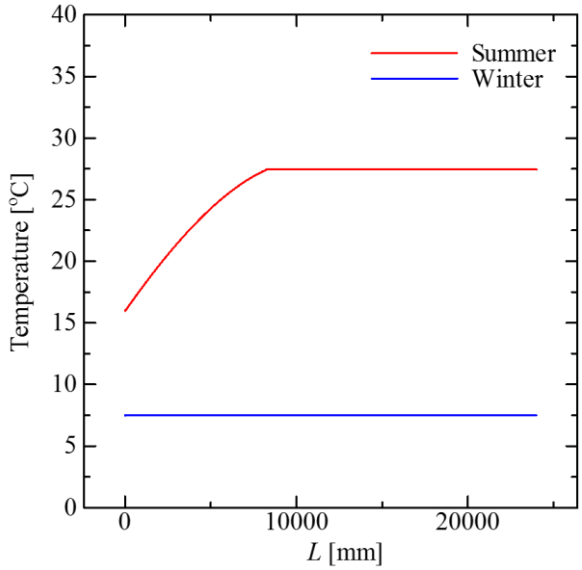

Figure 5.6. Calculation results of temperature in the cooling tube in winter and summer weather conditions.

The temperature distribution along the cooling tube length obtained by the numerical calculation based on equation (5.4) ~ (5.6) in winter and summer conditions are depicted in Figure 5.6. Temperature is calculated based on the CO_2 database PROPATH [13]. In the summer condition, the inlet temperature (L = 0 mm), which is obtained from the experiment condition is set at 16 °C, and it is found that liquid CO_2 temperature increases along the cooling tube length, but after CO_2 reaching 28 °C (L = 8,230 mm), CO_2 temperature becomes almost constant at approximately 28 °C, which is caused by heating up to the phase change of CO_2 (at saturation temperature). However, in the winter condition, when the inlet CO_2 temperature is set at 7.5 °C, it is found that the difference between inlet and outlet becomes minimal as depicted in Figure 5.6.

5.4 Results and discussions

Based on the fact that the operation of the hybrid system is strongly dependent on the time variation of solar radiation and the surrounding ambient air temperature. In order to obtain typical representative data for testing the effectiveness of the hybrid system, reference solar radiation and surrounding air temperature were recorded in winter (4th January 2015) and summer (18th August 2015) weather conditions in Kyotanabe area, Japan, which are shown in Figure 5.7 (a) and (b), respectively. It can be seen obviously that in the winter data, from 8:00 to 12:30 hour, the solar radiation gradually increases and vice versa from 12:30 to 17:00 hour. While in the summer data, the time of solar radiation was taken longer due to the difference of sunrise and sunset time in each weather condition. In the summer data, the recorded hour increases from 6:00 to 13:00 hour and vice versa from 13:00 to 18:00 hour. The average radiation energy in winter is lower than in the summer

condition, which is obtained from the measurement device directly and can be represented as 0.124 kW/m^2 and 0.746 kW/m^2, respectively. The average ambient air temperature was found at 5 °C and 25 °C in the winter and summer conditions, respectively.

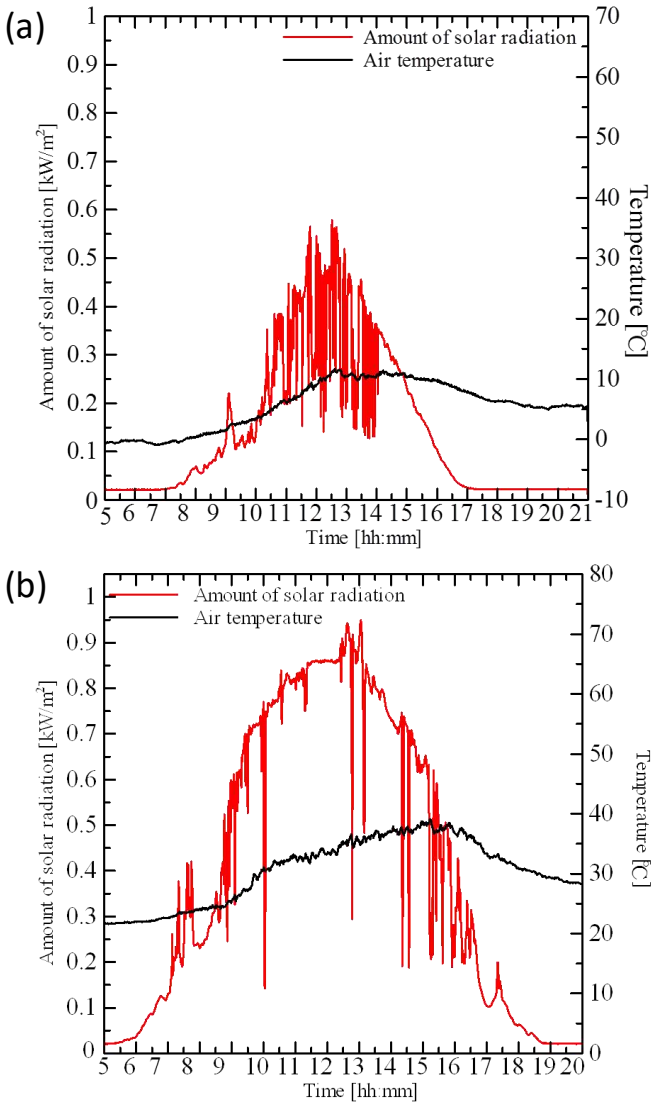

Figure 5.7. Solar radiation and ambient air temperature in (a) winter; January 4, 2015, and (b) summer; August 18, 2015.

From the measured meteorological data in Figure 5.7 (a) and (b), the power generation efficiency and photovoltaic solar panel temperature obtained from the hybrid system and reference (ordinary) photovoltaic solar panel are obtained and compared in Figure 5.8 (a) and (b) in case of the reference winter and summer conditions, respectively. The power generation efficiency is calculated, based on the heat collection data from the experiment and temperature from installed thermocouples by equations (5.1) ~ (5.3).

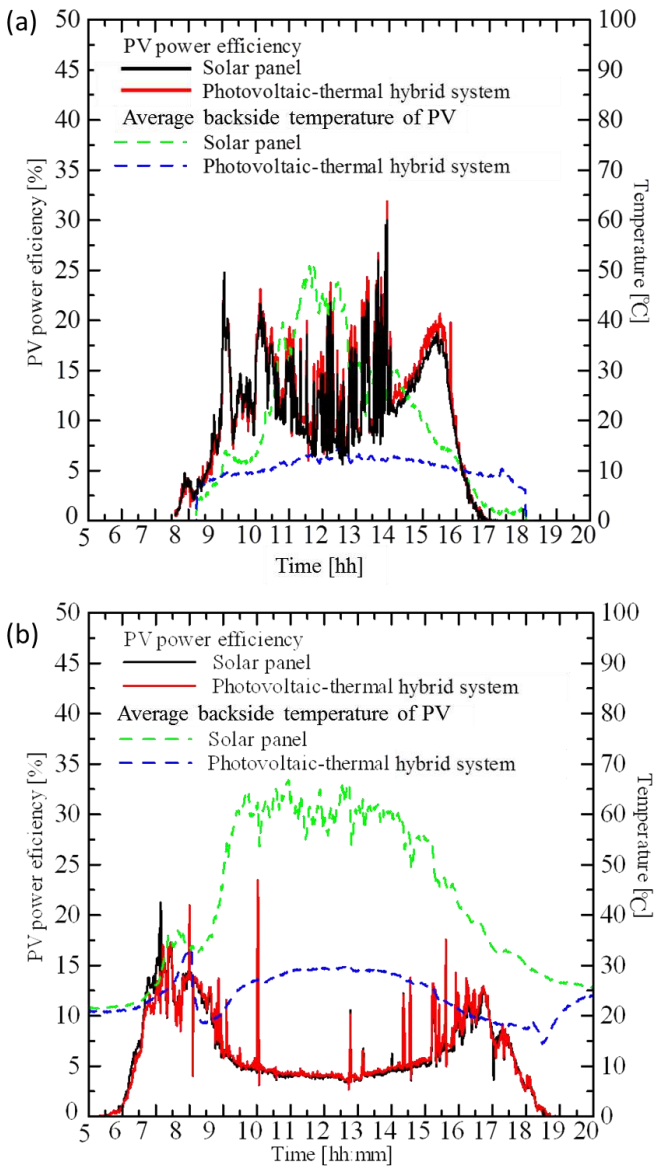

Figure 5.8. Electric power generation efficiency and backside temperature of the CO_2-based photovoltaic-thermal hybrid system compared with the ordinary photovoltaic solar panel in (a) winter and (b) summer.

The operation time was approximately 8:00 to 17:00 hour in winter and 6:00 to 18:00 hour in summer. In Figure 5.8 (a), the winter condition, it was observed that the time-averaged efficiency of electric power generation is approximately 13.8 % in the hybrid system, while the ordinary photovoltaic solar panel shows 12.9 %. In case of the summer condition, on the other hand, the time-averaged efficiency of power generation from both the hybrid system and the ordinary photovoltaic solar panel were found to be lower than that compared with winter condition, where the time-averaged power generation are found at 6.58 % and 6.31 % in the hybrid system and ordinary photovoltaic solar panel, respectively. The relative comparison between winter and summer is highly dependent on the difference of an ambient condition (mostly surrounding air temperature, i.e., the higher air temperature causes, the lower heat transfer effect) for cooling. However, it can be observed that the hybrid system gives higher value on power generation than the ordinary one in both weather conditions, in which the highest value of instantaneous power conversion efficiency increase can be found as much as 2 % in the winter condition [17]. This data (the increasing efficiency) is particularly highlighted in Figure 5.9 (a) from 10:00 to 14:00 hour (taken from Figure 5.8 (a), winter condition). It can be found that the power generation efficiency of the hybrid system is higher than the photovoltaic solar panel in the operation hours. To confirm the value of efficiency increase in electric power generation in the winter

condition and for the sake of clarity, the time average value per 30 minutes is plotted in Figure 5.9 (b). It is seen that a 2 % increase in electric power generation efficiency is evident.

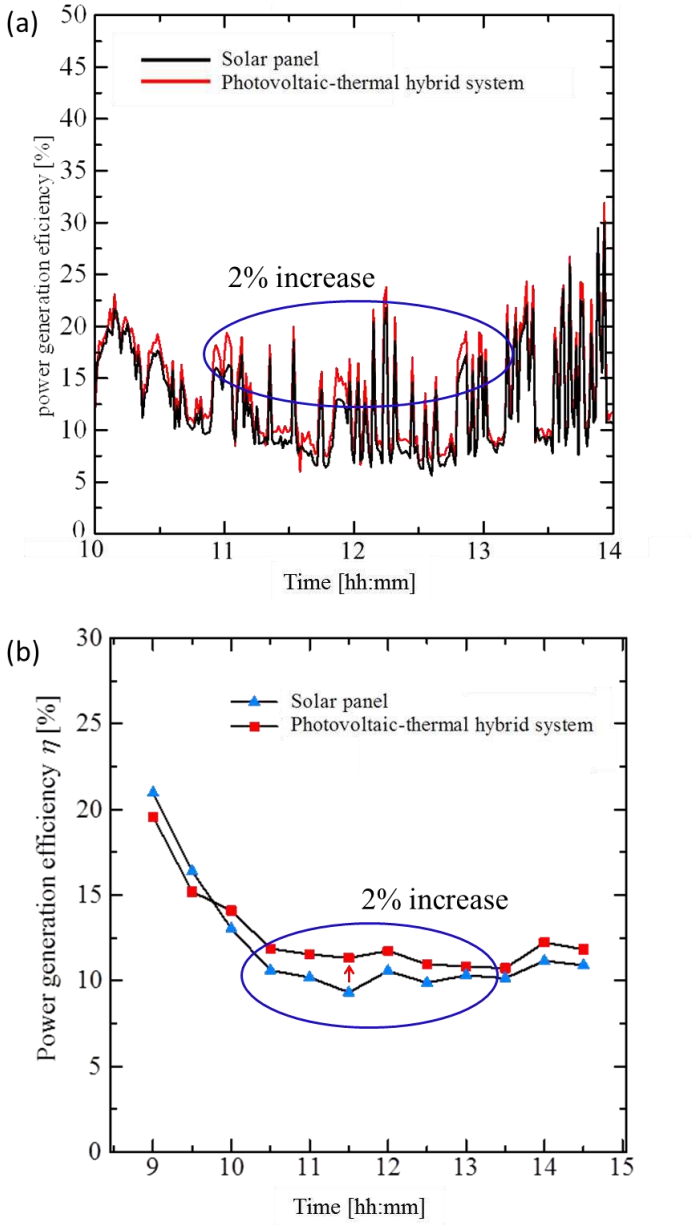

Figure 5.9. Electric power conversion efficiency increasing in winter condition on (a) instantaneous result and (b) time-average result.

In order to verify the temperature reduction in the photovoltaic solar panel by the CO_2 flow, the photovoltaic solar panel temperature (backside temperature) of the hybrid system and the conventional photovoltaic solar panel are also compared in Figure 5.8 (a) and (b) for winter and summer conditions, respectively. It was found that the substantial reduction of cell temperature in the hybrid system was possible resulting in increasing the efficiency of electric power generation, as mentioned above in Figure 5.9 (b), for which the maximum temperature reduction of 35 °C was recorded in the winter condition.

Another purpose of the hybrid system is to increase the performance of SRCS by pre-heating CO_2 before entering the evacuated solar collector as indicated in Figure 5.1. The temperature at the inlet and outlet of the hybrid system was examined in winter and summer conditions from 8:00 to 17:00 hour, which is similarly shown in Figure 5.10. It can be confirmed that the temperature of CO_2 is

increased by the hybrid system as the maximum value of 28 °C in the summer condition, while the only slight increase was observed as shown in the winter condition. The main reason for different results in weather conditions comes from the effect of ambient air temperature on the CO_2 properties in the system. The ambient air temperature in summer is much higher than in winter, where CO_2 is effectively heated in the summer condition with higher solar radiation.

The above results show that the hybrid system, when it is coupled with SRCS, can boost the thermal energy of CO_2 in the evacuated solar collector and resultantly can increase the electric power generation, raising the total efficiency of SRCS [18]. The advantage of installing the hybrid system can be thus understood, from the results of Figure 5.8, 5.9 and 5.10, that in the winter operation the photovoltaic solar panel efficiency in the hybrid system can become higher, and in the summer operation (when it is coupled with SRCS) SRCS thermal efficiency (including power output from turbine generation) becomes higher.

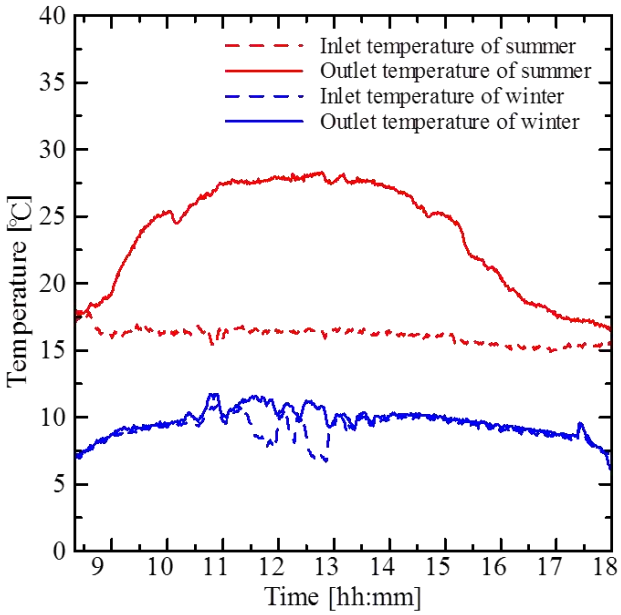

Figure 5.10. The CO_2 temperature at the inlet and outlet points of the CO_2-based photovoltaic-thermal hybrid system in winter and summer weather conditions.

In Figure 5.11 (a) and (b), experimental results of the surface temperature distribution of the backside of the hybrid system at the operation time of 8:00 to 18:00 hours in winter and summer conditions are respectively displayed with the resultant temperature at three different positions of thermocouples installed (positions of thermocouples are referred to Figure 5.2) together with CO_2 inlet and outlet temperatures. In the winter condition, Figure 5.11 (a), Point A (which is at the middle of the panel) indicates the lowest temperature while Point C (near the outlet point) indicates the highest temperature at all experiment condition. The highest temperature can be found at Point C (12:00 to 12:30). However, at some period of operation (11:00 to 14:00), the temperature has some degree of fluctuation in all measurement points, which may be due to the uncontrolled weather change as shown in Figure 5.7 (a).

In summer condition, as illustrated in Figure 5.11 (b), similar to the operation in winter condition, temperature at Point A is found lower than Point B and C, while the highest temperature was found at Point C. However, at the startup condition (8:00 to 10:00), the Point B is found to be higher than Point C. The reason of these unusual surface temperature distributions in the hybrid system are the transient process of the CO_2 in the system, due to the property change in liquid to gaseous phase. Furthermore, compared with the winter condition, the temperature variation is slightly smoother in all operation condition due to the smooth change of the solar radiation in the reference summer condition.

In order to verify the surface temperature (photovoltaic solar panel temperature) distribution of the hybrid system, the numerical evaluation is conducted, and the results are depicted in Figure 5.12 (a) and (b) for the winter and summer conditions, respectively. It should be mentioned here that for the sake of qualitative argument between the numerical verification and the experimental data, temperatures at some representative points (Point A, B, and C) in Figure 5.11 (a) and (b) are mainly considered in the following discussion.

The area (Figure 5.5 (a)) for the surface temperature distribution in winter and summer weather conditions are selected from the experimental set-up to be utilized in the numerical calculation. To represent the conditions in numerical analysis, the initial conditions in winter is set as 30 °C and 0.4 kW/m^2 of surface temperature and solar radiation, respectively, while the condition in summer is set as 60 °C and 0.8 kW/m^2, respectively.

For the present numerical work, to conduct a realistic numerical simulation, the mass flow rate of liquid CO_2 is quoted from the SRCS (as depicted in Figure 5.1) data [19], for some similar representative winter and summer weather conditions, where SRCS were kept at optimum operating condition at the evacuated solar collector condition of 10 MPa and 200 °C.

The temperature distribution of CO_2 along the cooling tube (as depicted in Figure 5.6 for the winter and summer conditions) is used to calculate the temperature distribution on the photovoltaic solar panel in winter and summer conditions. The results of the numerical calculation are illustrated in Figure 5.12 (a) and (b), respectively for the winter and summer conditions. It is mentioned that the strong heat transmission from the electric box (Figure 5.5) experienced from experiments is also taken into account in numerical calculations.

As seen (obtain from representative climate conditions) in Figure 5.12 (a) winter and (b) summer condition, the photovoltaic solar panel mounted on the surface of the hybrid system is cooled in such a way that along the cooling tube the whole panel area is reasonably well cooled, showing the greenish color distribution in major panel area. As the temperature rises from the inlet toward the outlet direction, the whole panel area is heated by heat conduction from the photovoltaic solar panel due to solar radiation (regarded as the constant heat flux input at the photovoltaic solar panel). As seen in Figure 5.12 (a) and (b) due to the cooling tube arrangement, the panel plate is effectively cooled from the solar radiation heat input, absorbing heat by passing cold CO_2 fluid. Notably, in Figure 5.12 (a) (the winter condition) the photovoltaic solar panel is almost evenly cooled along the cooling tube. While in Figure 5.12 (b) (summer condition), slightly un-evenly cooled area on photovoltaic solar panel surface appears toward the outlet cooling tube area, where 1 to 2 degree (K) un-even temperature distribution is observed. The unevenness of the summarized condition is relatively strong. This is due to heated up liquid CO_2 at the entrance of the hybrid system. Moreover, as liquid CO_2 is heated up to the state of phase-change (liquid-gas phase change), the temperature of the cooling pipe reaches almost plateau (as demonstrated in Figure 5.6, summer condition), keeping the temperature at constant after approximately L = 8,230 mm. This implies that almost ¼ of the total photovoltaic solar panel can be kept at evenly cooled state as verified in Figure 5.12 (b).

The results obtained from the numerical analysis (Figure 5.12 (a) and (b)) indicate the effectiveness of the CO_2 cooling for the hybrid system. It is mentioned that the reddish color zone shows higher temperature zone (where the two major hot zones appeared in Figure 5.12 (a) and (b) in the vicinity to the inlet and outlet region of the cooling tube) is the heat accumulated area due to the adiabatic condition. The electric box also causes reasonably high temperature area, which is inevitable in both (a) winter and (b) summer conditions.

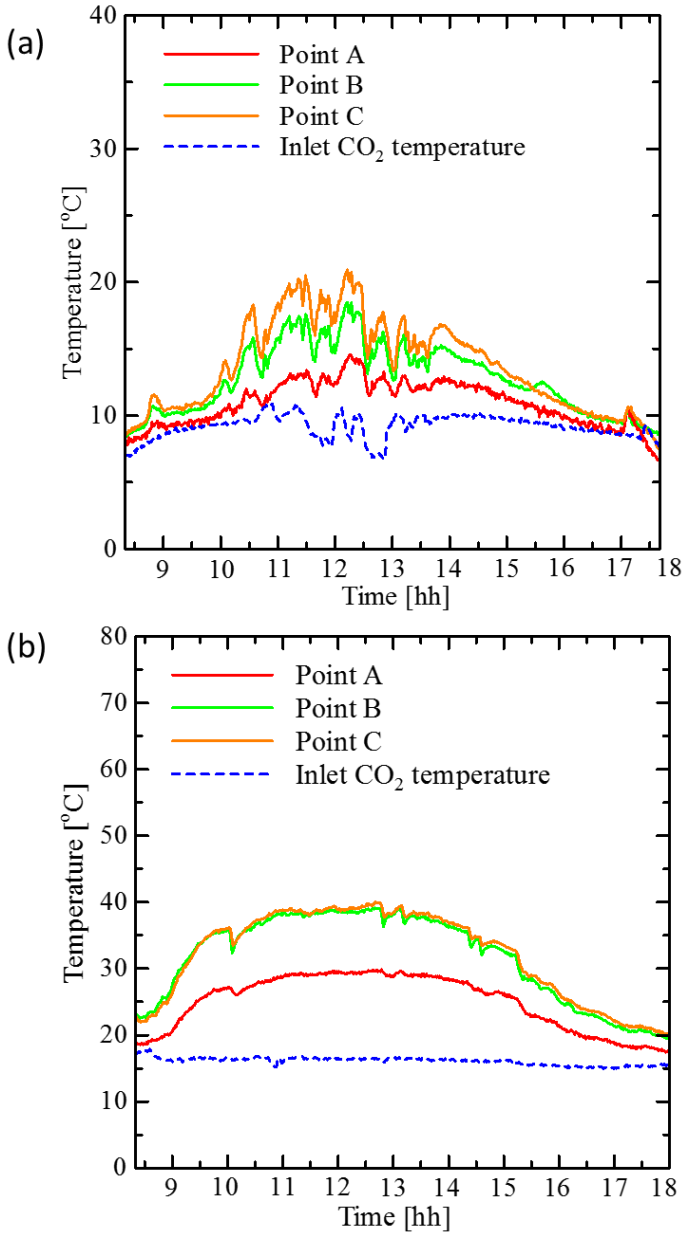

Figure 5.11. Experimental results of temperature distribution in (a) winter and (b) summer.

Three representative points are used to compare the analytical results and experimental results (Figure 5.11). In the summer condition, as shown in Figure 5.12 (b), the trend of strong temperature distribution is apparently visible. It can be seen that the temperature of the inlet region is higher than the outlet region (deep blue to light blue color). This also implies similar temperature distribution on the panel area which was observed at the representative points (Point A, Point B, and Point C) in the experiment (Figure 5.11 (b)). For the winter condition, as seen in Figure 5.12 (a), the photovoltaic solar panel temperature shows almost perfect evenness of the temperature distribution on the panel as described before, which also implies that similar trend for Point A, B, and C as observed in Figure 5.11 (a).

For the winter condition, as seen in Figure 5.12 (a), the photovoltaic solar panel temperature shows almost perfect evenness of the temperature distribution on the panel as described before, which also implies the similar trend for point A, B and C as observed in Figure 5.11 (a). The evenness of temperature distribution in the winter condition helps to improve the efficiency of electric power generation of the photovoltaic solar panel, as verified experimentally as 2 % higher than the ordinary photovoltaic solar panel in Figure 5.9 (a) and (b).

The numerical analysis evaluated in Figure 5.12 (a) and (b) depicts the fact that the temperature distribution in the photovoltaic solar panel may be depending upon the conditions of solar irradiation (together with the ambient condition) as well as the flow condition of liquid CO_2, entering to the hybrid system. The results obtained in Figure 5.12 gives a good indication of the trend for the temperature distribution of the whole photovoltaic solar panel in the hybrid system as displayed in Figure 5.11 [20].

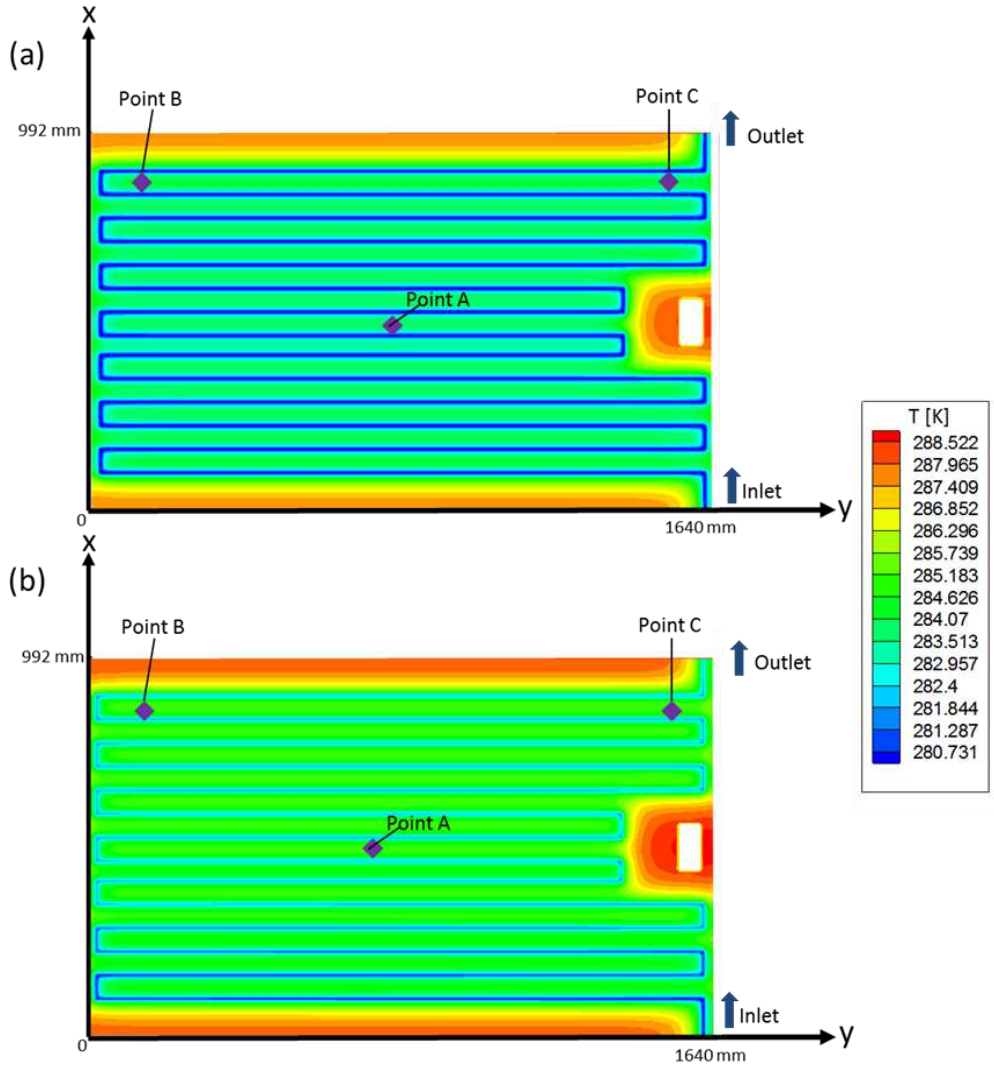

Figure 5.12. Analytical results of the temperature distribution of photovoltaic solar panel surface in (a) winter and (b) summer.

In this study, the 2 % increase of electric power generation efficiency of the hybrid system is found compared with the ordinary photovoltaic solar panel, suggesting an advantage of adopting the hybrid system in the economy. It can be estimated that 2 % increasing of electric power generation efficiency gives nearly 20 % effectiveness on the capital per kWh of power generation in the massive scale of installation [21]. The other advantages of the hybrid system such as thermal recovery, pollution reduction and payback of investment also benefit, compared with the ordinary photovoltaic solar panel.

5.5 Conclusions

The CO_2-based photovoltaic-thermal hybrid system is performed in the present study in application to the supercritical CO_2 solar Rankine cycle system. From the results of the experimental and numerical calculation, it is revealed that;

(i) From the experimental results, the efficiency of the system in winter is higher than in summer due to the effects of ambient air temperature and CO_2 properties in the system.

(ii) By using the hybrid system, the maximum increase in power generation efficiency is observed as 2 % in a field test, where the photovoltaic solar panel temperature is cooled by a maximum 35 °C in winter.

(iii) As to the increase in the performance of SRCS with the hybrid system, the experimental result showed a substantial increase in the temperature of the CO_2 between the inlet and outlet of the system. The maximum increase of 28 °C in summer followed by the phase change of CO_2.

(iv) The analytical results verified the temperature distribution from the experiments that the temperature at the near outlet region of the panel is higher than the near inlet region of the panel. However, the trend of temperature distribution in winter and summer conditions are entirely different, which may depend on the climate condition and CO_2 flow in the system.

References

[1] Huang, B. J., Lin, T. H., Hung, W. C., and Sun, F. S., 2001. Performance evaluation of solar photovoltaic/thermal systems. *Solar energy*, *70*(5), pp.443-448.

[2] Dubey, S., Sandhu, G. S., and Tiwari, G. N., 2009. Analytical expression for electrical efficiency of PV/T hybrid air collector. *Applied Energy*, *86*(5), pp.697-705.

[3] Chow, T. T., He, W., Ji, J., and Chan, A. L. S., 2007. Performance evaluation of photovoltaic–thermosyphon system for subtropical climate application. *Solar energy*, *81*(1), pp.123-130.

[4] Zhang, X. R., Yamaguchi, H., Fujima, K., Enomoto, M., and Sawada, N., 2005. A feasibility study of CO_2-based Rankine cycle powered by solar energy. *JSME International Journal Series B Fluids and Thermal Engineering*, *48*(3), pp.540-547.

[5] Yamaguchi, H., Zhang, X. R., Fujima, K., Enomoto, M., and Sawada, N., 2006. Solar energy powered Rankine cycle using supercritical CO_2. *Applied Thermal Engineering*, *26*(17-18), pp.2345-2354.

[6] Micheau, Patrick., 1991. Process and device for regulating a flow of liquid CO_2, and application thereof in a cooling tunnel." U.S. Patent No. 5,040,374.

[7] Chow, T. T., 2010. A review on photovoltaic/thermal hybrid solar technology. *Applied energy*, *87*(2), pp.365-379.

[8] Joshi, A. S., and Tiwari, A., 2007. Energy and exergy efficiencies of a hybrid photovoltaic–thermal (PV/T) air collector. *Renewable Energy*, *32*(13), pp.2223-2241.

[9] Bottinga, Yan, and P. Richet., 1981. High pressure and temperature equation of state and calculation of the thermodynamic properties of gaseous carbon dioxide. *American Journal of Science*, *281*(5), pp.615-660.

[10] Nishioka, K., Hatayama, T., Uraoka, Y., Fuyuki, T., Hagihara, R., and Watanabe, M., 2003. Field-test analysis of PV system output characteristics focusing on module temperature. *Solar Energy Materials and Solar Cells*, *75*(3-4), pp.665-671.

[11] Grätzel, M., 2004. Conversion of sunlight to electric power by nanocrystalline dye-sensitized solar cells. *Journal of Photochemistry and Photobiology A: Chemistry*, *164*(1-3), pp.3-14.

[12] Niu, X. D., Yamaguchi, H., Iwamoto, Y., and Zhang, X. R., 2013. Optimal arrangement of the solar collectors of a supercritical CO_2-based solar Rankine cycle system. *Applied Thermal Engineering*, *50*(1), pp.505-510.

[13] PROPATH Group, 1997. PROPATH: a program package for thermophysical properties.

[14] Yamaguchi, H., 2008. *Engineering fluid mechanics* (Vol. 85). Springer Science & Business Media.

[15] Angus, S., Armstrong, B. and De Reuck, K.M., 1976. Carbon Dioxide: International Thermodynamic Tables of the Fluid State-3. *Carbon Dioxide: International Thermodynamic Table of the Fluid State*.
[16] Çengel, Y.A. and Ghajar, A.J., 2011, *Heat and Mass Transfer Fundamentals & Applications*. McGraw-Hill, New York.
[17] Yamaguchi, H., Maki, T., Pumaneratkul, C., Yamasaki, H., Iwamoto, Y., and Arakawa, J., 2017. Experimental Study on the Performance of CO_2-Based Photovoltaic-thermal Hybrid System. *Energy Procedia*, *105*, pp.939-945.
[18] Kosmadakis, G., Manolakos, D., and Papadakis, G., 2011. Simulation and economic analysis of a CPV/thermal system coupled with an organic Rankine cycle for increased power generation. *Solar Energy*, *85*(2), pp.308-324.
[19] Zhang, X.R. and Yamaguchi, H., 2008, An experimental study on evacuated tube solar collector using supercritical CO_2. *Applied Thermal Engineering*, 28(10), pp.1225-1233.
[20] Pumaneratkul, C., Yamasaki, H., Yamaguchi, H. and Iwamoto, Y., 2018. Evaluation on the Performance of Photovoltaic–Thermal Hybrid System Using CO_2 as a Working Fluid. *Journal of Solar Energy Engineering*, *140*(4), p.041011.
[21] Kalogirou, S. A., and Tripanagnostopoulos, Y., 2006. Hybrid PV/T solar systems for domestic hot water and electricity production. *Energy conversion and management*, *47*(18-19), pp.3368-3382.

Chapter 6

Development of supercritical CO_2 Rankine cycle system with low-temperature geothermal energy using heat pipe technology

Geothermal energy was used for electric power generation more than hundred years ago in many countries. The geothermal energy production has been the most considerable growth in recent years, especially in the countries located on the "Ring of Fire" [1]. However, in the typical geothermal power plant, the only high-temperature geothermal reservoir is suitable to use for commercial production, where hot water or steam, which temperature is higher than 220 °C, is pumped up from the underground reservoir to drive a turbine for electric power generation on the ground [2]. It is usually practiced that, after the process of the geothermal power plant, cooled water will be injected back to absorb heat from the reservoir for the next power generation process. It can be obviously seen that the high rate of energy is required to drive the geothermal fluid in the power plant process. Another factor to consider is the utilization of low-temperature geothermal reservoir for electric power generation. Commonly, hot water from the low-temperature geothermal reservoir, which is lower than 100°C, is mainly used for the hot-spring resource as the primary purpose of tourism. Though, in recent years, the low-temperature reservoir has been paid much attention as an energy generation resource for the purpose of increasing demand for geothermal energy potential [3].

Due to the limitation of the low-temperature geothermal reservoir to generate electric energy, the secondary cycle system is used to transform heat energy from the geothermal reservoir into work for electric power generation [4~5]. In the present study, the supercritical CO_2 Rankine cycle system, which was introduced in Chapter 3 is used as the secondary cycle (power generation cycle) [6]. The heat pipe (thermosyphon) was originally adapted preliminary as heat absorption equipment from the low-temperature geothermal reservoir, in which only thermal energy is absorbed from the underground geothermal heat source, showing no additional energy required for pumping water to the surface and the ground as for the conventional geothermal power plant. Another advantage is the fewer impacts on the environmental aspect. Since the purposed system (supercritical CO_2 Rankine cycle system with geothermal heat pipe) does not use hot water itself (spa), that uses only thermal energy from the geothermal heat source, it must be sustainable than conventional geothermal energy generation, which is often discussed but rarely understood yet [7].

This chapter mainly presents some details of a heat pipe, using the principle of thermo-siphon in exacting the geothermal heat energy, where methanol is utilized as a working fluid to absorb heat energy ranging from 80 °C to 100 °C reservoir. The performance of the Rankine cycle (system) with the heat pipe is discussed on the basis of a supercritical CO_2 Rankine cycle system [8]. Furthermore, in order to confirm the principle of the low-temperature geothermal heat pipe, the experiment apparatus of heat pipe has been constructed and discussed later in this chapter.

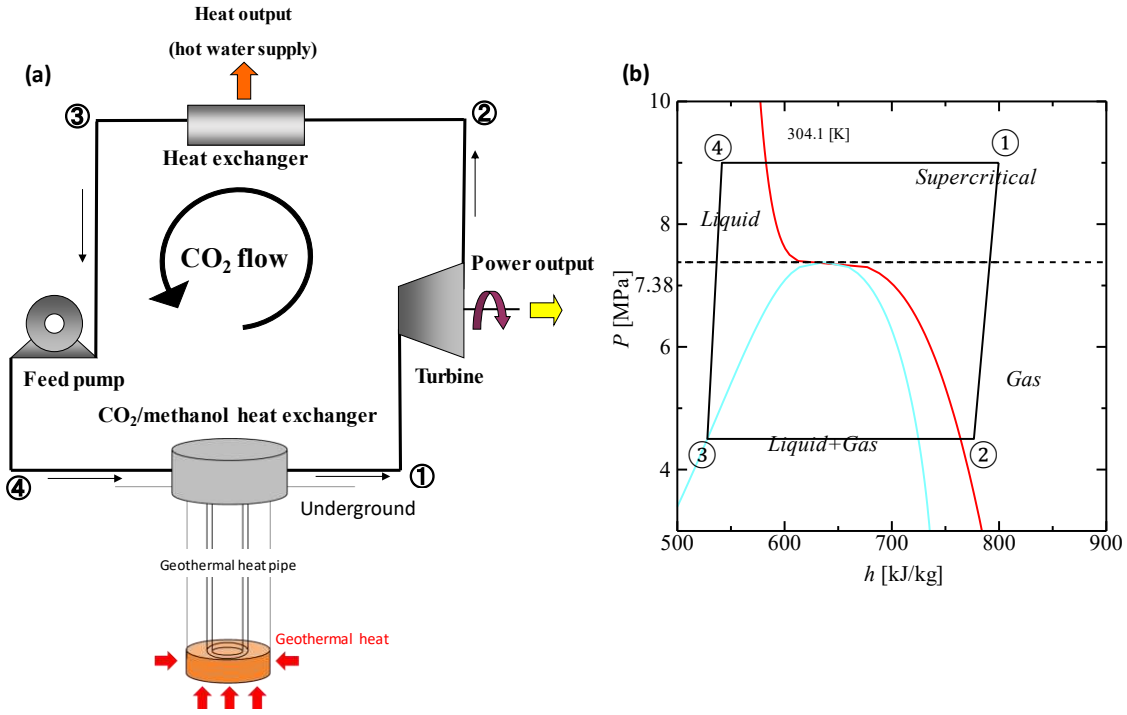

Figure 6.1. (a) Schematic diagram of supercritical CO_2 Rankine cycle with a geothermal heat pipe and (b) *P-h* diagram

6.1 Supercritical CO_2 Rankine cycle system with geothermal heat pipe

6.1.1 Rankine cycle with geothermal heat pipe

The Rankine cycle with geothermal heat pipe consists of main four components, as shown in Figure 6.1 (a) and (b) for the schematic diagram and *P-h* diagram, respectively. The CO_2/methanol heat exchanger with geothermal heat pipe, using methanol as working fluid, is installed at the high pressure side of Rankine cycle, ④ → ①, to absorb the heat from underground, in which CO_2 is heated by geothermal heat underground, and turns to a supercritical state. The expanded supercritical CO_2 drives a turbine and generate electric energy, ① → ②. After leaving the turbine, due to the remaining thermal energy, CO_2 is passed through the heat exchanger units, ② → ③ and heat energy are supplied to appliances on hot water supply. Lastly, mechanical feed pump feeds CO_2 back to a CO_2/methanol heat exchanger with the high pressure state, ③ → ①, and the cycle recommences. It can be seen that in the cycle process of the Rankine cycle with geothermal heat pipe both electric and heat energies are generated with high efficiency and environmentally friendly manner, because of unique properties of supercritical CO_2. It is mentioned here that the geothermal energy can be supplied for 24 hours, which makes much more sustainable compared with other renewable energy sources, and also the system increases the sustainable potential for low-temperature geothermal utilization.

6.1.2 Low-temperature geothermal heat pipe

The annulus pipe with a basin at the bottom end is designed as a heat exchanger from the low-temperature geothermal reservoir, as shown in Figure 6.2 (a). The heat pipe is assumed to be installed in the firmly shallow underground at approximately 300 m of depth with the estimated temperature being approximately 90 °C, which exists in many specific places, such as hot-spring (spa) resources in Japan [9]. As shown in Figure 6.2 (a), the insulation layer is installed between two pipes for the purpose of preventing heat transfer between the inner and outer tube, also at the outer tube to prevent the heat

from the ground (rock layer). Methanol is selected to use as a working fluid in the geothermal heat pipe, because of its low boiling point (64.7 °C) and high heat transfer properties.

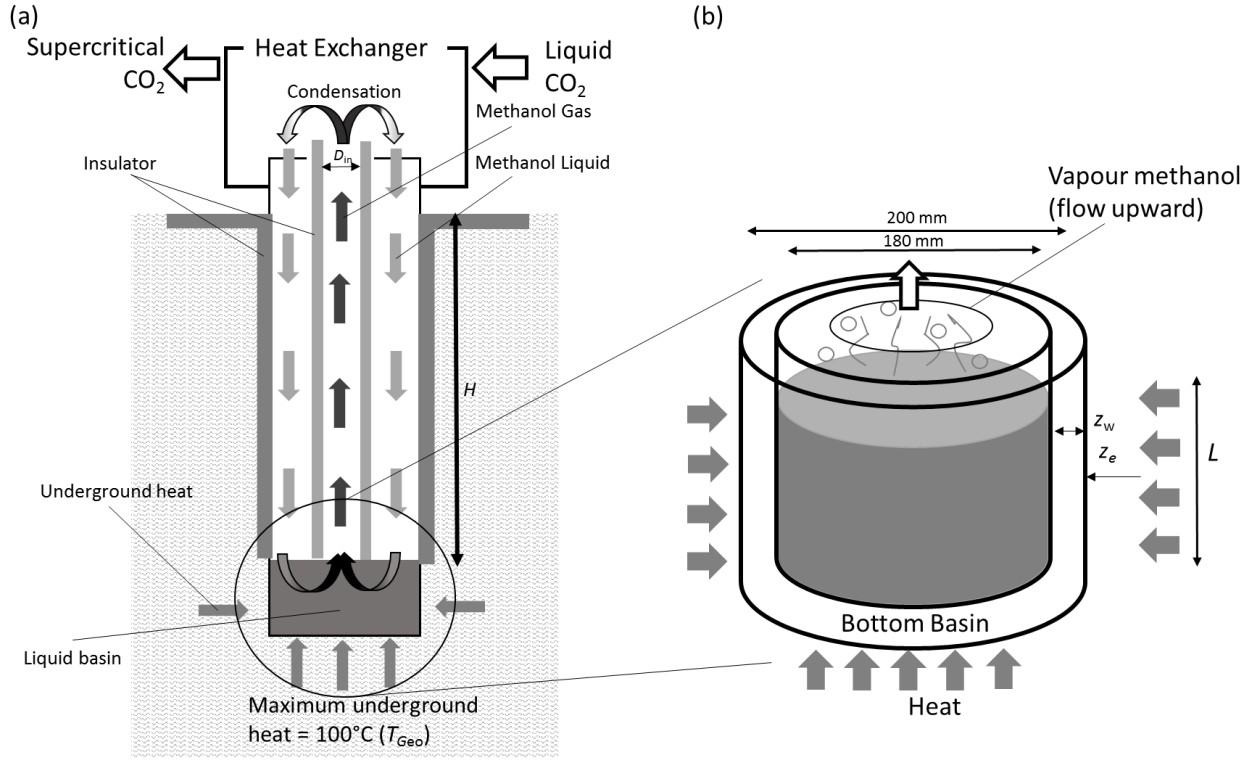

Figure 6.2. Schematic diagram of (a) low-temperature geothermal heat pipe and (b) detail view of a bottom basin.

The liquid methanol is contained in the bottom basin at the end of the pipe (Figure 6.2 (b)). While the methanol absorbs thermal energy from the geothermal reservoir, methanol changes the phase from a liquid state to gas state, and the gaseous phase flows up to the heat exchanger at the top of the heat pipe. At the top of the heat pipe, high-temperature gas methanol flows through the CO_2/methanol heat exchanger, where CO_2 is heated and turns into a supercritical state, and which is utilized for generating electric energy excess and heat (as hot water) supplying in Rankine cycle. After methanol transfers, thermal energy to CO_2, methanol gas is condensed and turns into a liquid state, and the liquids methanol flows to the bottom basin along the outer passage by the gravitation force to absorb the geothermal heat for the next cycle.

6.2 Analytical model of the system

The thermodynamical analysis is performed by enthalpy and energy transfer in and out to the Rankine cycle, using the *P-h* diagram as the power cycle chart, where the numbers in Figure 6.1 (b) are comespending to the schematic in Figure 6.1 (a). The flow rate of working fluid CO_2 ($\dot{m}_{CO_2}$) in the system is set at 0.842 kg/s, by assuming the electric power generation (Q_T) from the turbine is 20 kW while the heat energy (Q_{HX}) supplied from heat exchanger unit equals to 189 kW. The value of 0.9 is used for the efficiency of the turbine and heat exchanger unit [10]. The electric power generation can be estimated from the following equation. All thermodynamic properties of CO_2 are obtained from PROPATH [11].

$$Q_T = \dot{m}_{CO_2}(h_1 - h_2) \tag{6.1}$$

moreover, heat recovery from the heat exchanger unit can be found as,

$$Q_{\mathrm{HX}} = \dot{m}_{\mathrm{CO_2}}(h_2 - h_3) \tag{6.2}$$

where h is enthalpy of the CO_2 at any point in Figure 6.1.

Total heat power input in the Rankine cycle (Q_{Rankine}) can be obtained from heat power absorbed from underground geothermal energy by the heat pipe using methanol (Q_{heatpipe}), as shown follows

$$Q_{\mathrm{Rankine}} = 0.9 Q_{\mathrm{heatpipe}} \tag{6.3}$$

where equation (6.3) is equivalent to

$$\dot{m}_{\mathrm{CO_2}}(h_1 - h_4) = 0.9\dot{m}_{\mathrm{methanol}} c_{\mathrm{p}}(T_{\mathrm{in}} - T_{\mathrm{out}}) \tag{6.4}$$

in equation (6.4), $\dot{m}_{methanol}$ and c_{p} are flow rate and heat capacity of methanol in the heat pipe, respectively, while T_{in} and T_{out} refer to the temperature of methanol at inlet and outlet points of the CO_2/methanol heat exchanger, respectively. The properties of methanol are obtained from Engineering Sciences Data Unit [12].

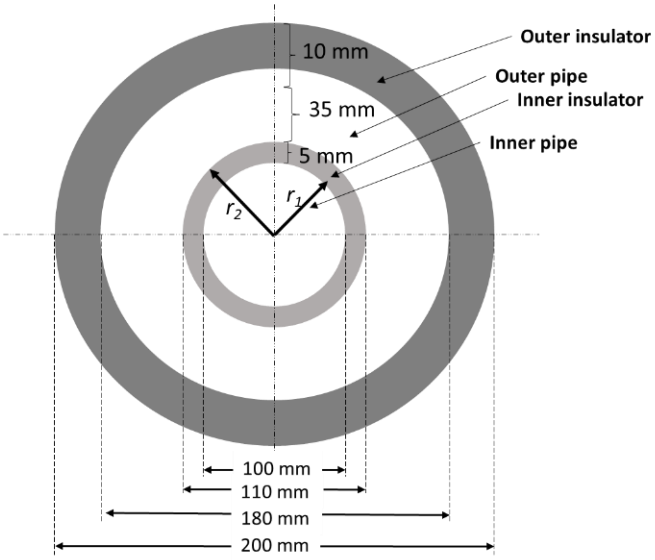

Figure 6.3. Cross section of the geothermal heat pipe.

As mentioned earlier, the design of geothermal heat pipe is based on the low-temperature geothermal reservoir, which exists in many specific places, such as in Japan. For a practical 20 kW system, it is assumed from an engineering point of view that the 200 mm of outer diameter pipe is designed with a depth of 300 m, the temperature at the bottom hole is approximately at 90 °C. Also, due to the limitation of construction in primary design, the diameter of the methanol basin is fixed as the 200 mm [13]. The gas flow pathway (inner pipe) with the diameter equals to 100 mm, while the thickness of inner and outer insulation layers is designed optimally as 5 mm and 10 mm, respectively. The whole structure of geothermal heat-pipe is considered to be made from chromium for the purpose of preventing metal corrosion from methanol. The selective low thermal conductivity polystyrene is chosen to be used as insulation material as shown in Figure 6.2 [8]. The cross-section of the geothermal heat pipe is shown in Figure 6.3 as well as the detail of methanol basin at the bottom of the pipe in Figure 6.4.

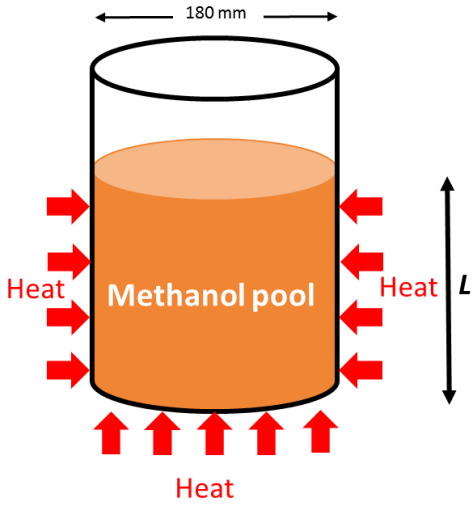

Figure 6.4. Detail of methanol basin at the bottom end of the heat pipe

The acceptable rate of heat loss (q/L) from the outer passage to inner passage per unit length of methanol flow in the heat pipe is set as less than 100 W/m (it can be found as 60 W/m in this design), which can be calculated from equation (6.5) [14],

$$\frac{q}{L} = 2\pi k \left(\frac{T_i - T_o}{\ln\left(r_2 / r_1\right)} \right) \tag{6.5}$$

where k is thermal conductivity of polystyrene, L is the total length of heat pipe T_i and T_o are the temperature at an inner and outer tube of the heat pipe, respectively, and r_1 and r_2 are respectively radius inner pipe and insulation layer (Figure 6.3).

The observed temperature can calculate the underground temperature at any depth along the length of the geothermal heat pipe T_G at the upper top and bottom end pipe using the linear interpolation of the geothermal gradient as shown below [15].

$$T_G(z) = \frac{T_E - T_A}{L} Z + T_A \tag{6.6}$$

where T_E and T_A are the temperatures at the bottom end pipe and upper air atmosphere, which are set as 100 °C and 25 °C, respectively.

The pressure at the bottom basin of the tube P_p, with a condition of the vertical heat pipe and due to the hydrostatic head can be found as [16]

$$P_p = P_v + \rho g L \sin\theta \tag{6.7}$$

It is noted that the change of methanol height level L in the bottom basin as the result of boiling has an insignificant effect on the pressure. P_v is the vapor pressure of methanol, ρ is the density of methanol (Figure 6.4).

In this study, the temperature in the heating of liquid basin of methanol by the geothermal energy is set at temperature approximately 90 °C (T_s) while the saturation temperature of methanol (at surface of methanol in basin) is found as 67.8 °C (T_{sat}), in which the excess temperature is assumed as relatively low (lower than 30 °C). Thus, in the analysis, the nucleate boiling takes place in the basin [14]. The Rohsenow relationship in the nucleate pool boiling is used to calculate heat flux ($\dot{q}_{\text{nucleatetion}}$)

as

$$\dot{q}_{\text{nucleate}} = \mu_{\text{l}} h_{\text{fg}} \left[\frac{g\left(\rho_{\text{l}} - \rho_{\text{v}}\right)}{\sigma} \right]^{1/2} \times \left[\frac{c_{\text{pl}}\left(T_{\text{s}} - T_{\text{sat}}\right)}{C_{\text{sf}} h_{\text{fg}} \, \text{Pr}_{\text{l}}^{\text{n}}} \right]^{3} \tag{6.8}$$

where h_{fg} is enthalpy of vaporization of methanol, μ_{l} is the dynamic viscosity of liquid methanol, C_{sf} is coefficient of fluid-surface combinations (Ethyl alcohol-chromium), σ is surface tension of liquid-vapor interface and Pr_{l} is Prandtl number of liquid methanol.

The rate of heat transfer during the nucleate boiling $\dot{Q}_{\text{boiling}}$ can be determined as

$$\dot{Q}_{\text{boiling}} = A\dot{q}_{\text{nucleate}} \tag{6.9}$$

The surface heating areas A include the bottom and wall of the basin, which is

$$A = \pi r^2 + 2\pi rL \tag{6.10}$$

while the radius of basin r equals to 100 mm and L is the height level of methanol in the basin.

The model of the CO_2/methanol heat exchanger is used as this study has the thermal resistance as 0.0222 °C/W z_{HX}, while the thermal resistance of external surface z_{e} and the wall of the bottom basin z_{w} (at the heating area) are calculated based on reference [16].

Vapor temperature of methanol T_{v} and its velocity $\dot{V}$, which the flow property of methanol is assumed to be laminar flow for the estimation when flowing upward can be calculated as below.

$$T_v = T_4 + \frac{z_{HX}}{\sum z}\left(T_{Geo} - T_4\right) \tag{6.11}$$

$$\dot{V} = \frac{\left(\Delta P - \rho_v g H \sin\theta\right)\pi {D_{in}}^4}{128\mu_v H} \tag{6.12}$$

where the properties of vapor methanol at any temperature can be obtained from the database [12]. In equations (6.11) and (6.12), T_4 refers to the point of temperature in Figure 6.1, and T_{Geo} is temperature of surrounded rock at bottom basin (90 °C), ρ_{v} and μ_{v} are density and dynamic viscosity of vapour methanol, respectively, H is the height of flow pathway of vapour methanol in heat pipe (250 m), θ is tilt angle of heat pipe (vertical in this study), D_{in} is the diameter of the inner pipe (vapour methanol flow pathway), and ΔP is the pressure difference between at vapour methanol in bottom basin and methanol/CO_2 heat exchanger at the surface, which is assumed to be at 1atm of pressure at the surface.

The methanol mass flow rate ($\dot{m}_{methanol}$) (which is a high factor in considering the performance of the heat pipe as explained lately) through the heat exchanger at top end can be determined as

$$\dot{m}_{\text{methanol}} = \rho_v A\dot{V} \tag{6.13}$$

where A is an area of vapor methanol flow pathway.

The equations (6.1) to (6.4) refers to the system analysis of the Rankine cycle (the secondary cycle) for electric and thermal energy generation and supply. The geothermal energy absorption system with a CO_2/methanol heat exchanger is investigated by understanding the characteristic of heat transfer

and driving force in the heat pipe (for the low-temperature geothermal reservoir) within equations (6.5) to (6.10). Furthermore, equations (6.11) to (6.13) show the methanol gas flow rate in the heat pipe.

The results (of low-temperature geothermal heat pipe) are verified in the next section, where the temperature gradient and depth of methanol basin are discussed in order to avoid the too-high rate of heat transfer and mass flow rate, which depends on the safety factor of heat pipe design.

6.3 Results and discussions for the system analytical

The representative resultant Rankine cycle with geothermal heat pipe obtained from this operation are displayed in Figure 6.1 (b). It can be seen from the analysis of the *P-h* diagram that the cycle can achieve the transcritical cycle throughout the operating condition. From the process ④ to ① where CO_2 is found to be changed to the supercritical state for power generation in the turbine.

Figure 6.5 shows a change of temperature along the depth in the heat pipe obtained from equation (6.6) with the polystyrene as an outer insulator with the initial temperature (at the upper surface) being estimated as 25 °C. The increasing of temperature is linear. The total length of the heat pipe is set as 300 m with the highest temperature of 100 °C

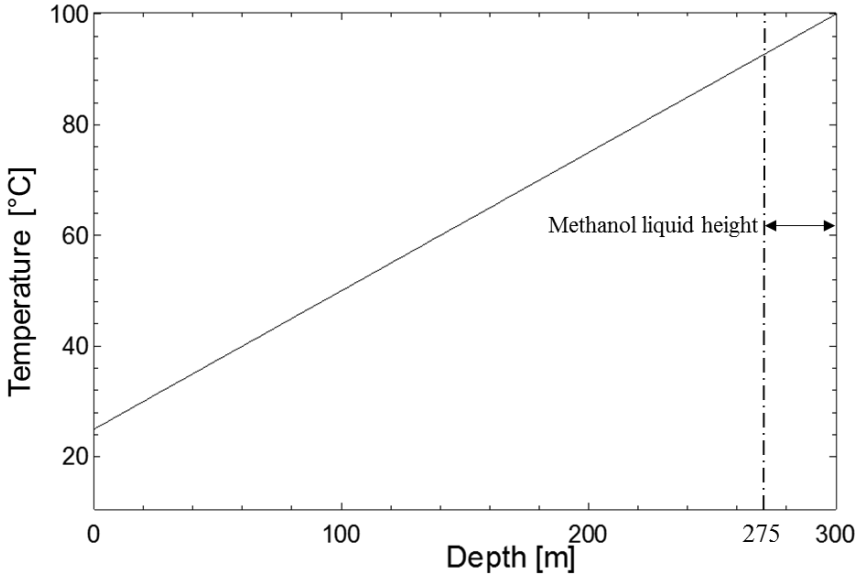

Figure 6.5. The change of temperature along the heat pipe with the depth of the geothermal reservoir.

In order to verify the performance of the heat pipe, the methanol liquid height from 0 m to 25 m at the bottom basin are investigated mainly to obtain the heat from the low-temperature geothermal reservoir (no outer insulator installed). The pressure at the bottom basin of the heat pipe at 5 m, 10 m, 15 m, 20 m and 25 m are calculated to simulate energy transfer from the basin to the top of the heat pipe, where the CO_2/methanol heat exchanger is situated, referring to Figure 6.5. The average temperature at the bottom and wall basin for pressure calculation in this analysis is assumed as 90 °C, which also use to obtain all properties of methanol. The pressure at bottom basin increases with the increase of high of methanol level in the basin as shown in Figure 6.6.

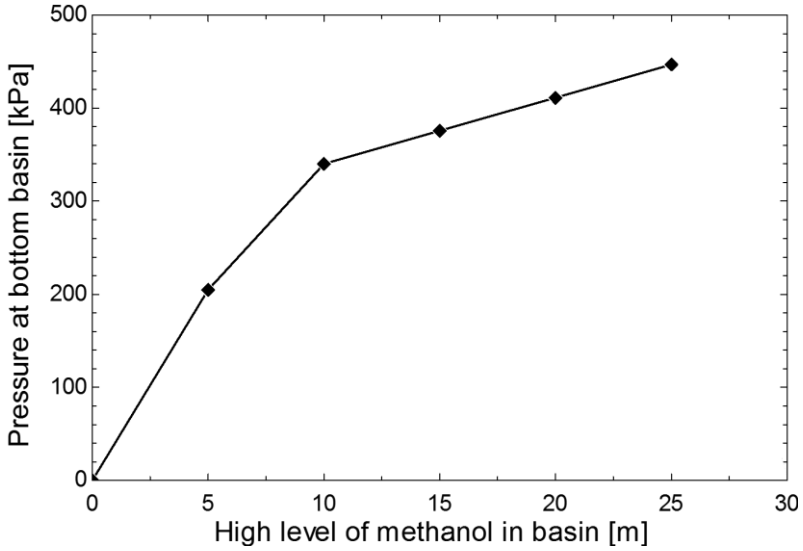

Figure 6.6. The pressure at the bottom basin (P_p) with the difference of methanol height level in heat pipe (L).

The resultant mass flow rate of vapor methanol and heat transfer rate in CO_2/methanol heat exchanger are displayed in Figure 6.7 and Figure 6.8, respectively. In Figure 6.7 and Figure 6.8, referring to the calculation result of the pressure distribution at each height level of liquid methanol as shown in Figure 6.6, the mass flow rate of methanol and the rate of heat transfer in the CO_2/methanol heat exchanger are substantially dependents on the height of methanol level in the basin. Where on first approximation the area at the bottom of the basin is only used (not including wall area), the mass flow rate of vapor methanol and the rate of heat transfer in CO_2/methanol heat exchanger are relatively low as 0.029 kg/s and 1.695 kW, respectively. However, in the case of the 5 m height of methanol in the basin, the results show that both rates are increased to 2.901 kg/s and 171.303 kW, respectively [17]. It can be determined that the heating area of the wall in the basin is a significant factor to achieve the use of the low-temperature geothermal reservoir by using the heat pipe.

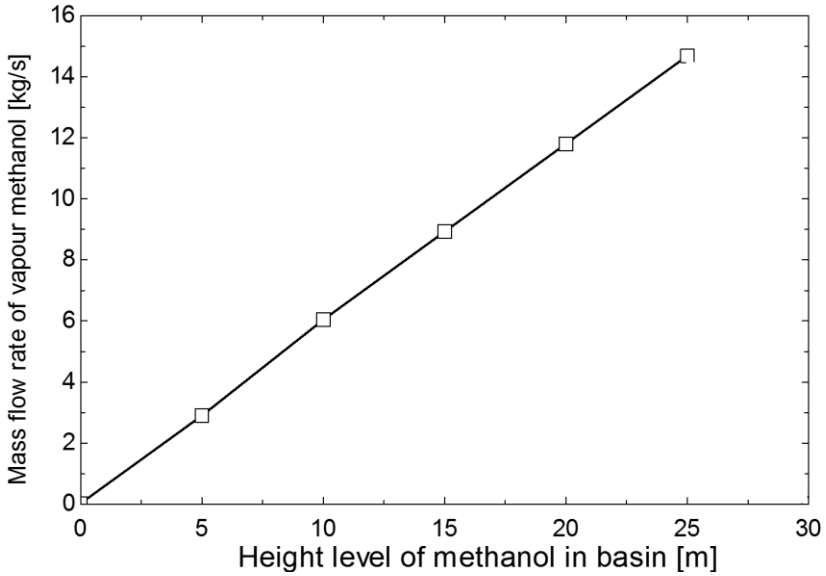

Figure 6.7. The flow rate of vapor methanol ($\dot{m}_{methanol}$) with the difference of methanol height level in the heat pipe (L).

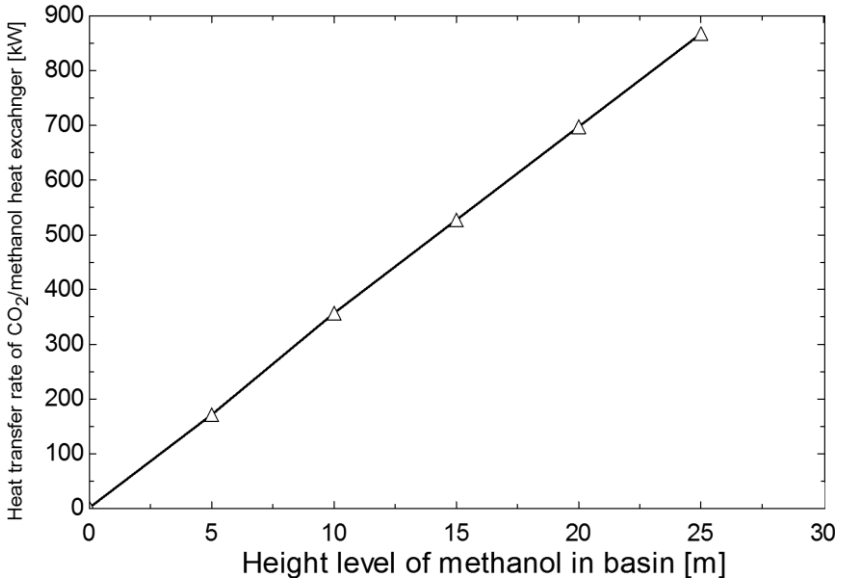

Figure 6.8. Heat transfer rate of the CO_2/methanol heat exchanger in heat pipe ($Q_{heatpipe}$) with the difference of methanol height level in heat pipe (L).

From the equations (6.3) and (6.4), it can be found that the rate of heat transfers required to change to the CO_2 liquid state to supercritical state in CO_2/methanol heat exchanger is approximately 224 kW. Where, if the height of methanol in the basin is around 7 m, the rate of heat transfer becomes higher than 224 kW (at 10 m of higher gives 357.196 kW in the same calculation). In this study, the highest value was found at 25 m of height, which gives 14.487 kg/s and 867.561 kW of the mass flow rate of methanol and the rate of heat transfer, respectively. Using the results obtained in Figure 6.7 and Figure 6.8, it can be speculated that the efficiency of heat absorption may be as higher as 80 %. It can be obviously seen from the analysis that it can ensure the feasibility of the system to utilize low-temperature geothermal reservoir.

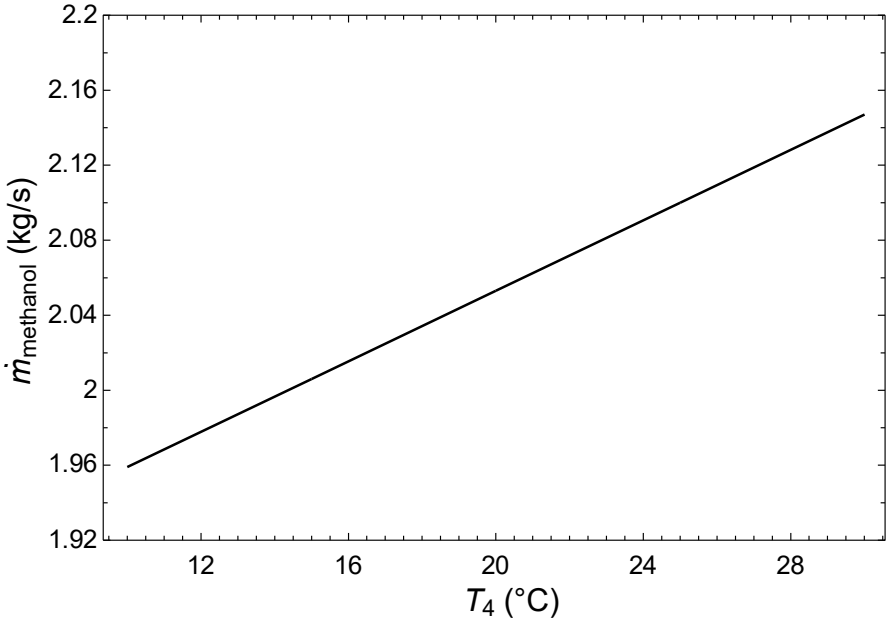

Figure 6.9. The flow rate of vapor methanol ($\dot{m}_{methanol}$) with a difference of the methanol/CO_2 heat exchanger inlet temperature (T_4).

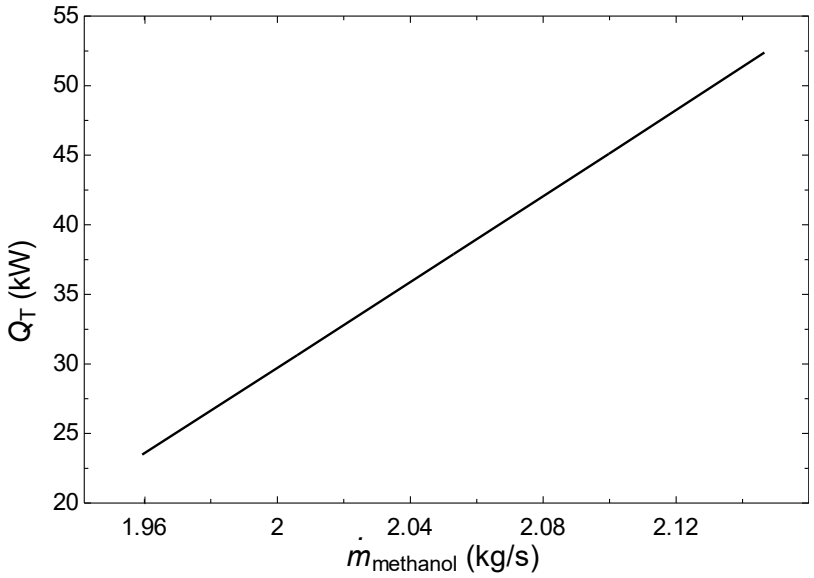

Figure 6.10. Electric power generation from the supercritical CO_2 turbine (Q_T) with a different flow rate of vapor methanol ($\dot{m}_{methanol}$).

In the theoretical calculation, the methanol/CO_2 heat exchanger inlet temperature (T_4) range of 10 °C to 30 °C with a pressure of 8 MPa are conveniently used to calculate the mass flow rate of methanol from the heat pipe. The result is shown in Figure 6.9, and it is found that that the methanol mass flow rate ($\dot{m}_{methanol}$) defined in equation (6.13) increases with increasing T_4 by the highest value is about 2.149 kg/s in case of T_4 = 30 °C. Regarding feasibility in energy generation from supercritical CO_2 Rankine cycle system with low-temperature geothermal heat pipe, the electric power generation is investigated from equation (6.4) with the difference methanol mass flow rate ($\dot{m}_{methanol}$). In Figure 6.10, the electric power generation increase along the methanol mass flow rate, which can be found as high as 52.38 kW with 2.149 kg/s of methanol mass flow rate.

The performance of supercritical CO_2 Rankine cycle system with low-temperature geothermal heat pipe is evaluated by investigating the variations of the CO_2 properties in the system loop, i.e., temperature and pressure at inlet and outlet of methanol/CO_2 heat exchanger and also at the turbine. Also, the mass flow rate of methanol in the heat pipe has a significant effect on the system efficiency as well.

The system efficiency is determined as that of the turbine in the system by ignoring the mechanical loos of the mechanical feed pump. The system thermal efficiency (η_{th}) and methanol/CO_2 heat exchanger efficiency (η_{HX}) are defined as

$$\eta_{th} = \frac{0.9\left(h_1 - h_2\right)}{h_1 - h_4} \tag{6.14}$$

$$\eta_{HX} = \frac{\dot{m}_{CO_2}\left(h_1 - h_4\right)}{0.6Q_{\text{heatpipe}}} \tag{6.15}$$

The system thermal efficiency of supercritical CO_2 Rankine cycle system with low-temperature geothermal heat pipe and methanol/CO_2 heat exchanger efficiency with outlet temperature T_4 (10 °C to 30 °C) of methanol/CO_2 heat exchanger at three difference pressure P_4 = 8, 9 and 10 MPa are shown in Figure 6.11 (a) and 6.11 (b), respectively. In Figure 6.11 (a), temperature T_4 has a significant effect on the thermal system efficiency which increases with temperature. In addition, the lower pressure gives higher in thermal efficiency as well (8 MPa in this study). The thermal efficiency indicates that the scale

of conversion in thermal energy input (from geothermal energy) into total work output (electric energy). In which supercritical CO_2 Rankine cycle system with low-temperature geothermal heat pipe η_{th} can achieve higher than 0.25 in case of P_4 = 8 MPa.

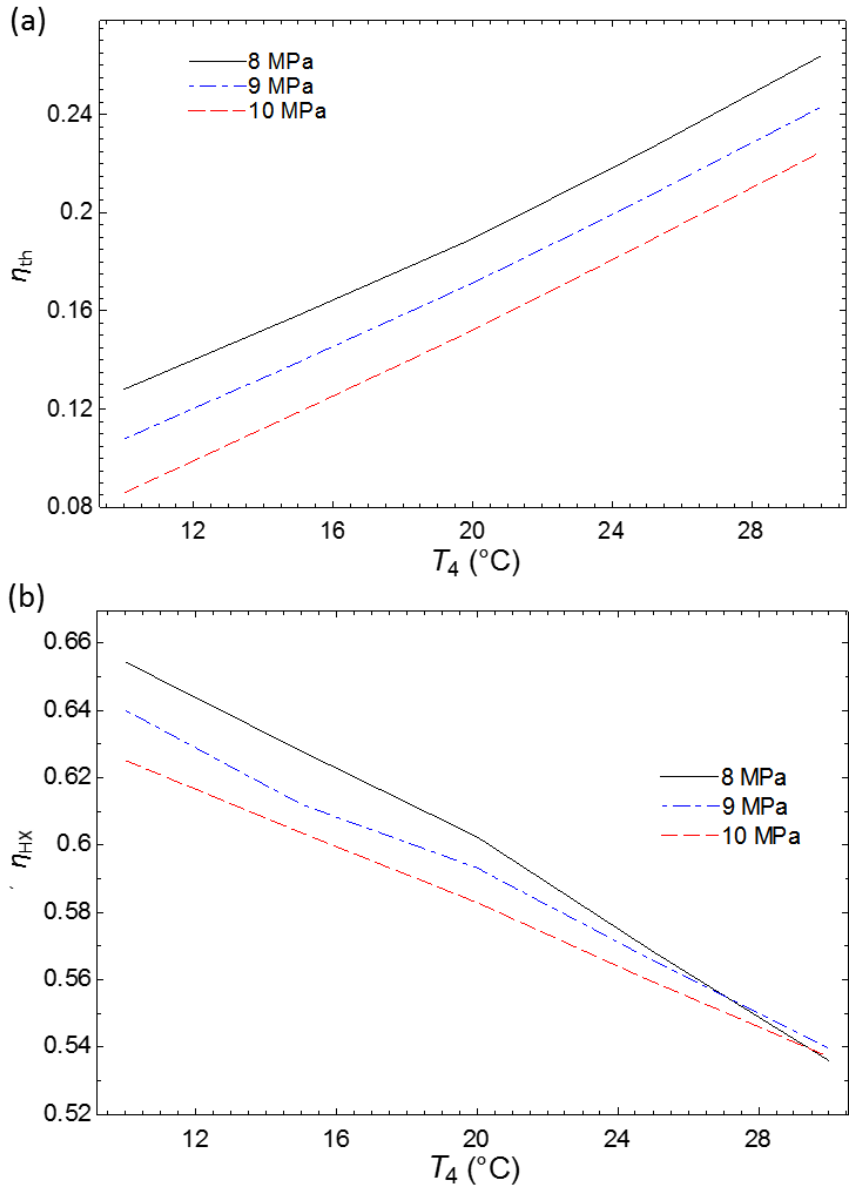

Figure 6.11. (a) thermal system efficiency (η_{th}) and (b) methanol/CO_2 heat exchanger efficiency (η_{HX}) with a difference of the methanol/CO_2 heat exchanger inlet temperature (T_4).

The methanol/CO_2 heat exchanger efficiency shows the ratio of heat quantity transfer from high temperature vapor methanol into the working fluid CO_2 in the methanol/CO_2 heat exchanger. In which Figure 6.11 (b), similar with Figure 6.11 (a) that lower pressure gives higher efficiency (value of 0.65 can be found at 8 MPa), but the methanol/CO_2 heat exchanger efficiency decreases with increasing temperature. Furthermore, at around point of 25 °C, the efficiency of 8 MPa falls off, which is lower than in case of 9 MPa and 10 MPa at the end (30 °C) [8]. The reasons may come from the unique properties of supercritical CO_2.

The specific design of the CO_2/methanol heat exchanger is further required to investigate the optimal design for the system in the further study where the experimental should be conducted for confirming the efficiency of the system.

6.4 Experimental model of the low-temperature geothermal heat pipe

In order to confirm the working principle of the low-temperature geothermal heat pipe, the experiment apparatus have been originally designed and constructed. The heat transfer properties from the hot reservoir to the cold reservoir with a driving force generated by a working fluid in the pipe has been investigated for the purpose of this study. As the primary design, water has been used as a working fluid instead of methanol to avoid the difficulty and to safety in preliminary [19].

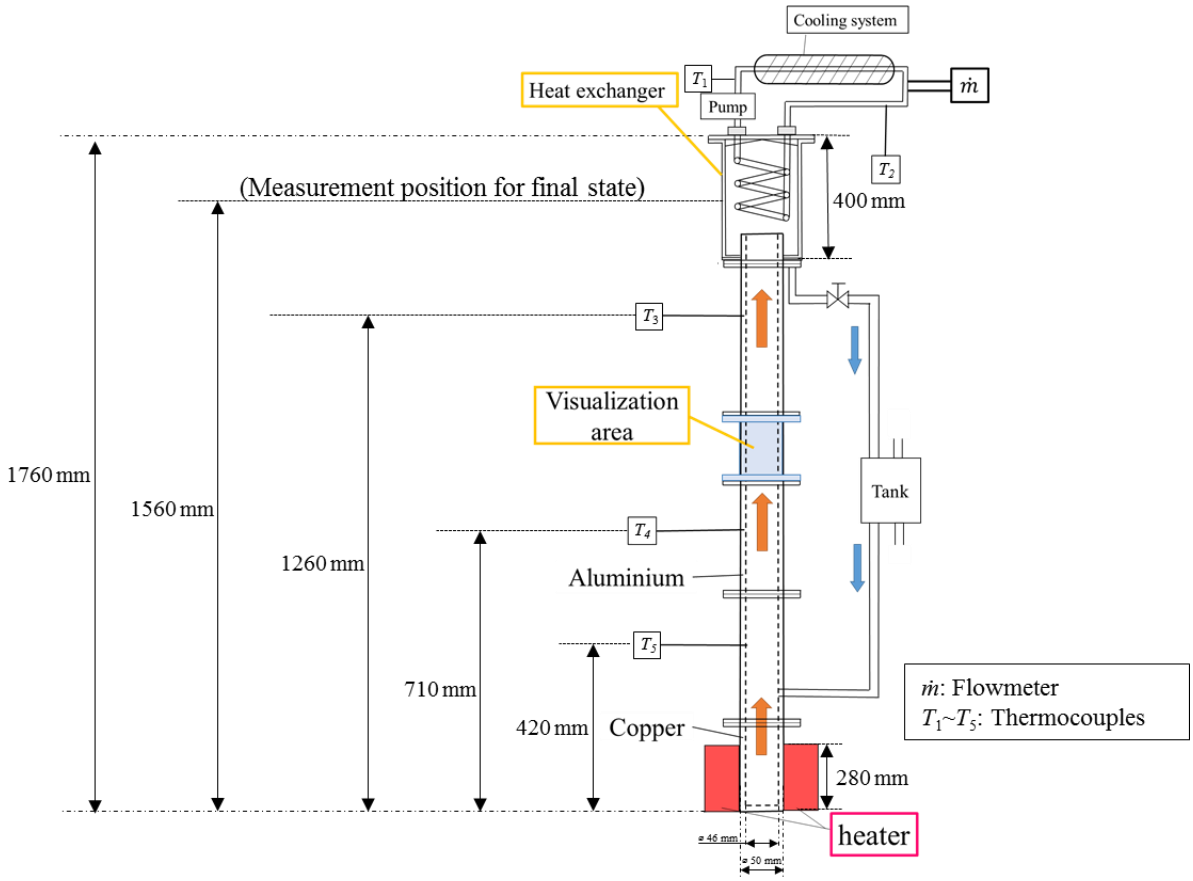

Figure 6.12. Schematic of low-temperature geothermal heat pipe experiment apparatus.

The experiment apparatus is scaled down from the theoretical model in the previous section for usability. The primary structure of the vertical heat pipe model is made from aluminum while the evaporator section (bottom basin) is constructed from copper due to high heat conductivity (398 W/(m·K)) with a total length of 1760 mm and inner and outer diameters of 46 mm and 50 mm, respectively. The schematic of the experiment setup is drawn in Figure 6.12. The visualization area made from polycarbonate is installed in the middle part of the heat pipe for visualization investigate on the flow behavior of working fluid. The glass wool type insulator (thickness of 25 mm) is used to cover the heat pipe for avoiding the heat loss in the system. Band heater is used as the hot reservoir in the evaporator section of the heat pipe with a length of 280 mm and maximum power output of 580 W. At the top side of the heat pipe, heat exchanger unit is installed, which is equipped with the water cooling system. A valve controlled the flow rates of the cold water and measured by a flow meter. In the heat exchanger unit, water tube is made of copper (with 8 mm of inner diameter and 10 mm of outer diameter) as 6 m of total length double-spiral structure in order to enhance the heat exchanger area as shown in Figure 6.13 (a) and (b) for schematic and detail view, respectively. The width and height of the heat exchanger unit are respectively 250 mm 400 mm, and the total heat exchanger area is about 0.18 m^2. The bypass tube is used to drain the liquid water from the heat exchanger unit to the bottom basin. Five K-type

thermocouples with an accuracy of ±2.5 °C for temperature measurements are installed at a different position to measure its temperature and pressure in the heat pipe.

Water is contained in the bottom basin and heated by the heater. After heating, water is boiled, and steam flows to the heat exchanger unit by buoyancy forced created. The steam passes through the visualization area while the flow properties of steam can be observed. When steam reaches the heat exchanger unit, steam is exchanged heat with the cooling water and condense to be liquid state water. The heat transferred from the bottom basin can be observed and calculated by thermocouples and mass flow meter installed at the heat exchanger unit (see Figure 6.12). The condensed liquid water flows down to the bottom basin through the bypass tube for absorbing heat, and the cycle recommences.

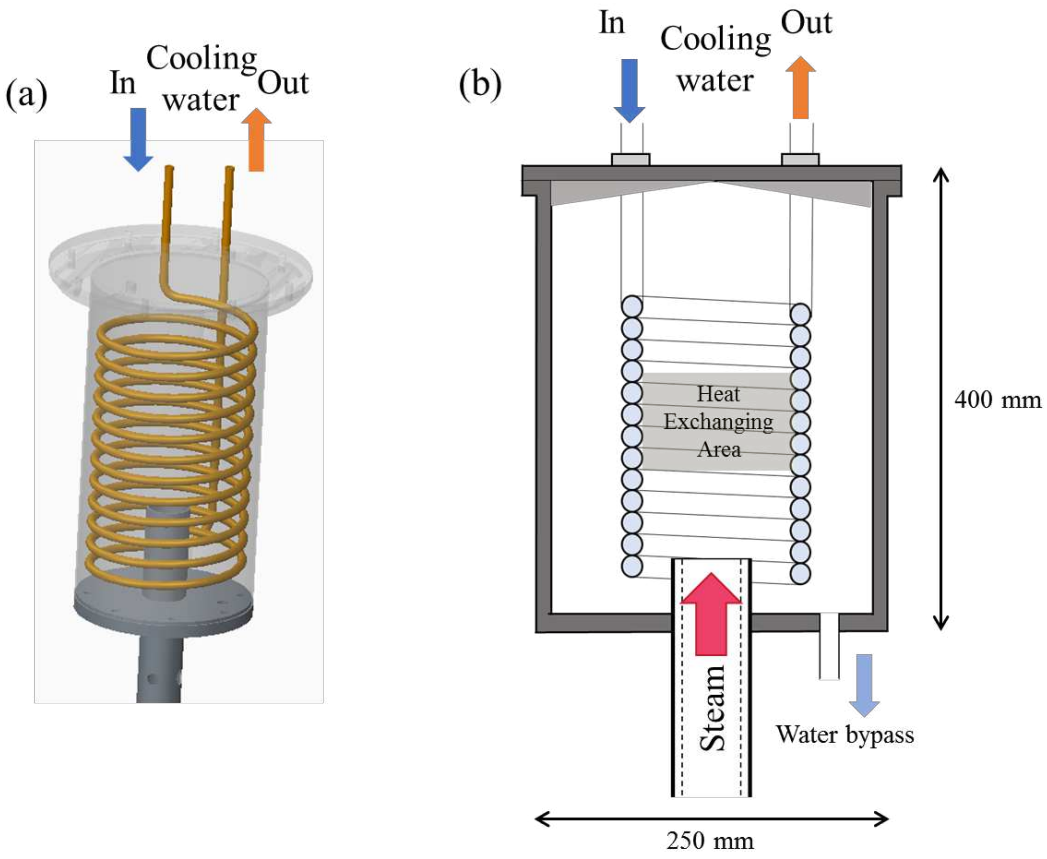

Figure 6.13. Schematic diagram of (a) heat exchanger unit and (b) the detail view.

The experiments were carried out in the heat pipe and its performance in different energy input to the evaporator section (bottom basin) and fill ratios were studied. The electric power supplied q_1 in the heat pipe can be calculated by the supply voltage V and current I of the band heater as expressed in equation (6.16):

$$q_1 = VI \tag{6.16}$$

Furthermore, the heat loss to the ambient in the band heater q_2 is calculated by the temperature gradient dT/dx at two different points at in the heat insulating (heat pipe surface and heater surface), which can be estimated as:

$$q_2 = A\lambda \frac{dT}{dx} \tag{6.17}$$

where λ and A are thermal conductivity of the insulating material and surface area of the heating area in the bottom basin, respectively.

The heat input energy in the system (Q_{in}) is calculated as:

$$Q_{in} = q_1 - q_2 \tag{6.18}$$

The heat recovery Q_{out} from the heat pipe system is found from the heat absorbed by the cooling water in the consider section (heat exchanger unit) as the following relation:

$$Q_{out} = \dot{m}_{water} c_{p\,water} (T_1 - T_2) \tag{6.19}$$

in which $\dot{m}_{water}$ is water mass flow rate, c_{pwater} is heat capacity of cooling water. Temperature T_1 and T_2 are the inlet and outlet temperature of cooling water, respectively.

The heat pipe efficiency can be calculated from the heat recovery and heat input of the heat pipe:

$$\eta = \frac{Q_{out}}{Q_{in}} \tag{6.20}$$

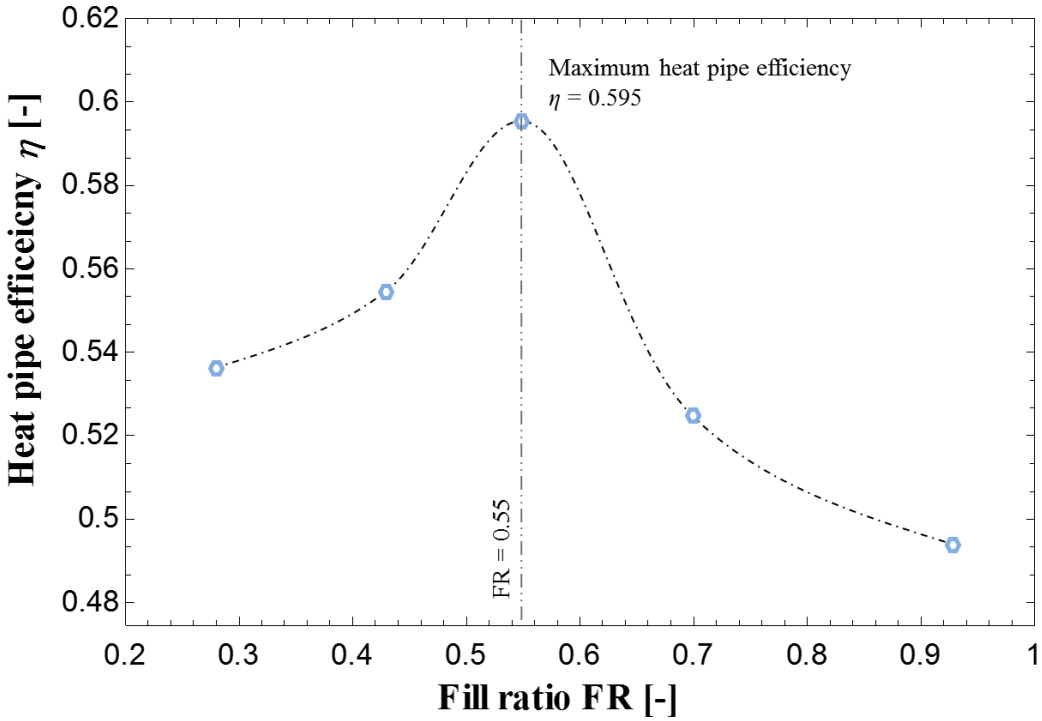

Figure 6.14. The relationship of the water fill ratios in evaporator section and heat pipe efficiency.

From different fill ratios, FR (the ratio of the initial filled water volume and the total volume of evaporation section) of 0.28, 0.43, 0.55, 0.77 and 0.93 with maximum heat input energy of 580 W were examined. The heat pipe efficiency at different fill ratios is plotted in Figure 6.14. The results show that the fill ratios have a significant effect on heat pipe efficiency and in this study, the maximum heat pipe efficiency (= 0.595) can be obtained at FR = 0.55. In which, considering to other researches on heat pipe, the results show the similar trend with other working fluid in the heat pipe [20~21].

From the previous results, the fill ratio of 0.55 is selected to use as the reference in this study due to the highest efficiency condition. The measurement values of the evaporated water volume in the evaporator section with heat reaching to the temperature measurement points (T_3, T_4, and T_5) are used

to compare with theoretical. The distance and position of each measurement points are referred to Figure 6.12. The temperature of 95 ~ 100 °C is set to be a reference of temperature reaching a point with keeping stable altitude.

Table 6.1. Experimental and evaluation results.

	The water level in bottom basin ΔL [mm]	Steam raising distance ΔH [mm]	Heat input Q_{in} [W]	Heat output Q_{out} [W]	Heat pipe efficiency η [-]
State (i), initial state	154	-	0	0	-
State (1), temperature reaching T_5	103	317	85.8	13.44	0.156
State (2), temperature reaching T_4	103	607	141.8	47.07	0.332
State (3), temperature reaching T_5	86	1174	291.8	100.8	0.345
State (f), stable state	77	1483	580	345.1	0.595

Table 6.1 shows the results of the experiment and evaluation of the water level in the evacuator section when the heat reaches each temperature measurement points with the heat pipe efficiency. For comparison, an initial state (starting condition) a stable state (maximum heat input) have been included: in this case, it was assumed that the system is in most stable at 580 W of heat input. The detail of water and steam rising level in the heat pipe is drawn in Figure 6.15.

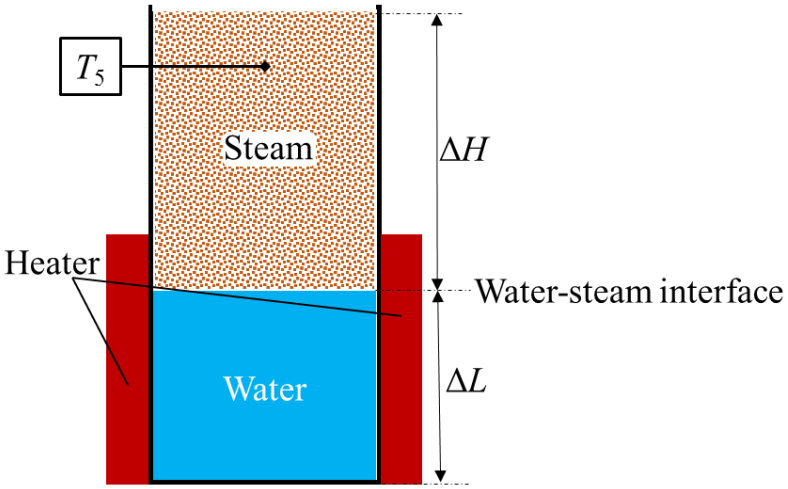

Figure 6.15. Detail of water level ΔL and steam rising ΔH in the heat pipe.

It can be observed from the Table 6.1 that the water level at State (1) is decreased from the state (i) about 51 mm. Furthermore, the water level at State (2) is kept constant from the State (1) while the heat input Q_{in} to the heat pipe is found increased. Moreover, the distance between temperature measurement points T_5, and T_4 is about 290 mm. Unlikely with the highly significant decrease of water level from the state (i) to (1), the water level slightly decreases, only 9 mm from the State (3) to the stable at State (4) although the huge of heat input applies to the heat pipe. The reason may come from the quality of wet steam ($x < 1$) during the evaporation process of water in the heat pipe, in which will be detail discussed in this chapter.

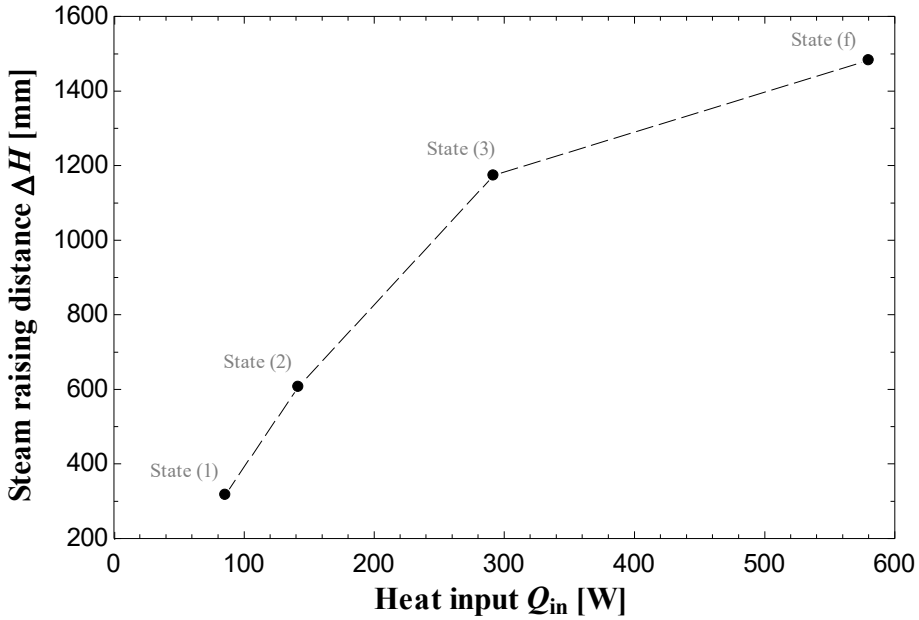

Figure 6.16. The relationship between heat input and the steam raising distance from the water surface.

Figure 6.16 shows the relationship of the steam rising distance in the heat pipe ΔH and heat input Q_{in}. The results indicate that an increase of heat input leads to an increase in rising steam distance from the water surface. This is due to high heat input causes an increase in the evaporation of water leading to increasing of steam vapor and quality affecting the rising of steam and heat in the heat pipe. Steam quality x refers to the ratio of steam in the vapor phase to the liquid phase [22].

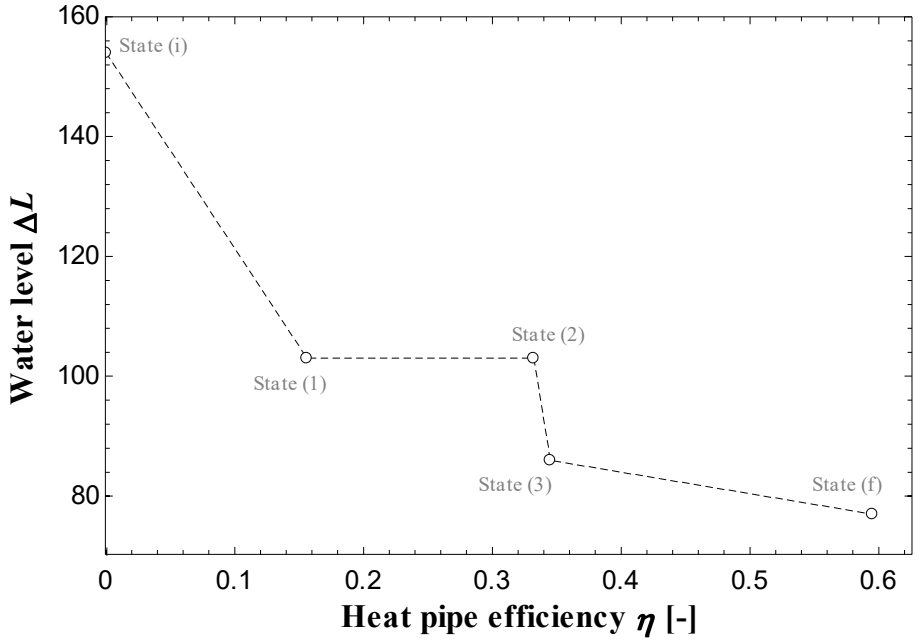

Figure 6.17. The relationship between heat pipe efficiency and the water level in the bottom basin.

In Figure 6.17, the variation of heat pipe efficiency with the water level in the bottom basin is plotted. The heat pipe efficiency can be calculated from the ratio of heat input and heat output of the heat pipe (equation (6.12)), referring to each state condition in Table 6.1. It can be seen that heat pipe efficiency tends to decrease with decreasing of the water level. This is because the water level decreases which results in evaporation process in the bottom basin. Water turns to steam. Therefore, steam expands inside the heat pipe due to the higher specific volume. It can be confirmed by the increase of

heat pipe efficiency (see Figure 6.17). However, as mentioned earlier, the water level was found to be kept constant during State (1) to State (2), which it is explained quality of wet steam in the heat pipe.

6.5 Discussion on the evaporation process in the heat pipe

In the evaporator section (bottom basin), heat input from the heater is applied to the water. The water temperature gets increased from the initial state of 25 °C to the boiling point of 100 °C. This is to say that the heat transferred from one system to another, while the temperature changes with no phase change can be referred to as sensible energy or sensible heat [23]. For the further heating, of what is now water, change of phase to steam occurs at a constant temperature with constant pressure and is accompanied by a reduction in specific volume, the heat required for this process knowing as the latent energy or latent heat [24]. The heat requires to change 1 kg of a liquid (water) to a gas (steam) is called the latent heat of vaporization, which is expressed as:

$$Q_l = mL_v \tag{6.21}$$

where m is mass of the water that becomes vapor and L_v is the specific latent heat of vaporization, in which equals to 2,258 kJ/kg for water. The relationship between temperature and heat input in the heat pipe is plotted in Figure 6.18 to understand the properties of water and steam in the heat pipe operation.

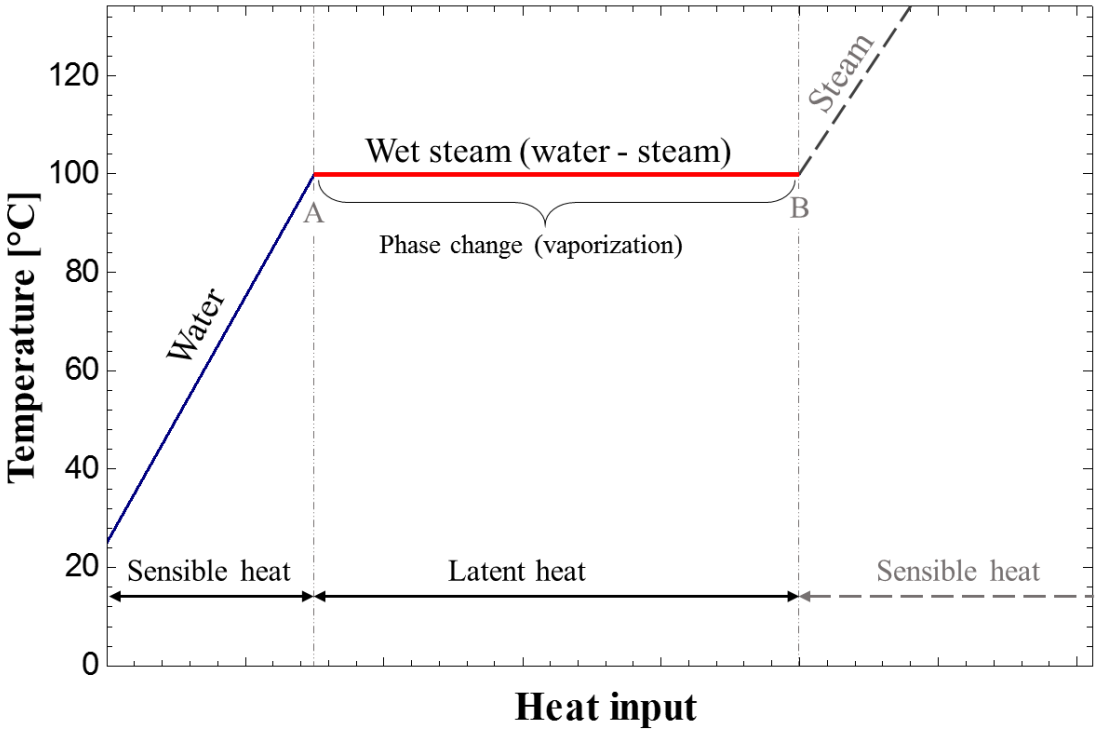

Figure 6.18. The phase property of water in the heat pipe with increasing temperature and heat input.

As shown in Figure 6.18, from the starting point (water at 25 °C), water is in it liquid phase, as the heat is added the heat goes into the kinetic energy of the water bringing the temperature up to its boiling point (100 °C), but water is still a liquid phase at Point A. As it is heated further, the energy from the heat input overcomes the bonds, in which the phase change can be indicated by the flat region (Point A – Point B). When the water obtains enough kinetic energy to escape from the liquid phase (Point B), the water is entering the gas phase and becoming steam. Beyond the Point B, if further heat is added, it can raise the steam temperature above 100 °C.

Consider in this study for the experimental model of the heat pipe, the temperature of the steam inside the system is found maximum at 100 °C. It can be obviously considered that the steam inside the

heat pipe falls in the wet steam region, which means the heat input is not enough to exceed the energy required to enter the superheat region ($x \geq 1$) [22].

From the experimental results shown in Table 6.1, the water level decreases from the State (i) to State (1) about 51 mm, in which the vanished water changes into the steam and expands inside the heat pipe. Furthermore, from the State (1) to (2), the water level is kept stable while the steam expands in the heat pipe (317 mm to 607 mm of rising distance). In the other word, the steam changes its volume when increasing heat input. The steam quality can explain this phenomenon in heat pipe that steam becomes more superheat steam (x approaches to 1) in the State (2) compared with the State (1). It can be confirmed with the heart pipe efficiency of State (2) higher than in State (1), which is because of lower quality of steam contains lesser energy [25]. Moreover, lower quality steam contains more moisture that is in the production of condensate initially as when entering to the heat exchanger unit. The vapor phase, steam must reduce its quality to saturated liquid ($x = 0$) and give up its latent heat before condensing to water (liquid phase) [26].

On the other hand, in each state of heat pipe experimental, steam has different quality vary on heat input in the heat pipe. However, if both saturated water and saturated steam, and any state between, can exist at the same pressure and temperature condition, it is impossible to determine the steam quality by only measuring pressure and temperature in the heat pipe. In purpose of this study, Figure 6.19 has been illustrated by using the experimental data to estimate the condition inside the heat pipe.

From the State (i), no heat inputs to the heat pipe, the water level is 154 mm height at the initial state. After adding heat input of 58.8 W (State (1)), the temperature at T_5 is reached to 100 °C and became stable (no temperature increases at T_5 and T_4). The heat pipe efficiency can be found as low as 0.156. The reasons may come from the long distance to the heat exchange unit and the imperfect insulator of the heat pipe. At State (2), vapor rising distance and temperature inside the heat pipe got higher. The efficiency at State (2) (0.332) is higher than the State (1), so the heat pipe is approached to the more stable state. The moisture is also high condensed in the heat pipe wall surface, in which the condensation process took place before vapor reaching the heat exchanger unit.

It can be confirmed by the moisture appeared on the inner wall surface of the visualization area (Figure 6.20). It is able to say that the high condensation on the heat pipe wall decreases the heat pipe efficiency. In State (3) and (f), heat pipe respectively has higher efficiency, 0.345 and 0.595, along with the increase of heat input. The condensation on the upper wall surface also has taken place due to the height vapor raising distance. To deal with the loss due to the condensation on the wall surface, the optimum condition, and novel heat pipe design would be considered to avoid the nonstable condition of heat pipe operation [27].

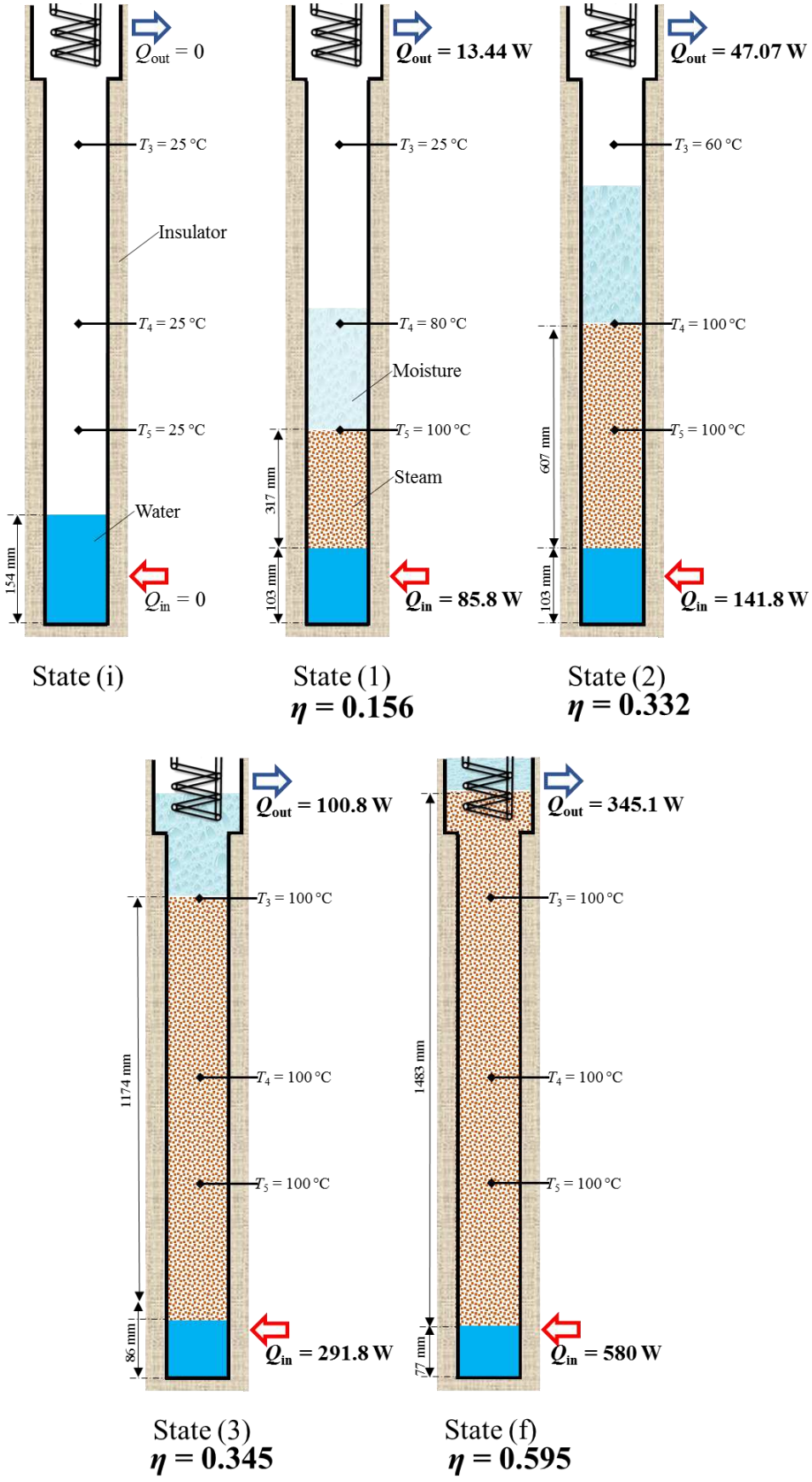

Figure 6.19. The state operations of heat pipe.

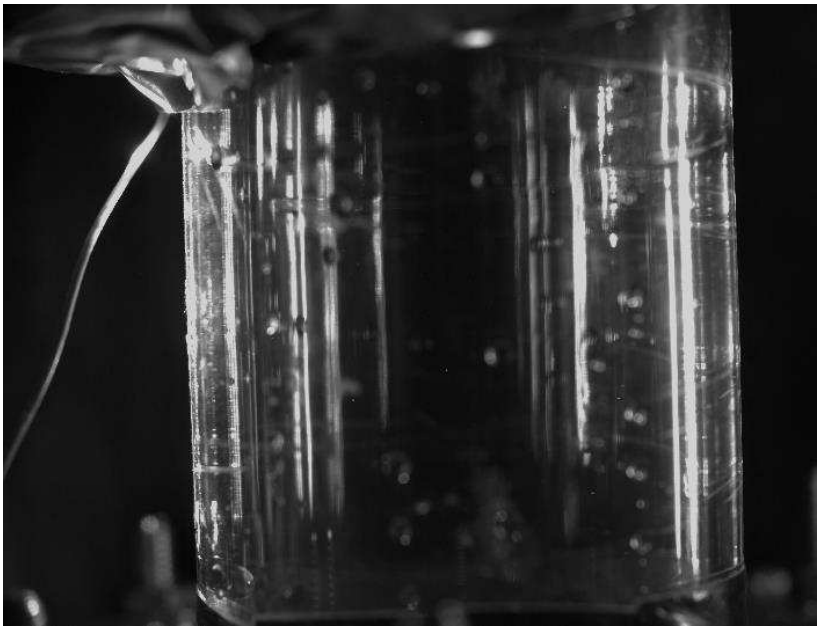

Figure 6.20. The moisture on the wall of the visualization area in the heat pipe.

6.6 Feasibility of heat pipe operation in low-temperature geothermal

In order to confirm the feasibility of geothermal heat pipe in section 6.2 and 6.3, the theory of models (based on the experimental model in section 6.4) is readily developed by obtaining the principle of dimensional analysis and similitude [28]. In this section, the Buckingham's π-theorem, which is based on the notion of dimensional homogeneity is applied [29]. The physical phenomena given in heat pipe model can be described by a term of π as

$$\Pi_{1m} = \phi\left(\Pi_{2m}, \Pi_{3m}, ..., \Pi_{nm}\right) \tag{6.22}$$

Equation (6.22) is employed to explain the behavior of a particular of the experimental model of the heat pipe, the relationship of actual geothermal heat pipe model can be full similarity written as

$$\Pi_{1a} = \phi\left(\Pi_{2a}, \Pi_{3a}, ..., \Pi_{na}\right) \tag{6.23}$$

These parameters are the same at both heat pipe experimental model scale and actual geothermal model scale as long as the same phenomenon is involved, following conditions,

$$\begin{aligned} \Pi_{2m} &= \Pi_{2a} \\ \Pi_{3m} &= \Pi_{3a} \\ &\vdots \\ \Pi_{nm} &= \Pi_{na} \end{aligned} \tag{6.24}$$

while the function φ is for same as a heat pipe experimental model and actual geothermal model can be shown as

$$\Pi_{1m} = \Pi_{1a} \tag{6.25}$$

Equation (6.24) is called model design conditions and equation (6.25) is prediction equation, which is the value of Π obtained in the experimental model equals with for the actual geothermal model on condition that the other π terms are equaled.

To determine the feasibility of the actual geothermal heat pipe, the heat output Q_{out} should be performed by using the information obtained from section 6.2 through 6.4. It is to be expected that heat output Q_{out} to depend on the heat input Q_{in}, steam rising distance ΔH, tube diameter D, the mass of working fluid m, working fluid boiling temperature T_b and specific heat of working fluid c_p. It can be hence,

$$Q_{out} = f\left(Q_{in}, \Delta H, D, m, T_b, c_p\right) \tag{6.26}$$

where the dimension writes down,

$$Q_{out} \doteq \mathrm{ML^{-1}T^{-2}}$$
$$Q_{in} \doteq \mathrm{ML^{-1}T^{-2}}$$
$$\Delta H \doteq L$$
$$D \doteq L$$
$$m \doteq M$$
$$T_b \doteq \Theta$$
$$c_p \doteq \mathrm{L^2T^{-2}\Theta^{-1}}$$

From the variation above, the application of the π-theorem results

$$\frac{Q_{out}Q_{in}}{\Delta H^4 m^2} = \phi\left(\frac{D}{\Delta H}, \frac{c_p T_b m^{2/3}}{Q_{in}{}^{2/3}\Delta H^{2/3}}\right) \tag{6.27}$$

The heat output similarity requires that the dimensional group between the experimental model and actual geothermal heat pipe by obtaining data and variables from section 6.3 and 6.4, respective, thus

$$\left(\frac{Q_{out}Q_{in}}{\Delta H^4 m^2}\right)_{model} = \left(\frac{Q_{out}Q_{in}}{\Delta H^4 m^2}\right)_{actual} \tag{6.28}$$

The conditions of geothermal heat pipe model using for heat output prediction are referred to the State (1), (2), (3) and (f) in section 6.4. As shown in Figure 6.21, the predicted heat output is increased following from State (1) to (f), which is according to the higher in heat output of heat pipe model in each state. It can be confirmed by the increase of heat pipe efficiency in each state. The Q_{out} obtained for actual geothermal heat pipe can achieve highest at 83.36 kW.

This is a reasonable heat output that could be certainly reached in a system with using water as a working fluid. The heat pipe experimental model shows the feasibility of heat transfer principle of the heat pipe. However, it is to be noted here that this is the result of using water but in the actual model design, the working fluid methanol is employed. Methanol has a lower boiling point and higher specific heat compared with water, in which it is promising that the actual operation condition in geothermal heat pipe gives higher performance nearly to the calculation in section 6.3.

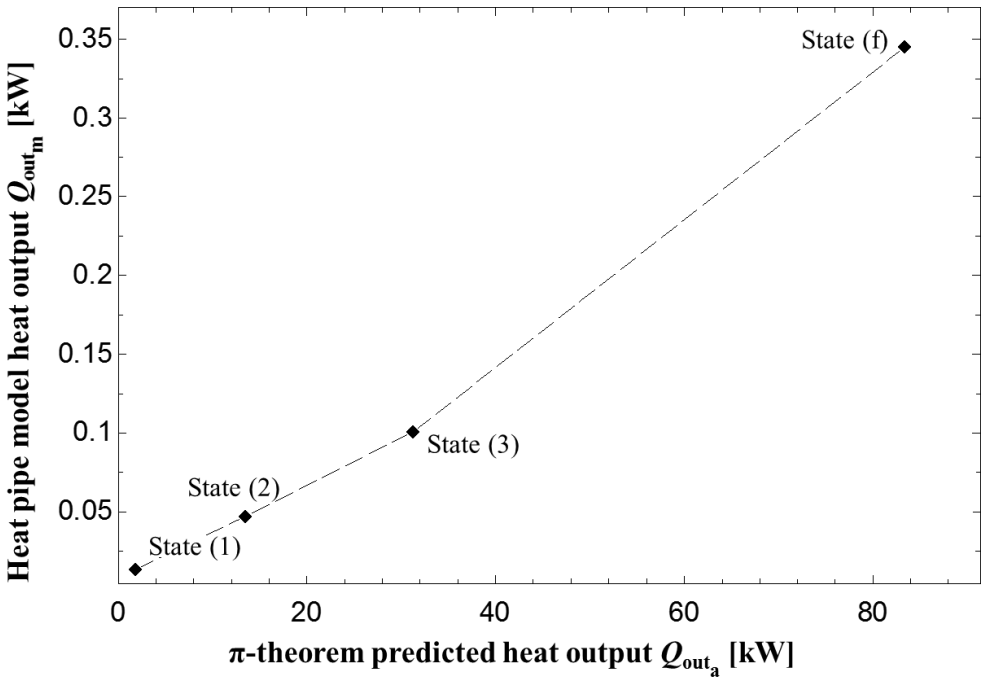

Figure 6.21. The prediction heat output of actual geothermal heat pipe based on π-theorem with the condition State (1), (2), (3) and (f) from the heat pipe model.

6.7 Conclusions

The primary design was proposed in the present study. The analysis for the heat pipe using methanol as a working fluid is performed in this study in application to the low-temperature geothermal reservoir for thermal energy absorption. The heat pipe can be combined with the supercritical CO_2 Rankine cycle system to generate electric power and to supply the thermal energy.

The present study shows the feasibility of the system where it is operated for the shallow low-temperature geothermal reservoir (likewise in the spa) without extracting spa (hot water). The following results are summarized;

(i) The thermal efficiency and methanol/CO_2 heat exchanger efficiency were investigated where the highest values of 0.25 and 0.65 were estimated, respectively.

(ii) With the condition of approximately 7 m height of methanol level in the basin. The heat pipe can transfer the energy to the CO_2/methanol heat exchanger as higher than 224 kW, which can achieve the 20 kW and 189 kW of electric energy generation and thermal supplied energy, respectively.

(iii) Increasing the inlet temperature of methanol/CO_2 heat exchanger gives the higher value both of thermal system efficiency (η_{th}) (in lower temperature) and methanol/CO_2 heat exchanger efficiency (η_{HX}) (in higher temperature).

(iv) The low-temperature geothermal reservoir can be utilized to generate electric power energy by using heat pipe technology together with supercritical CO_2 Rankine cycle system, which the electric power generation from the system can achieve higher than 50 kW in this study.

(v) The experimental model of heat pipe shows the feasibility of the heat transfer principle of heat pipe by using water as a working fluid. The fill ratio of 0.55 gives the highest efficiency to heat pipe operation. However, the details on the vapor flow in the heat pipe would be investigated by visualization principle to confirm the flow behavior.

(vi) Buckingham π-theorem's is employed to confirm the feasibility in the current design of heat pipe model. The use of methanol working fluid in the heat pipe would be further investigated in the experimental model to the accuracy in the low-temperature geothermal heat pipe.

References

[1] Duffield, W.A. and Sass, J.H., 2003. *Geothermal energy: Clean power from the earth's heat* (Vol. 1249). US Geological Survey.

[2] Chamorro, C.R., Mondéjar, M.E., Ramos, R., Segovia, J.J., Martín, M.C. and Villamañán, M.A., 2012. World geothermal power production status: Energy, environmental and economic study of high enthalpy technologies. *Energy*, *42*(1), pp.10-18.

[3] Østergaard, P.A. and Lund, H., 2011. A renewable energy system in Frederikshavn using low-temperature geothermal energy for district heating. *Applied Energy*, *88*(2), pp.479-487.

[4] Hettiarachchi, H.M., Golubovic, M., Worek, W.M. and Ikegami, Y., 2007. Optimum design criteria for an organic Rankine cycle using low-temperature geothermal heat sources. *Energy*, *32*(9), pp.1698-1706.

[5] Guo, T., Wang, H. and Zhang, S., 2011. Comparative analysis of natural and conventional working fluids for use in transcritical Rankine cycle using low-temperature geothermal source. *International Journal of Energy Research*, *35*(6), pp.530-544.

[6] Zhang, X.R., Yamaguchi, H., Fujima, K., Enomoto, M. and Sawada, N., 2005. A feasibility study of CO_2-based Rankine cycle powered by solar energy. *JSME International Journal Series B Fluids and Thermal Engineering*, *48*(3), pp.540-547.

[7] Kubota, H., Hondo, H., Hienuki, S. and Kaieda, H., 2013. Determining barriers to developing geothermal power generation in Japan: Societal acceptance by stakeholders involved in hot springs. *Energy Policy*, *61*, pp.1079-1087.

[8] Pumaneratkul, C., Yamasaki, H., Yamaguchi, H., Kitamura, S. and Sako, Y., 2017. Supercritical CO_2 Rankine Cycle System with Low-Temperature Geothermal Heat Pipe. *Energy Procedia*, *105*, pp.1029-1036.

[9] Sugino, H., Akeno, T., 2010. The 2010 country update for Japan. In: *Proceedings of the 2010 World Geothermal Congress*. Bali, Indonesia, April 25–29, pp 7.

[10] Zhang, X.R., Yamaguchi, H., Uneno, D., Fujima, K., Enomoto, M. and Sawada, N., 2006. Analysis of a novel solar energy-powered Rankine cycle for combined power and heat generation using supercritical carbon dioxide. *Renewable Energy*, *31*(12), pp.1839-1854.

[11] PROPATH Group, 1997. PROPATH: a program package for thermophysical properties.

[12] ESDU 80017, 1980. "Thermophysical properties of heat pipe working fluid: operating range between -60 °C and 300 °C." Data Item No. 80017, *Engineering Sciences Data Unit*, London.

[13] Mita, N., Maruyama, A., Usui, A., Higashihara, T. and Hariya, Y., 1994. A growing deposit of hydrous manganese oxide produced by microbial mediation at a hot spring, Japan. *Geochemical Journal*, *28*(2), pp.71-80.

[14] Cengel, Y.A., Ghajar, A.J. and Kanoglu, M., 2011. *Heat and mass transfer: fundamentals & applications* (Vol. 4). New York: McGraw-Hill.

[15] Davis, A.P. and Michaelides, E.E., 2009. Geothermal power production from abandoned oil wells. *Energy*, *34*(7), pp.866-872.

[16] ESDU 81038, 1981. "Heat pipes – performance of two-phase closed thermosyphons." Data Item No. 81038, *Engineering Sciences Data Unit*, London.

[17] Pumaneratkul, C., Yamasaki, H. and Yamaguchi, H., 2017. Optimum Study on Primary Design of Geothermal Heat Pipe with CO_2 Based Rankine Cycle. *Energy Procedia*, *143*, pp.748-753.

[18] Badran, B., Gerner, F.M., Ramadas, P., Henderson, T. and Baker, K.W., 1997. Experimental results for low-temperature silicon micromachined micro heat pipe arrays using water and methanol as working fluids. *Experimental Heat Transfer an International Journal*, *10*(4), pp.253-272.

[19] Mozumder, A.K., Akon, A.F., Chowdhury, M.S.H. and Banik, S.C., 2011. Performance of Heat pipe for different Working fluids and Fill ratios. *Journal of Mechanical Engineering*, *41*(2), pp.96-102.
[20] Sukchana, T. and Jaiboonma, C., 2013. Effect of filling ratios and adiabatic length on thermal efficiency of long heat pipe filled with R-134a. *Energy Procedia*, *34*, pp.298-306.
[21] Muldary, P.F. and Tansev, E., Chevron Research and Technology Co, 1979. *Determining steam quality*. U.S. Patent 4,149,403.
[22] Honig, J.M., 2013. *Thermodynamics: principles characterizing physical and chemical processes*. Academic Press.
[23] Partington, J.R., 1949. *An advanced treatise on physical chemistry* (No. 541.3). Longmans, Green,.
[24] Clark, J.O.E. ed., 2004. *The essential dictionary of science*. Barnes & Noble.
[25] Babcock & Wilcox Company, 1913. *Steam, its generation and use*. Babcock & Wilcox..
[26] Gilpin, A.S., Herrman, T.J., Behnke, K.C. and Fairchild, F.J., 2002. Feed moisture, retention time, and steam as quality and energy utilization determinants in the pelleting process. *Applied engineering in agriculture*, *18*(3), p.331.
[27] Park, J.H., 1997. A study on thermal performance of heat pipe for optimum placement of satellite equipment. *ETRI journal*, *19*(2), pp.59-70.
[28] Munson, B.R., Okiishi, T.H., Rothmayer, A.P. and Huebsch, W.W., 2014. *Fundamentals of fluid mechanics*. John Wiley & Sons.
[29] Yamaguchi, H., 2008. *Engineering fluid mechanics* (Vol. 85). Springer Science & Business Media.

Chapter 7

Summary, conclusions, feasibility, and future directions

Owing to the reason in environment and energy issues, the utilization of green energy resources is more and more considered with serve attention to promoting an actual industrial application and to achieve Montréal Protocol compliance. After phasing down of HFCs due to the Paris Agreement objectives, natural working fluid is recommending replacing for industrial application, which is ammonia (NH_3) and carbon dioxide (CO_2). However, NH_3 is categorized as a hazardous substance, which effects on human health. For this reason, CO_2 gains much attention and be for a pathway for next-generation working fluid

Research using supercritical CO_2 in energy conversion system has been pursued. The system is considered to be a pathway for combating energy and global warming crises. One of the keystones for obtaining sustainable development is the utilization of supercritical CO_2 properties. Giving preventing global warming and sustainable energy development, supercritical CO_2 solar Rankine cycle system (SRCS) has been developed for power production by gaining the considerable potency of solar energy with using supercritical CO_2 as a working fluid.

In this thesis, the processes of thermodynamic power cycles were discussed and compared by showing the effects of supercritical Rankine in term of power generation. The gas behavior of CO_2 in supercritical state deviates significantly from the ideal gas. The properties of supercritical CO_2 are provided based on the Peng-Robinson equation of state, which is based equation of PROPATH database. The unique property of supercritical CO_2 is that CO_2 in the pseudocritical region is enhancing the higher in convective heat transfer coefficient, which can be feasibly acclaimed efficient operations of energy conversion system. The maximum value of specific heat can be achieved at the pseudocritical point, in which can be confirmed with the high peak of Prandtl number at the same point.

The current developments on SRCS are reported based on the proper components design, which is evacuated solar collector, turbine, and thermally driven pump. In the heat collection part, the cascade arrangement of evacuated solar collector shows the optimum to the system in term of CO_2 mass flow rate and heat collection efficiency. Turbine with 1.0 mm and 33 mm of nozzle diameter and length, respectively, is considered to use due to prevent of choked flow phenomenon and to enhance the power generation in the system. Furthermore, in order to reduce the efficiency losses occurred in the conventional mechanical feed pump used in the system, the thermally driven pump is introduced to replace with the mechanical feed pump. The results confirm the feasibility to circulate CO_2 in the system without electric energy required. The exergy analysis on the system further investigates and verify the higher efficiencies and advances of the thermally driven pump over the mechanical feed pump. Besides, the thermally driven pump helps to decrease the exergy destruction rate in the evacuated solar collector while the exergetic efficiency of turbine finds an increase, in which the electric power generated is considered as the main principle of the system.

The author believes that the combination of solar energy and CO_2, SRCS gives the feasibility in a long-running field test. As the dilatation of SRCS, it can be the path of future development in a small-scale standalone or smart grid energy conversion system.

Extension system from the SRCS, the CO_2-based photovoltaic-thermal hybrid system is developed to improve in power generation of the photovoltaic solar cell and to increase the efficacy of SRCS. Liquid CO_2 is used to absorb the waste heat of the photovoltaic solar cell and cool the surface of the solar cell. The highest of 2 % in generation efficiency gets improve to the photovoltaic solar cell

alone. Another additional purpose of the hybrid system is to preheat CO_2 before entering the evacuated solar collector, which maximum 28 °C can be found in this study. To confirm the temperature distribution on the surface of the photovoltaic solar cell, the numerical analysis has been conducted. The results from analysis acclaimed good trend of temperature distribution compared with the experimental results, especially in case of summer condition. The combination of the hybrid system and SRCS show the significant pathway to using CO_2 as a working fluid in energy conversion system both in term of the environment and economic.

In the final study, SRCS has been used as a secondary cycle to generate electric and heat energy from geothermal energy (underground reservoir). To utilize the low-temperature geothermal energy from the shallow borehole, the heat pipe (thermosyphon) principle where a working fluid with a low boiling temperature (methanol) is circulated and extracted heat to generate electric energy. From the numerical calculation, the supercritical CO_2 Rankine cycle system with low-temperature geothermal heat pipe shows the feasibility in power generation by using only around 100 °C of the low-grade geothermal reservoir. The experimental model based on the principle of geothermal heat pipe has been scaled down and primarily constructed by using water as working. It can be observed the reassuring results of heat transfer in heat pipe experimental. The wet steam phenomenon explains the relation between the steam rising distance in the heat pipe and heat pipe efficiency, in which moisture also can be observed at the wall of the visualization area. The experiment data from heat pipe model is based on predicting of heat output in the actual geothermal heat pipe that is the affirmative working principle of the heat pipe. However, for more accuracy, methanol would be used as a working fluid in the heat pipe experimental model.

After the Fukushima incident in 2011, the Japan government has decided to shut down all nuclear power plant, which equals to about 30 % of energy consumption share in Japan. To deal with the loss in energy production, the coal-fired power plants are retrofitted and set to play an increasingly important role in the energy supply. However, Japan's weakness is its geography that Japan is highly scarcity in energy resources causing Japan to rely seriously on imports. The fossil fuels and LNG (liquefied natural gas) imported of Japan significant increase after 2011, leading Japan to face significant energy security challenges. The recruitment of renewable energy resources is the necessity to fulfill the energy consumption. The study in SRCS is compelling to be the new pathway of energy supply for Japan and global.

Furthermore, to harness the low-grade geothermal energy by using heat pipe, it can increase the potential of geothermal in Japan. The power generation from geothermal in Japan is relatively low compared with overall potential, which is because of the laws restricting geothermal electricity production. Most geothermal sites in Japan are in the national park, which is out of developing. The low-temperature heat pipe can use the benefit from abandon hot spring borehole that exists everywhere across the country to generate electric and heat energy and fulfill the energy challenge of Japan.

Acknowledgment

During the past five years studying in Japan, I have learned and growth to be a person. To complete this Ph.D. study, it is a truly life-changing experience for me. It would not have been possible without direct and indirect encourage and support that I received from many people.

First and foremost, I would like to express sincere thanks to my supervisor, Professor Hiroshi Yamaguchi, for the continuous support and patient guidance in the time I spent at Doshisha University. I appreciate all his thought and kindness contribution to my study to make me growth as a good researcher.

I will forever be thankful to my senior fellow, Professor Yuhiro Iwamoto, and Professor Haruhiko Yamasaki, for all the great advice they always give to me for the research and methodology of life. Special thanks to Professor Yoshifumi Kimura for the suggestion he made in Chapter 2 of this work.

Many thanks to all members as well as the alumni of Physics (Yamaguchi) Laboratory at Doshisha University who are always doing hard study for our research. I would like to express my special thanks to Rankine team 2013 to 2018, Harunobu Kido, Hiroki Takeuchi, Takanori Maki, Kyosuke Fujita, Takashi Horino, Yuta Fujimune and Maiko Yamakawa, and heat pipe team, Yu Nakazawa and Kensaku Fukushige for all the help in the experiments work and cooperate in the research.

I gratefully acknowledge to the Global Resource Management (GRM) program at Doshisha University for the generosity to support me in this Ph.D. study and to explore my knowledge in the field of global studies. I would like to give my special thanks to all professors, staffs and students in GRM program for the great ambitions and contribute to significantly and successfully in the program's achievements. It is an inspiration on the interdisciplinary studies to approach my study in Chapter 6 of this work. In addition, I would like to thank to the supervisor and members of GRM student project 2017, Professor Akira Hayashida, Yan Chen and Mostafa Khalili, I have gained many knowledge and experience from the field that are very meaningful to me.

I wish to thank to all friends at Doshisha University and Thai students' Association in Japan whom I have interacted with for all supporting in many different ways with the fun environment to learn and grow.

Thanks to Teemaporn Liewchumnong for the loving, supporting, encouraging and waiting me till the finish of this study. Your supportive comforts me and helps me get thru the difficult time.

Lastly and most importantly, I would love to dedicate this work to my parents and my brother. Thank you for your innumerable support to my study here in Japan, and the unconditional love you give me.

Chayadit Pumaneratkul

Doshisha University, Kyotanabe Campus, Kyoto

Night of June 1, 2018